Measurement of Fugitive Greenhouse Gas Emissions from an Oil Sands Tailings Pond

by

Hao Shi

A thesis submitted in partial fulfillment of the requirements for the degree of

Master of Science

in

Environmental Engineering

Department of Civil and Environmental Engineering

University of Alberta

Abstract

Alberta oil sands tailings ponds are under the concern of releasing greenhouse gases (GHGs) including carbon dioxide (CO_2) and methane (CH_4). In this research, Eddy Covariance (EC) technique was used to measure GHGs emissions from an oil sands tailings pond. A tower with EC instruments mounted on top was placed at the south bank of the tailings pond from July 27, 2017 to September 29, 2017. EC instruments mainly included gas analyzers for concentration measurements of both CO_2 and CH_4, and a 3D sonic anemometer for wind speed measurement. Collected data were processed using EddyPro software, and analyzed to show relationships between measured concentrations, calculated fluxes and potential impacting factors such as wind speed, wind direction, and temperature. The median concentration measurements of CO_2 and CH_4 over the entire measurement period are 385.3 ppmv and 3.0 ppmv, respectively. The median flux measurements of CO_2 and CH_4 are 6.8 $g/m^2/d$ and 6.5 $g/m^2/d$, respectively as flux values over the entire measurement period. The footprint analysis of the flux measurements shows that the majority of source areas contributing to the flux values was within the boundary of the pond, when the EC tower was downwind of the tailings pond. The flux values obtained using EC were compared to previous flux measurements at the same tailings pond by flux chamber technique, and synchronous independent EC, flux chamber, flux gradient, inverse dispersion modelling (IDM) measurements by Environment and Climate Change Canada (ECCC). CH_4 concentration measurements and flux calculations from this study were aligned with flux measurements reported by ECCC. The median CH_4 flux measurements of this thesis of 6.5 $g/m^2/d$ is 12% different from the ECCC's median flux measurements value of 7.4 $g/m^2/d$. Concurrently

historical flux chamber measurements of this target pond are lower than the EC flux measurements due to the inability of flux chamber to capture the heterogeneity of the tailings pond. Therefore, it is recommended to use EC for measuring GHG flux from oil sands tailings ponds.

Preface

This thesis is an original work by me. No part of this thesis has been previously published. The work presented in this thesis was fully reviewed and supervised by Dr. Zaher Hashisho in the Department of Civil and Environmental Engineering at the University of Alberta. My colleagues Dr. Pooya Shariaty and Saeid Niknaddaf assisted me during the field campaign. My colleague Lucas Zhang taught me the key components of the Eddy Covariance system thoroughly. The work presented in this thesis was conducted, analyzed, interpreted, and compiled by me.

Dedication

I am thankful to my parents and my wife, Chunlei Lan, without their constant support this thesis was not possible.

Acknowledgements

I wish to show my appreciation to Dr. Pooya Shariaty, Saeid Niknaddaf and Lucas Zhang for their contributions to the field campaign. I greatly appreciate the detailed guidance and supervisory from Dr. Zaher Hashisho regarding all parts of this thesis. I also wish to thank my defense committee members, Dr. Bipro Dhar and Dr. Tariq Siddique, for their reviews and comments on this thesis. In addition, I would like to acknowledge Alberta Environment and Parks for providing the funding for this project.

TABLE OF CONTENTS

LIST OF TABLES

LIST OF FIGURES

LIST OF ACRONYMS

ABL	Atmospheric Boundary Layer
ACLP	Alberta Climate Leadership Plan
AOSR	Athabasca Oil Sands Region
ASB	Aurora Settling Basin
bLS	Backward Lagrangian Stochastic
BTEX	Benzene, Toluene, Ethylbenzene, Xylenes
CH_4	Methane
CO_2	Carbon Dioxide
CR3000	Campbell Scientific Datalogger
CSAT-3	Campbell Scientific 3-D Sonic Anemometer
CT	Consolidated Tailings
d	Day
DOY	Day of Year
EC	Eddy Covariance
EddyPro	LI-COR EC Data Processing Software
FFT	Fluid Fine Tailings
FG	Flux Gradient
FTT	Froth Treatment Tailings
g	Gram
GHG	Greenhouse Gas
GOA	Government of Alberta
GPS	Global Positioning System
ha	Hectare
Hz	Hertz
H_2	Hydrogen
H_2O	Water (Water Vapour)
IDMs	Inverse Dispersion Models
ISH	Instrument Sensible Heat
K	Kelvin Degree
L	Monin-Obukhov Length
L_{90}	90 Percent Footprint
LoggerNet	Campbell Scientific EC Data Collection Software
LI-7500A	LI-COR CO_2/Humidity Analyser
LI-7700	LI-COR CH_4 Gas Analyser
m	Metre
m^2	Metre Square
MFT	Mature Fine Tailings
MJ	Megajoule
mol	Mole

NDIR	Non-Dispersive Infrared
OP-FTIR	Open Path Fourier Transform Infrared
PA	Process Affected
ppbv	Parts per Billion by Volume
ppmv	Parts per Million by Volume
pptv	Parts per Trillion by Volume
QA/QC	Quality Assurance/Control
REA	Relaxed Eddy Accumulation
RMS	Root Mean Square
RSSI	Received Signal Strength Indicator
s	Second
SO_4^{2-}	Sulphate
STP	South Tailings Pond
t	Metric Tonne
TEA	True Eddy Accumulation
$\bar{u}$	Mean Horizontal Wind Speed
u*	Friction Velocity
UofA	University of Alberta
w	Wind Speed
WMS	Wavelength-Modulation Spectroscopy
WPL	Webb et al. (1980) Method for Density Compensation
yr	Year
z	Measurement Height of EC Tower
z/L	Stability
µmol	Micromole
°C	Celsius Degree
%	Percentage
% wt.	Percent Weight
σ_w	Standard Deviation of Vertical Wind Velocity
3-D	Three Dimensional

1.0 INTRODUCTION

1.1 Background

As an effort to minimize global warming, Alberta Climate Leadership Plan (ACLP) intends to provide a systematic approach to practically reduce Greenhouse Gas (GHG) Emission (GOA, 2017). The objectives of this plan are to reduces carbon emissions and keep the carbon tax revenue in the province of Alberta, before Ottawa introduces a federal carbon tax (GOA, 2018). Alberta is one of the areas with the highest GHG emission per capita level, and therefore has a great potential to reduce GHG emission (Ivey, 2016). Key aspects of ACLP includes: putting a price on GHG emission, phasing-out coal-generated electricity, developing more renewable energy, capping oil sands emissions to 100 megatonnes per year, and reducing methane emissions by 45% by 2025 (GOA, 2017). These key aspects of ACLP require fair and accurate quantification of current GHG emissions.

Oil sands ponds emit carbon dioxide (CO_2) and methane (CH_4) gases due to metabolism of microorganisms, and presence of organic compounds in the ponds (Small et al., 2015). Quantifying emissions from oil sands tailings ponds is challenging due to daily and seasonal variation of emissions, as well as the complexity of the continuous emission generation processes in the ponds (Wang et al., 2009). Desired quantification technologies need to provide non-point source measurements through reliable flux values collected continuously, in real time, and with full spatial coverage. Desired technologies should also offer functions such as remote monitoring to troubleshoot timely, and high frequency data collection to allow further necessary corrections during analyses. Chamber based methods (i.e. flux chamber) are conventional methods to estimate ecosystem CO_2 flux (Pavelka et al., 2018). Flux chamber methods are relatively less expensive, and easier to use. However, the flux chamber may only capture a small portion of the

surface, and it may disturb the emitting surface. Therefore, other methods are needed to cross validate or replace flux chamber measurements (Wang et al., 2009). Eddy Covariance (EC) technology for flux measurements can cover a relatively large source area, and the EC tower does not interfere with the emission and transport of fluxes originated from the source area (Burba, 2013). Commonly used methods to obtain GHG fluxes include flux chamber method, eddy accumulation method, flux gradient (FG) method, and inverse dispersion method. Other newer methods to measure GHG emissions from the tailings pond include Advanced Light Detection and Ranging (LIDAR) including Integrated Path Differential Absorption (IPDA) (Kiemle et al., 2017), Unmanned Aerial Vehicles (UAV) (Emran et al., 2017), satellite monitoring and modelling for flux estimation (Ott et al., 2015), and aerial survey for methane measurements (Baray et al., 2017).

While measurements of GHG fluxes from oil and sands tailings have historically been obtained using the flux chamber technique, the flux chamber measurement process has become increasingly labour intensive, dangerous for operators, and systematically unreliable. This thesis will assess the feasibility and reliability of EC measurement technique for measuring GHG fluxes from an oil sands tailings pond.

1.2 Objectives

The goal of this thesis is to assess the feasibility of using EC for measuring GHG emissions from an oil sands tailings pond. The main objectives of this thesis are 1) to quantify the GHG fluxes from the target tailings pond; 2) to analyse the relationships between the flux results and influential factors such as wind direction, wind speed, temperature, and diurnal variation; and 3)

to compare the GHG fluxes obtained with EC to values obtained using other flux measurement techniques.

This thesis focuses on the application of EC technique to quantify the GHG emissions from an oil sands tailings pond located north to Fort McMurray, Alberta. The GHG emissions are expressed in form of flux measurements for two parameters, CO_2 and CH_4. The tasks include a two-month field measurement during summertime, data processing and analyses, and comparison to relevant tailings ponds emission data.

1.3 Thesis Outline

Section 2.0 of this thesis provides an overview of GHG emissions from oil sands and methods used to quantify fluxes including EC. Section 3.0 describes the methodology of this field campaign, including instrumentation of EC system, data processing techniques, and quality assurance/control (QA/QC) procedures. Section 4.0 provides site description and instrument setup of this field campaign. Section 5.0 presents the flux, concentrations of both CO_2 and CH_4. Section 6.0 discusses the results, the relation between fluxes and influencing factors, analyses of the limitation of EC method, recommendations for potential improvements of flux measurements for tailings pond, and comparison of flux measurements of this field campaign to values obtained with other flux measurements techniques. Finally, section 7.0 concludes the procedures and findings of this thesis.

2.0 LITERATURE REVIEW

2.1 Atmospheric Boundary Layer

Troposphere is the lowest layer of atmosphere above the earth surface. While troposphere has an average altitude of 11 km, earth surface only impacts the lowest few kilometres of the troposphere. Therefore, atmospheric boundary layer (ABL) is a crucial part of troposphere that can be affected by physical properties of earth surface with a timescale of about an hour or less (Stull, 1988). Figure 2.1 shows the concept of the atmospheric boundary layer. Figure 2.1 shows that the troposphere is a combination of boundary layer and the free atmosphere above it, with tropopause as the top cover. An EC system typically works inside the surface boundary layer of the ABL, which is around 20-50 m high above earth ground during unstable condition and is around few tens of meters in stable stratification (Foken, 2008).

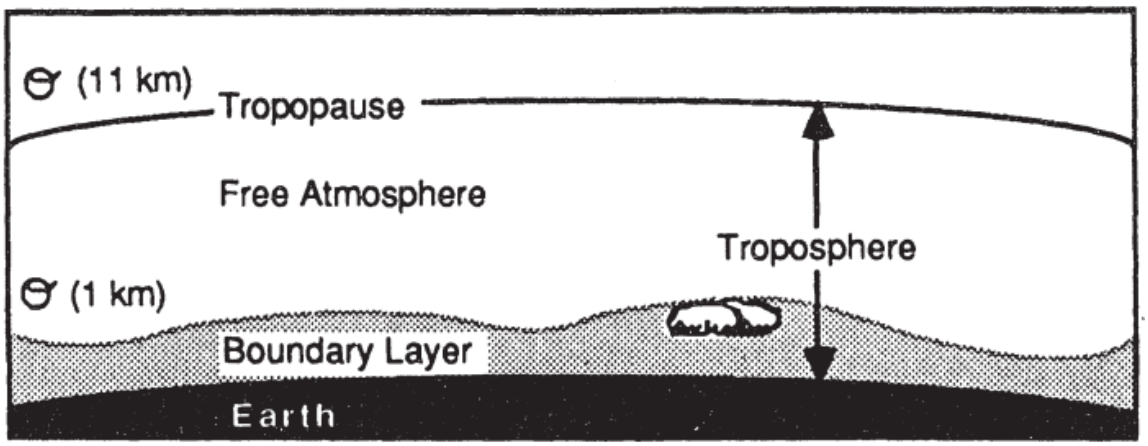

Figure 2.1. Conceptual figure of troposphere (taken from Stull, 1988)**.**

2.2 GHG Characteristics and Production

CO_2 and CH_4 are two important GHGs since they are both common product of anthropogenic activities, while being relatively persistent in the atmosphere (Soloman et al., 2010). In terms of

impacts on global warming, CH_4 is 25 times more effective than CO_2 (IPCC, 2007). In the context of oil sands tailings, CO_2 may contribute to faster de-watering of the tailings pond (Famakinwa, et al., 2018). Methane production also positively affects tailings densification, which accelerates operational water re-use in tailings pond (Stasik and Wendt-Potthoff, 2016). However, methane may fasten transport of toxic materials in deeper tailings to the upper water surface (Stasik and Wendt-Potthoff, 2016).

Microbial communities allow fermentation of n-alkane and monoaromatics to produce hydrogen (H_2) and acetate. Acetate can further break down to produce more H_2 and CO_2 (Siddique et al., 2011). Presence of Sulphate (SO_4^{2-}) may inhibit the process of methanogenesis, and therefore limit the production of CH_4. However, after enough time, sulphate level may decrease in tailings pond (Small et al., 2015), and therefore allow methanogenesis which consumes products of fermentation (acetate and H_2/CO_2) (Stasik and Wendt-Potthoff, 2016).

The oil sands mining activities involve surface mining of oil sands, then extracting bitumen from the oil sands with Clark Hot Water Extraction processes (Siddique et al., 2007). The bitumen extracted from the oil sands is viscous, therefore a diluent solvent (e.g. naphtha) is necessary to prepare bitumen for further upgrading to synthetic crude oil. Figure 2.2 shows the typical generation process of tailings from oil sands open pit mining operation.

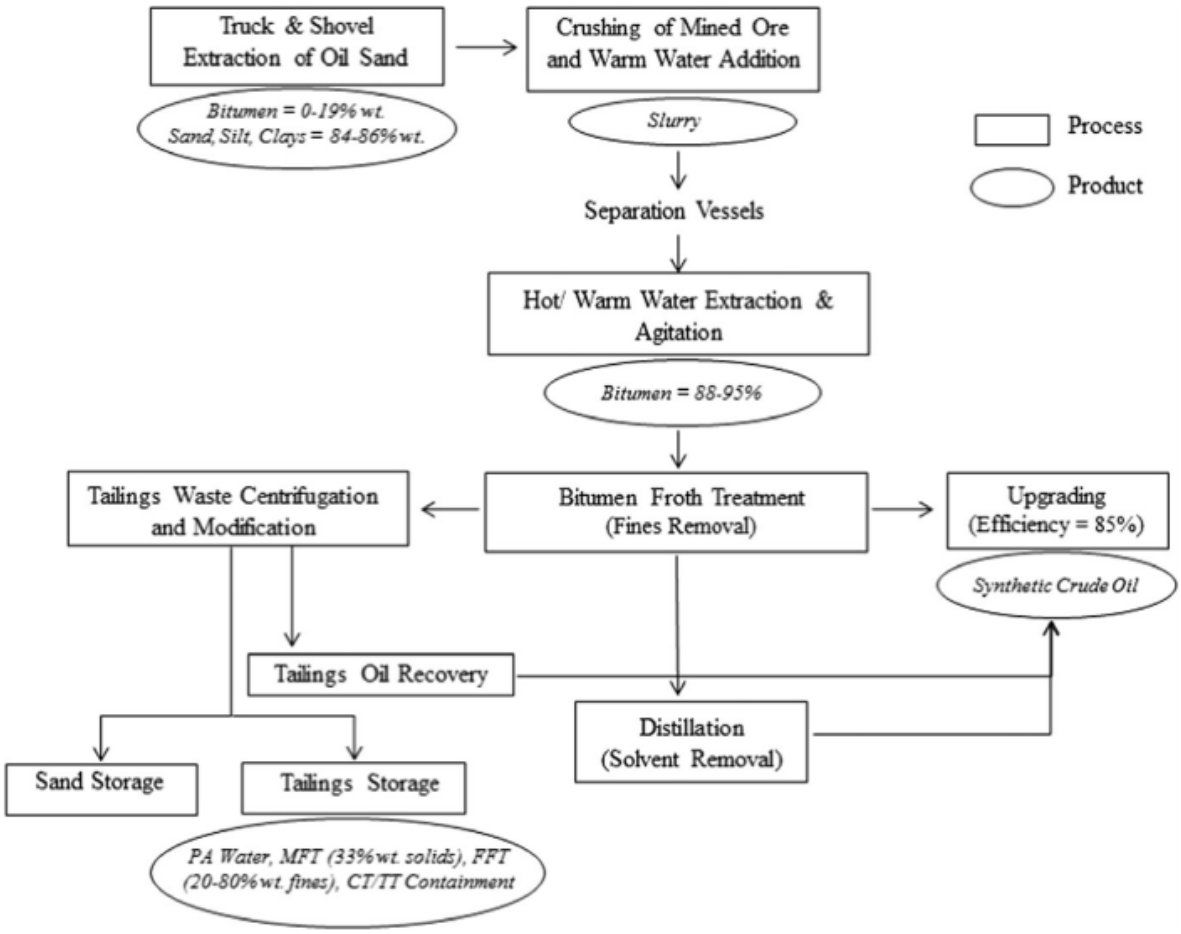

Figure 2.2. General open-pit mining operation and tailings generation (adapted from Small et al., 2015)**.**

In Figure 2.2, waste tailings are generated after crushing, extraction, and principal treatment processes such as fines removal and centrifugation. Tailings storage then contain process-affected (PA) water, mature fine tailings (MFT), fluid fine tailings (FFT), and/or consolidated tailings (CT) with variable percentages among facilities. MFT is different from FFT in terms of the percent weight (% wt.) of solids and fines. A portion of applied diluent may remain in the FTT treatment stream and eventually is diverted to the tailings ponds (Small et al., 2015). These tailings are transported to settling basins to form tailings ponds. The dewatering process of the

tailings pond will recycle water at the surface of the settling pond for further extraction processes, however, the solids content will increase to form MFT.

The major organic material in the MFT is unrecovered bitumen from the extracted tailings. However, the bitumen is relatively more resistant to rapid biodegradation process, which is the key for GHGs generation such as CO_2 or CH_4. Some of the lower molecular weight aliphatic and monoaromatic hydrocarbons in the MFT are derived from the diluent, (Siddique et al., 2007). Majority of the diluent used in the bitumen extraction process is recovered and recycled. However, a small amount of the diluent may end up in the tailings, and is the major source of methanogenesis, which generates GHGs, especially CH_4. Diluents used in oil sands tailings extraction process are a mixture of aliphatic and aromatic hydrocarbons (naphtha), or a mixture of alkanes and isoalkanes mainly as pentanes and hexanes (paraffins) (Siddique et al., 2007). The microbial metabolism of benzene, toluene, ethylbenzene, and xylene (BTEX) and n-alkanes can generate GHGs based on the following theoretical methane production revealed as stoichiometric equations (Siddique et al., 2007; Siddique et al., 2008).

$$\text{n-Hexane } C_6H_{14} + 2.5\ H_2O \rightarrow 1.25\ CO_2 + 4.75\ CH_4$$

$$\text{n-Heptane } C_7H_{16} + 3.0\ H_2O \rightarrow 1.50\ CO_2 + 5.50\ CH_4$$

$$\text{n-Octane } C_8H_{18} + 2.5\ H_2O \rightarrow 1.25\ CO_2 + 4.75\ CH_4$$

$$\text{n-Nonane: } C_9H_{20} + 4\ H_2O \rightarrow 2\ CO_2 + 7\ CH_4$$

$$\text{Benzene: } C_6H_6 + 4.5\ H_2O \rightarrow 2.25\ CO_2 + 3.75\ CH_4$$

$$\text{Toluene: } C_7H_8 + 5\ H_2O \rightarrow 2.5\ CO_2 + 4.5\ CH_4$$

Ethylbenzene, xylenes: $C_8H_{10} + 5.5\ H_2O \rightarrow 2.75\ CO_2 + 5.25\ CH_4$

The generation of GHGs varies depending on the composition of MFT, and the microbial community residing in the combination of tailings and MFT (Siddique et al., 2008). Under anaerobic conditions such as a tailings pond, the microbial community in the MFT, is capable of consuming major components of naphtha under methanogenic conditions to produce GHGs emissions.

The target tailings pond in this thesis utilizes naphtha as the main diluent solvent (Small et al., 2015). The surface mining of Alberta bitumen is certainly affecting a large portion of surface land (Burkus et al, 2014). In 2016, tailings ponds covered 257 km^2 including dykes, berm, and beaches. About 103 km^2 of the pond surface is covered with process-affected tailings water, which has potential to contribute to fugitive GHGs emission into the atmosphere (GOA, 2016).

Based on historical observations, the total GHG CO_2 equivalent (CO_2 eq) emission intensity from the oil sands tailings pond ranges from 0.08 to 1.53 grams of CO_2 eq per megajoule (MJ) of bitumen produced, or from 1.00 to 16.1 kilograms of CO_2 eq per litre of diluent applied during tailings production. In terms of flux emission intensity represented as tonne of CO_2 eq per hectare per year, the emission intensity ranges from 4.6 t/ha/y to 603.5 t/ha/y (Burkus et al., 2014). Among all the 2012 emission intensity data of the monitored tailings pond shown in Burkus et al. (2014), Suncor Pond 2/3 has an emission intensity of 258.1 t/ha/y, which sits in the middle of all the monitored fugitive emission intensities from Alberta tailings ponds.

Small et al. (2015) has summarized the CO_2 and CH_4 emissions from major oil sands tailings ponds within the Athabasca oil sands region (AOSR), which has approximately 80 percent of oil

sands activities in Alberta. Owners of the listed tailings pond are Suncor Energy Ltd., Syncrude Canada Ltd., and Canadian Natural Resources Ltd. (Table 2.1).

Table 2.1. Summary of CO_2 and CH_4 emissions from oil sands tailings management areas (adapted from Small et al., 2015)**.**

Tailings Pond*	CO_2 (t/ha/y)	CH_4 (t/ha/y)
1A	17.66	1.25
2/3	59.69	9.45
5	46.53	0.19
6	3.71	0.04
7	4.47	0.03
8A	7.66	0.13
8B	66.06	0.32
STP	23.46	0.06
East In-Pit	23.26	0.06
West In-Pit/BML	88.07	3.32
MLSB	52.85	26.22
SWSS	10.92	0.04
Aurora In-Pit	497.88	0.13
ASB	31.55	0.00378
MRM ETF	4.35	0.09
MRM In-Pit Cell 1A	156.74	0.48
JPM sand cell 1	35.36	0.55
JPM thickened tails	12.29	0.55
Horizon	30.25	0.29

* STP stands for South Tailings Pond; BML stands for Base Mine Lake; MLSB stands for Mildred Lake Settling Basin; SWSS stands for Southwest Sands Storage; ASB stands for Aurora Settling Basin; MRM stands for Muskeg River Mine; and JPM stands for Jackpine Mine.

Micrometeorological flux measurement techniques such as EC have not been commonly used at Alberta's oil sands tailings ponds (Zhang et al., 2019). Researchers have conducted few flux measurements of GHG from oil sands tailings ponds by EC. Zhang et al. (2019) used the EC technique over one of the tailings ponds located in the AOSR in 2014. Mean CH_4 and CO_2 emission fluxes were 4.56×10^{-2} g/(m^2d) and 3.59 g/(m^2d) respectively. You et al. (2021) performed GHG flux measurements on the same tailings pond as the one studied in this thesis.

The comparison between the results from You et al. (2021) and the result of University of Alberta (UofA) campaign in 2017 is presented in Section 6.4 of this thesis.

2.4 Flux Measurement Technologies

2.4.1 Flux Chamber

Implementation of chamber measurements of scaler gas fluxes between the land surface and the atmosphere started almost a century ago (Pavelka et al., 2018). Chamber techniques have been successfully utilized for GHGs estimations, including CO_2, CH_4, and N_2O. Generally, chamber methods are low cost, and easy to operate. In the case of CH_4 flux measurement, CH_4 gas analyser with high frequency and high accuracy has only been developed recently (Pavelka et al., 2018). Therefore, flux chambers provided the majority of CH_4 flux data. However, flux chamber methods produce relatively less appropriate flux measurements than EC method, and have certain limited conditions.

Conventional closed chamber is the most common method for GHG measurement from agricultural soils (Kumar et al., 2017). Placing a closed chamber over the soil surface with proper volume control would capture the short-term emission or uptake of trace gas from the soil. As the volume of air exchange across the covered surface is known, the net emission or uptake of the trace gas would be determined from the change in the trace gas concentration. Figure 2.3 illustrates a common setup for closed chamber implementation.

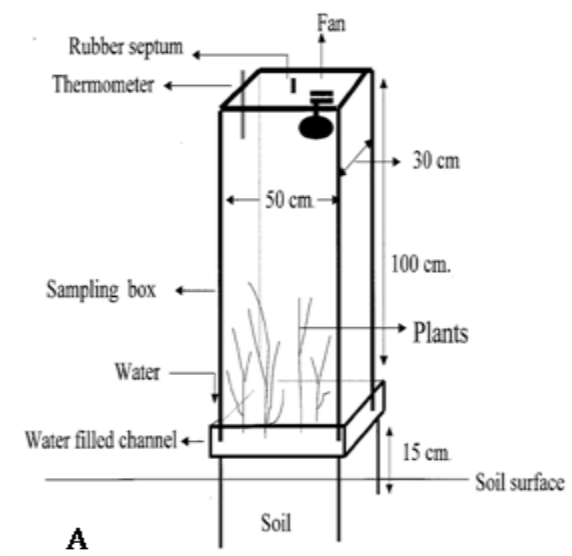

Figure 2.3. Closed chamber setup (taken from Kumar et al., 2017)**.**

As shown in Figure 2.3, based on the type of soil surface, both water, and plants could be included in the closed chamber during emission or uptake measurements. The dimensions of a chamber could vary extensively based on the objectives of flux measurements (Pavelka et al., 2018). Both temperature and pressure measurements are necessary for the flux calculations. The flux is calculated from this change using either a linear or non-linear fit model.

However, according to Pavelka et al. (2018), different ecosystem requires different chamber designs. The adjusted floating chamber method can be applied to measure diffusive flux from the surface of aquatic ecosystems (Goldenfum, 2010). Figure 2.4 presents the conceptual sketch of a floating chamber system.

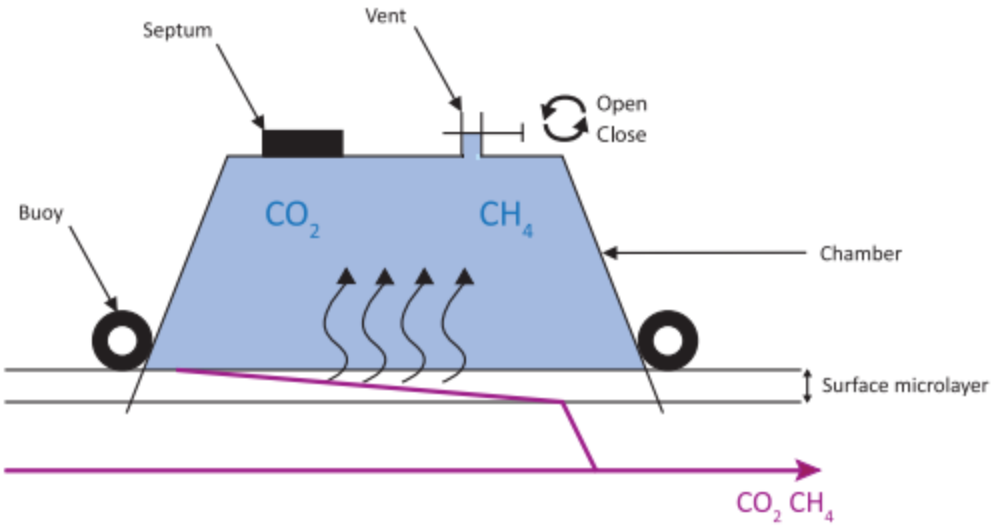

Figure 2.4. Conceptual sketch of a floating chamber (taken from Goldenfum, 2010)**.**

As shown in Figure 2.4, the chamber is designed to float on the surface of aquatic ecosystem instead of covering the soil surface. Diffusive fluxes are affected by the concentration gradient between the aquatic surface microlayer and the atmosphere, and other variables such as wind speed and rainfall events (Goldenfum, 2010). Floating chambers must have walls extending below the water surface to prevent the chamber drifting during calm wind periods. Chamber drifts caused by friction between the edges of the chamber and the water surface can create more turbulence than nature, therefore creates higher flux measurements than nature. A vent is also necessary on the top of the chamber to make sure chamber pressure is the same as the air pressure before any measurements. The cover material of the chamber should be reflective to avoid considerable temperature variation inside the chamber (Goldenfum, 2010).

In general, the flux chamber measurement technique is low cost and easy to operate, however, the flux chamber can only cover a small portion of the water surface. Since the coverage of a flux chamber is limited to the footprint of the chamber bottom surface area, the results from flux

chambers may not reflect the spatial variability of the fluxes from the target source (Denmead, 2008). Flux chambers are used to measure the flux from a small sample area (typically 0.13 m^2) for a short duration (typically 0.5 to 1 hour), which may not account for the variability in emissions over time or over a non-uniform area source such as an oil sands tailings pond (Small et al., 2015).

The flux chamber relies on the transfer of the target gas from water surface to the atmosphere. For closed flux chambers, the increased gas concentrations in the chamber can restrain further flux emission from the water surface to the flux chamber (Denmead, 2008). This limitation of closed flux chamber may cause reduction of measured emission of the target gas from the target water surface. Flux chamber is also an invasive method as it may physically impact the water surface and the extended water body of the footprint area. The physical contact and source disturbance may cause uncertainty in the final flux measurements results as well.

Additionally, the oil sands tailings ponds are difficult to access for flux chamber deployment. The oil sands tailings are hazardous materials and therefore the tailings water and tailings dusts are hazards for flux chamber operations. Riding a boat may be the only way to setup a flux chamber system for the tailings pond, and extra safety measures such as dust masks, goggles, and safety vests are necessary for the flux chamber operations.

2.4.2 Eddy accumulation

The true eddy accumulation (TEA) (Baker et al., 1992) technique is closely related to the EC technique if no high frequency gas analysers are available for EC measurements. The TEA method requires an anemometer measuring at least the vertical wind speed. After the air flow is

directed through the anemometer, it will be diverted to updrafts and downdrafts for sampling and analyses. A typical flowchart of TEA method is shown below as Figure 2.5.

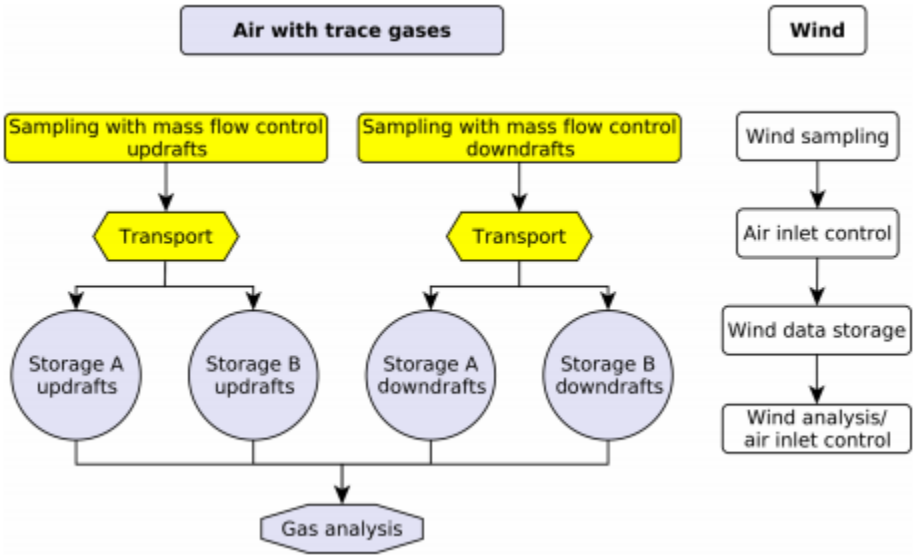

Figure 2.5 Schematic flowchart of TEA system (adapted from Siebicke and Emad, 2019)**.**

Figure 2.5 shows air containing trace gases is diverted into updraft and downdraft with mass flow control, then all the samples will stay in the storage areas before they are analyzed by the same gas analysers. While wind data is recorded properly and will be analysed corresponding to the wind samples diverted to the updrafts and downdrafts. The general equation utilized in TEA is the same as the general flux equation for EC calculations. In contrast to EC, the separate sampling of the wind and scalar time series is no longer possible, therefore physical collection of separate air samples of updraft and downdrafts proportionally to the magnitude of the vertical wind velocity is applied (Siebicke and Emad, 2019). A practical implementation of TEA determines the scalar of interest as half of the difference between the mole fraction of the scalar in the updraft reservoir, and the mole fraction of the scalar in the downdraft reservoir, then

multiplied by the mean of the absolute value of vertical wind velocity, assuming mean vertical wind velocity is nearly zero. At the end of each sampling period, the updraft or downdraft trace trace gas concentrations are measured with a high-resolution gas analyzer to obtain the gas flux, F_g (Denmead, 2008).

$$\overline{F_g} = \overline{w_u \rho_{g,u}} - \overline{w_d \rho_{g,d}}$$

In above equation, w_u and w_d are the vertical wind speed for the updrafts sampling period and downdrafts sampling period, $\rho_{g,u}$ and $\rho_{g,d}$ stand for the gas concentrations of the updrafts and the downdrafts.

Since the formulation of TEA is challenging, Businger and Oncley (1990) proposed a modified version of eddy accumulation, as relaxed eddy accumulation (REA). The idea of REA is based on the concept of flux-variance similarity, which relates the scalar flux to the variance of the vertical wind velocity, through a proportionality factor. REA requires a fast-response anemometer to measure w, and air is sampled at a constant flow rate. The gas flux can then be calculated as the following equation (Denmead, 2008).

$$\overline{F_g} = b\sigma_w(\rho_{g,u} - \rho_{g,d})$$

Where in above equation, b is the coefficient representing the proportionality factor, and σ_w is the standard deviation of w. Typical b values are around 0.55 and ranging from 0.4 to 0.7 based on observations from various independent measurements and simulations (Siebicke and Emad, 2019). The coefficient range can be a significant uncertainty during practical measurements of fluxes using REA approach.

2.4.3 Flux Gradient Method

The classic flux gradient (FG) technique relies on the similarity of turbulent diffusion coefficients for gases combined with heat or momentum information (Laubach and Kelliher, 2004). The similarity theory (K-theory) assumes the surface-layer air flow is ideal, which means a steady and horizontally homogeneous surface flow. The homogeneous flow dynamics properties include the surface fluxes of momentum, sensible heat, and latent heat. In ideal surface-layer air flow, the vertical flux of an entity, c (such as methane) can be calculated by introducing the turbulent diffusivity, K_c (Laubach and Kelliher, 2004):

$$F_c^{FG} = -K_c \frac{\partial s}{\partial z}$$

In this equation, z represents the height above the mean zero-plane, F_s is the vertical flux of s at height z, and the superscript FG indicates the Flux Gradient technique in use. The estimate of diffusivity, K_c for methane gas, can be obtained by the similarity theory. In ideal condition, the similarity theory states the diffusivity of momentum, heat, and passive tracers (including gas concentration) are equal. Therefore, if heat or momentum fluxes can be measured by equipment such as a sonic anemometer, the diffusivity of the passive tracer can be obtained (Laubach and Kelliher, 2004). Experimental evidence has already suggested the diffusivity of heat K_h equals diffusivity of methane K_c at all stabilities (Dyer and Bradley, 1982), hence one options to calculate K_c was developed based on heat diffusivity:

$$K_c = K_h = -F_T \left(\frac{\partial T}{\partial z}\right)^{-1}$$

Another option based on momentum diffusivity can be developed:

$$K_m = ku^* z\varphi_h^{-1}$$

In the momentum equation, k = 0.4 is the von Kármán constant and u^* is the friction velocity. By combining the above heat equation and momentum equation, the K_c function now can be expressed as:

$$K_c = K_h = ku^* z\varphi_h^{-1}(\frac{z}{L})$$

where u^* and the Monin–Obukhov length, L are derived from the sonic anemometer data. φ_h is the Obukhov stability function for heat as specified by Kaimal and Finnigan (1995), based on Dyer (1974) and the revision of Högström (1988).

2.4.4 Inverse Dispersion Fluxes

The inverse dispersion models (IDMs) are applied for deriving emission flux estimates based on line or point measurements downwind of the source area (You et al., 2021). The emission rate estimated by using IDMs is obtained by the following equation.

$$Q = \frac{(C - C_b)}{\left(\frac{C}{Q}\right)_{sim}}$$

Where C is the mole fraction of the tracer gas measured, C_b is the background mole fraction (measured upwind of source) and $(C/Q)_{sim}$ is the simulated ratio obtained from a backward Lagrangian stochastic (bLS) model. Combined with open-path Fourier transform infrared (OP-FTIR) technique for concentration measurements, inverse dispersion can be used to estimate the emission flux from a source area (You et al., 2021).

2.4.5 Aerial Survey for GHG Measurements

Aerial survey is a top-down measurement of GHG emissions, which can help in verification of bottom-up emission inventories established from specific sources (Baray et al., 2017). Aircraft based aerial survey of GHG measurements applies mass balance approach to determine total CH_4 emissions rate for the target sources. During an aircraft survey, a gas analyzer can measure the concentration values of CH_4, CO_2, CO, and H_2O. Other necessary parameters such as temperature, dewpoint temperature, wind speed and pressure can be measured by corresponding probe, hygrometer, and sensor. Geospatial information such as latitude, longitude, and ellipsoid height altitude are usually provided by a Global Positioning System (GPS). Measurements are performed during designed flights for target source areas, which includes two patterns: screen flights and box flights.

Emission rates then can be determined based on mass-balance approaches, such as a Top-down Emissions Rate Retrieval Algorithm (TERRA), or a second mass-balance approach using downwind flight tracks to spatially separate CH_4 emissions from different sources.

2.5 Eddy Covariance Flux Measurement

EC system performs flux measurements between a flat, horizontally homogeneous surface and the above atmosphere. The covariance between turbulent fluctuations of the vertical wind and the quantity of interest (e.g. GHG) can describe the one-way net transport between the investigated surface and atmosphere (Aubinet et al., 2012). EC system becomes mature and practically manageable after sonic anemometer development was advanced in 1980s. In parallel, the development of new gas analyzer types allowed an extension of the investigated trace gas

spectrum. Infrared analyzer and Tunable Diode Laser provide the possibility for high-frequency measurements of CO_2 and methane gases (Aubinet et al., 2012).

Convective horizontal air flow can carry numerous rotating eddies along with the horizontal wind direction. Each eddy has three dimensional characteristics, including a vertical component. By measuring gas concentration, temperature, humidity, and the speed of the vertical air movement of each eddy, monitors can estimate the vertical upward or downward fluxes of gas (including GHGs) and water vapor concentrations, temperature, and humidity. For example, according to Burba, (2013), if at one moment that three molecules of CO_2 went up, and in the next moment only two molecules of CO_2 went down, then the estimated net flux over this time was upward, and equal to one molecule of CO_2. The following equation is the classical equation for eddy flux.

$$F \approx \overline{\rho_d}\,\overline{w's'}$$

Where F is the flux of a certain gas, ρ_d is dry air density, w' is the instantaneous deviation in vertical wind speed and s' is the instantaneous deviation in mixing ratio (or dry mole fraction) of a certain gas. Generally, this equation means flux is equal to the product of the mean air density and the mean covariance between instantaneous deviations in vertical wind speed and mixing ratio (Burba, 2013), as covariance is defined as a measure of the strength of the correlation (Snedecor and Cochran, 1980) between the derivation of the vertical wind speed and the instantaneous deviation of gas concentration.

2.5.1 Reynolds Decomposition

Reynolds decomposition is a mathematical technique used to separate the expectation value of a quantity from its fluctuations. EC system is based on Reynolds decomposition, and therefore includes ergodic hypothesis which assumes that time averages are equal to ensemble averages. To fulfil this assumption, the fluctuations must be statistically stationary during the averaging time chosen. This assumption may not be true and may be a limitation of this technique (Aubinet et al., 2012).

2.5.2 Major Assumptions

For a specific atmospheric constituent of interest (such as CO_2 and CH_4), factors relative to the rate of change of the quantity are atmospheric transport, molecular diffusion, and source/sink. Where atmospheric transport, and source/sink are dominant factors in EC measurement system, molecular diffusion is often negligible for EC system calculation (Aubinet et al., 2012).

Other assumptions in EC theory includes constant dry air density in time-averaging period, zero wind velocity perpendicular to the average velocity, zero vertical wind velocity, horizontal homogeneity (nullify horizontal gradients) and steady state conditions (Aubinet et al., 2012). Under these assumptions, measured flux represents the source/sink of the target gas, and is constant with height. EC flux calculations also assume the molecular density and turbulent fluxes measured by the tower are representative of the whole control volume of the Scalar Budget Equation (Aubinet et al., 2012).

2.6 Flux Footprint

Calculations from flux footprint models may describe the spatial coverage of the emission source contributing to the corresponding turbulent flux measurements. Footprint analyses is crucial for

flux measurements of CO_2, water vapour (H_2O), and CH_4, and is already a standard task for measurements from flux towers (Kljun, et al., 2015). Three main factors affecting the size and shape of flux footprint are measurement height, measurement distance from the source, characteristics of surface boundary layer (surface roughness), and atmospheric thermal stability (Schuepp et al., 1990).

3.0 METHODOLOGY

3.1 Instrumentation

The EC system consists of four major components: a 3-D sonic anemometer for wind speed measurements (Campbell Scientific CSAT-3); an open-path CH_4 gas analyser utilizing wavelength modulation spectroscopy (WMS) (LI-7700); an open-path CO_2/humidity analyser using non-dispersive infrared (NDIR) detection (LI-7500A); and a datalogger (Campbell Scientific CR3000) to store and synchronize all valuable data from the previous three components.

The 3-D sonic anemometer (CSAT3) measures the three dimensional meteorological wind velocity components. The sonic anemometer uses a fine-wire thermocouple mounted on a stainless steel bayonet for high frequency (up to 20 Hz) temperature measurements. The sonic anemometer measures three components of wind speeds through utilizing the ultrasonic signal emitted and received by the three non-orthogonal sonic axes. The sonic anemometer determines wind speeds and the speed of sound by measuring the travel time of ultrasonic sound between the three pairs of transducers mounted on the sonic axes.

The open-path CH_4 gas analyser (LI-7700) applies the Beer Lambert Law to measure methane concentration with high frequency (up to 40 Hz) and high precision. The precision can reach a root mean square (RMS) of 5 parts per billion by volume (ppbv) at 10 Hz frequency at typical ambient conditions (LI-COR, 2020). The CH_4 gas analyser operates based on the principle of Beer Lambert Law, which describes the absorption of radiation by a gas sample (in this case, CH_4), combining with WMS, the CH_4 gas analyser laser scans the absorption band of CH_4 to convert the absorption rate of CH_4 to CH_4 concentrations. LI-7700 has a physical optical path of

0.5 m between upper mirror and the lower mirror. The laser travels 60 repetitive passes in a Herriott cell pattern for a total path length of 30 m to better capture the variations of the absorption rate. LI-7700 also measures the ambient temperature and pressure of the sampling volume through a fine-wire thermocouple on the upper mirror and a pressure transducer installed below the lower mirror. The gas analyser also records the laser signal strength named as Received Signal Strength Indicator (RSSI) as a dimensionless number. The RSSI can be used to indicate the operational condition of the gas analyser, which can inform quality assurance/quality control (QA/QC) and mirror cleaning/heating decisions. The LI-7700 CH_4 analyser is factory-calibrated. The calibration range of LI-7700 analyser are 0-25 ppm at -25 ºC, 0-40 ppm at 25 ºC and 0-50 ppm total range (LI-COR, 2020).

The open-path CO_2/H_2O gas analyser (LI-7500A) measures both CO_2 and H_2O concentrations as the sampling volume pass through the upper mirror and lower mirror of the device (LI-COR, 2009). The LI-7500A measurement principle based on Beer Lambert Law is the same as the CH_4 gas analyser, with the same maximum measurement frequency at 40 Hz. Also, the precision of LI-7500A in terms of RMS noise is high, and corresponds to 0.11 ppmv for CO_2 measurement and 0.0047 pptv for H_2O at 10 Hz frequency. The LI-7500A CO_2 analyser is factory-calibrated. The calibration range of the CO_2 analyser is from 0 to 3000 μmol per mol.

The datalogger (CR3000) operates with a modem to enable daily communication with distant operator. The EC setup ensures capturing high frequency (10 Hertz) volume concentrations and meteorological data required for flux emission calculations. Two solar panels are selected to supply majority of power requirements of the operation. LI-7700 operates with self cleaning

optics. In addition, both LI-7700 and LI-7500A have air nozzles system for dust clean up. Datalogger stores data in binary form in one 2-Gigabytes (GB) secure digital (SD) card.

3.2 Post Measurement Data Processing Procedure

The Card Convert function of LoggerNet (Campbell Scientific EC data collection software) converts the collected binary form data into text form data. EddyPro (LI-COR EC data processing software) version 6.2 can process the text form data directly with 30 minutes time averaging period (LI-COR, 2016). Appendix A shows the calculation processes for important metadata for EddyPro data processing. In this thesis, Section 4.2 shows detailed description of the metadata.

EddyPro version 6.2 (LI-COR Inc.) was utilized for all flux calculations and corrections. Table 3.1 summarizes all the choices made in advanced setting for EC flux calculations, and other options available for selections. As default, advanced setting utilizes spike count/removal, amplitude resolution test, drop-outs, absolute limits, then skewness and kurtosis tests for statistical analyses. Spectral corrections include low frequency range analytic correction of high-pass filtering effects (Moncrieff et al., 2004), and high frequency range correction for short and heated sampling lines (Moncrieff et al., 1997). The ISH correction ("add instrument sensible heat (ISH) components") in the compensation for density fluctuations option is significant for CO_2 measurements during cold meteorological condition (Burba et al., 2008). George Burba, (personal communication, July 11, 2018) suggested presenting calculated data with the ISH correction is possible even for high temperature measurement. Since the general CO_2 flux is small compared to the terrestrial measurements of previous research (Burba et al., 2008), and the

instrument sensible heat flux may be important as well. Section 5.0 will also present all flux values without the option ISH correction selected for more comprehensive interpretations.

Table 3.1. Summarized advanced setting choice in EddyPro flux calculation.

Processing Options	Option Selected	Other Option(s)
Wind speed measurement offsets	Offsets obtained from zero-span test	N/A
Axis rotation for tilt correction	Double rotation method	- Triple rotation - Planar fit method
Detrending turbulent fluctuations	Linear detrending with 30 minutes time constant	- Running mean - Exponential running mean
Time lags compensation	Covariance maximization	- Constant time lag - Time lag optimization
Compensation for density fluctuations	Webb et al. (1980) (WPL) correction and "add instrument sensible heat components" correction for LI-7500A	N/A
Footprint estimation	Kormann and Meixner (2001)	- Kljun et al. (2004) - Hsieh et al. (2000)

3.3 Quality Assurance/Control (QA/QC)

EC data filtration criteria includes appropriate diagnostic numbers, wind direction from the lake (discard wind from 90° to 270°, based on the direction of sonic anemometer, please see Appendix A north offset calculation), received RSSI larger than 20%.

After advanced setting calculations, Mauder and Foken (2004), as explained in Mauder et al., 2013, suggested a flagging policy where "0" means high quality fluxes, "1" means fluxes are moderate quality data suitable for use in long term observation programs, "2" means fluxes are low quality data and may not be appropriate for further analyses.

4.0 FIELD CAMPAIGN DESCRIPTION

4.1 Site Description

The coordinates of the University of Alberta (UofA) EC tower are at 56.983369º N, 111.508506º W. Figure 4.1 shows the satellite layout of the Pond 2/3 tailings pond, with location of the EC tower. The EC tower was located at the south side of the tailings pond. The tailings water area of Suncor pond 2/3 is around 2.8 km^2. As necessary part of the oil sands operation, pond 2/3 contains Naphtha as major diluent and coarse/fine froth treatment tails (FTT) (Small et al., 2015). The field campaign started from July 28, 2017 to September 29, 2017.

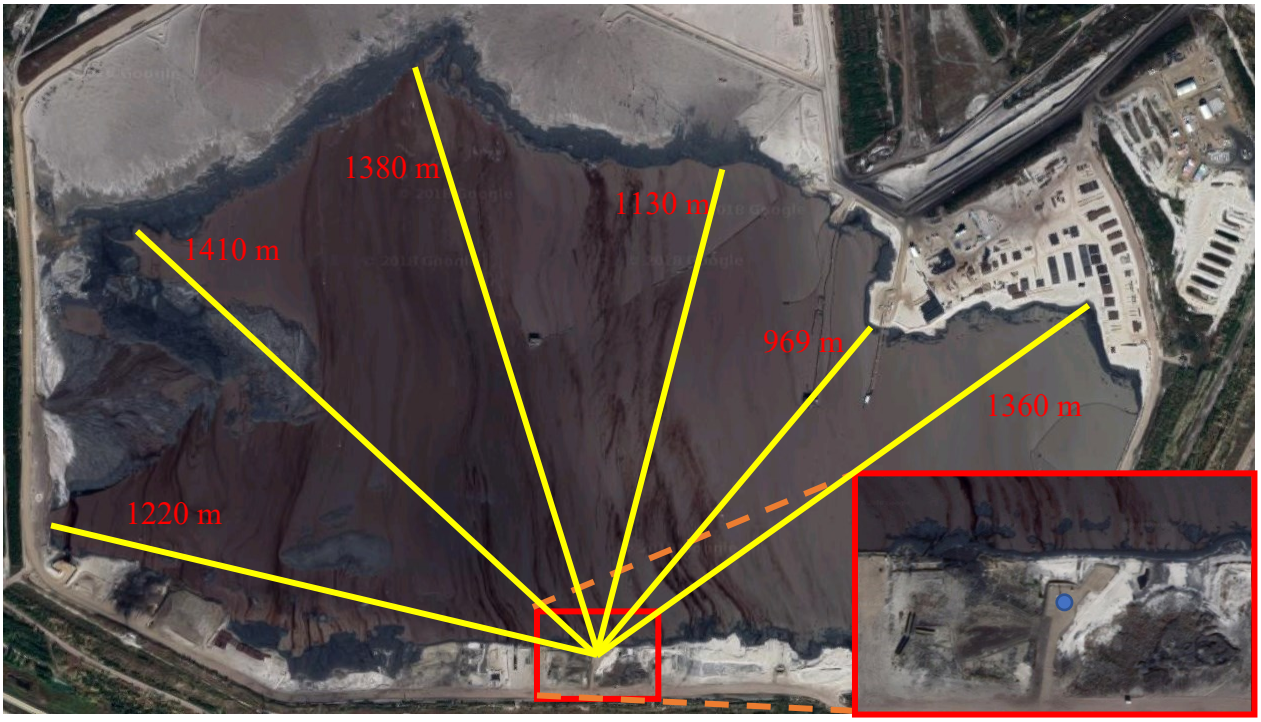

Figure 4.1. Site layout of field and location of the EC tower; zoomed in area enclosed in red rectangle indicates location of EC tower as blue dot; yellow lines with red number in unit of metre shows distance between EC tower and several edges of the water surface of pond in 2018 (Figure modified from Google Map, 2018)**.**

4.2 Instrument Setup

Installation of the EC system and supplemental devices started from July 26, 2017. The tower was palced on a gravel pad, and all EC instruments were attached to the main mast at the centre of the tower. Figure 4.2 shows the setup of the EC instruments on top of the tower. The sonic anemometer was facing north, to catch as many quality data as wind brings turbulence information from the lake (north) towards the tower (south). Appendix A depicts the metadata calculations of north offset and related magnetic declination. North offset indicates the angle between the main axis of the sonic anemometer and the true north at the measured location. The magnetic declination is necessary, since the measured degree of the CSAT3 sonic anemometer in field is relative to the magnetic north, not true north. North offset is important for wind filtration and 90% flux footprint analyses.

The gas analysers were tilted at around 10-15 degrees to naturally drain raindrops on the mirrors to reduce signal strength issues in long term. The separations between analysers and the sonic anemometer were around 20-30 cm. This ensures the analysers measure the same volume of air as the sonic anemometer, while minimizing the turbulence influence on the sonic anemometer (LI-COR, 2018). Vertical separations were controlled to be around zero during installation. Appendix A provides the measurements and calculations for separations between sonic anemometer and both gas analyzers. These separations are important for time lag calculations during data processing. Both gas analyzers and sonic anemometer operated in 10 Hertz (Hz) frequency. Figure 4.2 shows the proper separations between the sonic anemometer and both gas analysers.

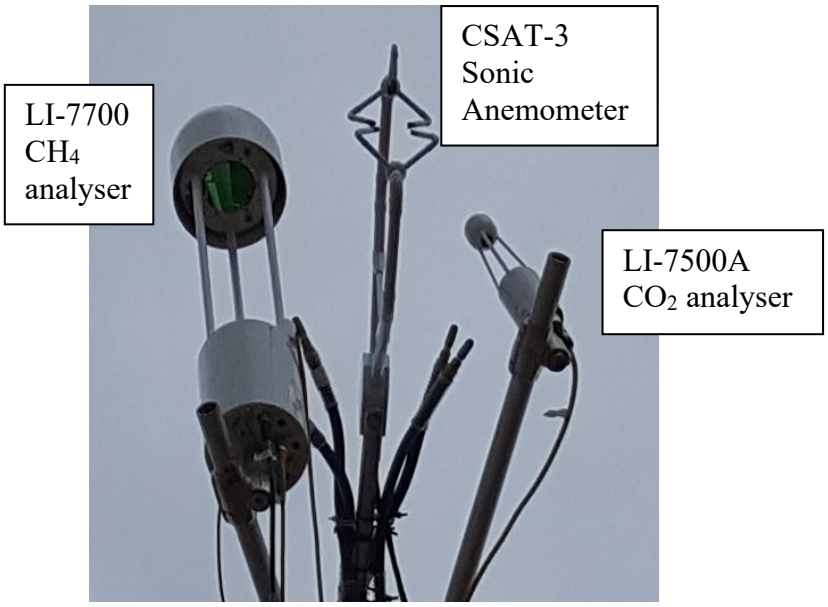

Figure 4.2. Setup of major EC instruments (LI-7700 at left, CSAT-3 in the middle, and LI-7500A all facing north).

Figure 4.3 shows the entire view of the tower setup, with supplemental device enclosures and solar panel. The centre of the sonic anemometer is at around 9.91 m above the water surface. Guy wires were attached to the tower at three different levels to secure the tower from falling. The tower height was limited by the length of the tubing between the washer reservoir (for LI-7700 optic cleaning) and the bottom mirror of LI-7700.

Figure 4.3. Photo of operating EC system and entire tower with guy wires.

5.0 RESULTS

5.1 Meteorology Condition

Time averaged wind speed measurements during this field campaign are between 0.2 metres per second (m/s) to 9.9 m/s. The maximum high frequency wind speed measured is 18.7 m/s. Figure 5.1 shows the wind rose measured by EC tower during this field campaign. In Figure 5.1, the lengths of each wedge represent the frequency of counts by wind direction in percentage, and the colours in the legend at right side indicate the different ranges of wind speeds in unit of m/s. During this field campaign, the dominant wind type is south wind, as wind blows from southwest and southeast towards north. Mean wind speed (not filtered) is around 3.035 m/s. In addition, calm wind weather (extremely low wind speed) did not occur during the field campaign.

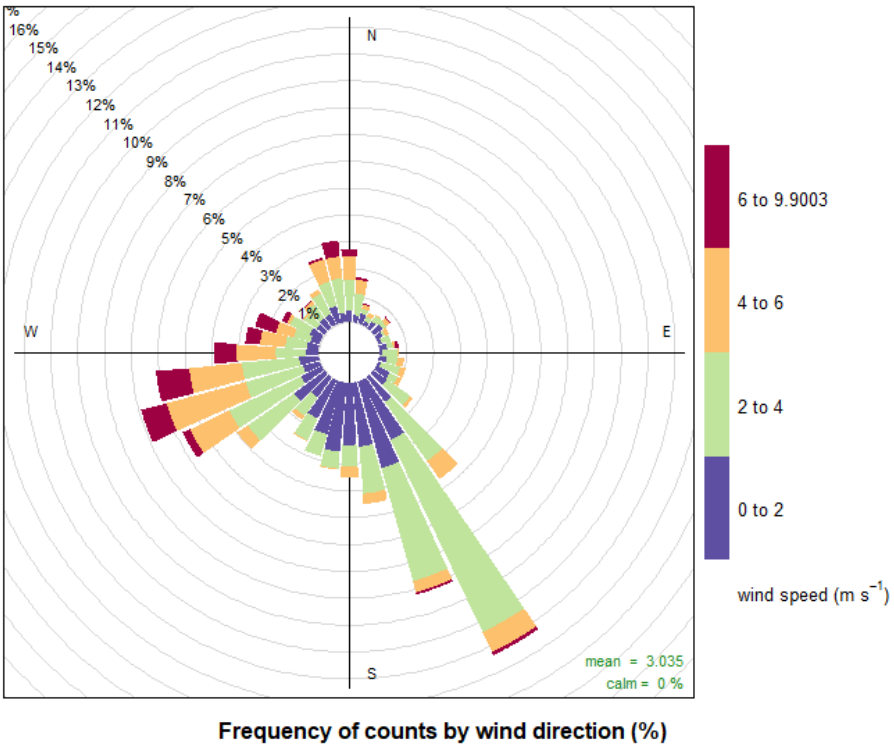

Figure 5.1. Wind rose during the entire field campaign; Colour of the wedges indicates wind speed in m/s (m s^{-1}).

Time averaged temperatures ranged from 0.5 ºC to 30.4 ºC, with an average of 15.5 ºC. Figure 5.2 shows the temperatures (in unit of degree Kelvin, K) measurements during the field campaign. July 28 of 2017. Day of year (DOY) at 209 means July 28 of 2017, and DOY at 272 means September 29 of 2017.

Figure 5.2 presents all valid temperatures measured with the CSAT-3 sonic anemometer during the field campaign. Figure 5.3 shows the zoomed in temperatures between day 235 and day 245 of the year to illustrate a clearer pattern in short time. As expected, peak temperature often occurred at late afternoon of the day, and lowest temperature often happened shortly before dawn.

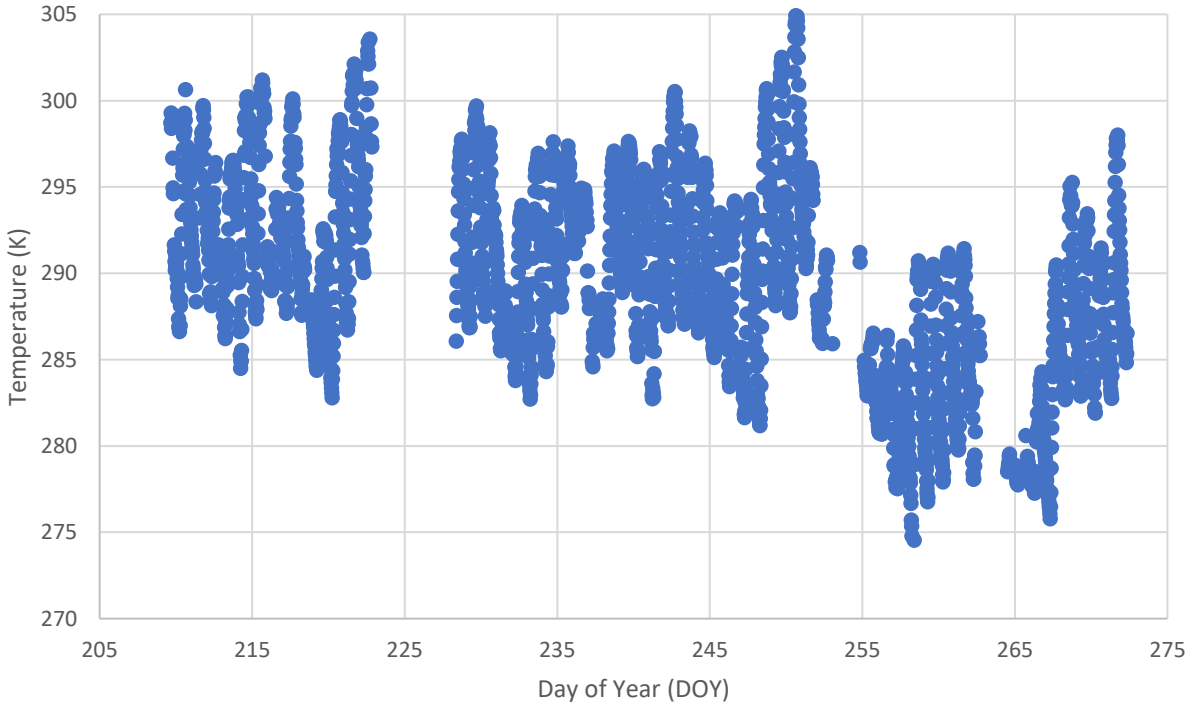

Figure 5.2. Temperature measurements during the field campaign.

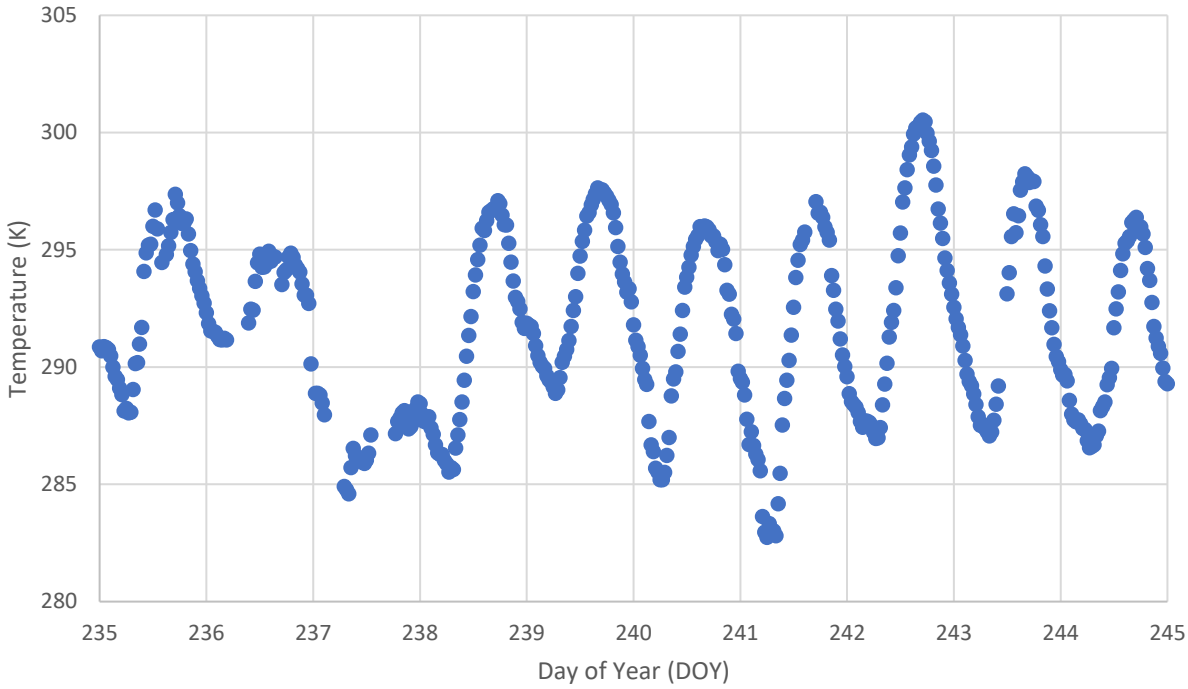

Figure 5.3. Zoom in figure showing short term temperature pattern.

EC method assumes homogeneous meteorological condition. Figure 5.4 demonstrates the relationship between normalized standard deviation of vertical velocity (σ_w/u^*) and stability (-z/L). σ_w represents the standard deviation of vertical velocity in unit of metre per second (m/s), u* represents the friction velocity (m/s), z is the measurement height in unit of (m), and L is the Monin-Obukhov length (m) (Kaimal and Finnigan, 1995). Negative stability (z/L) means the atmosphere is unstable, and positive z/L means the atmosphere is stable. In Figure 5.4, blue dots represent measured data from the EC field campaign. In addition, Kaimal and Finnigan (1995) model and Wilson (2008) models are plotted in Figure 5.4. Figure 5.4 demonstrates the field obtained data does fit patterns of both models, indicating the measured surface is undisturbed.

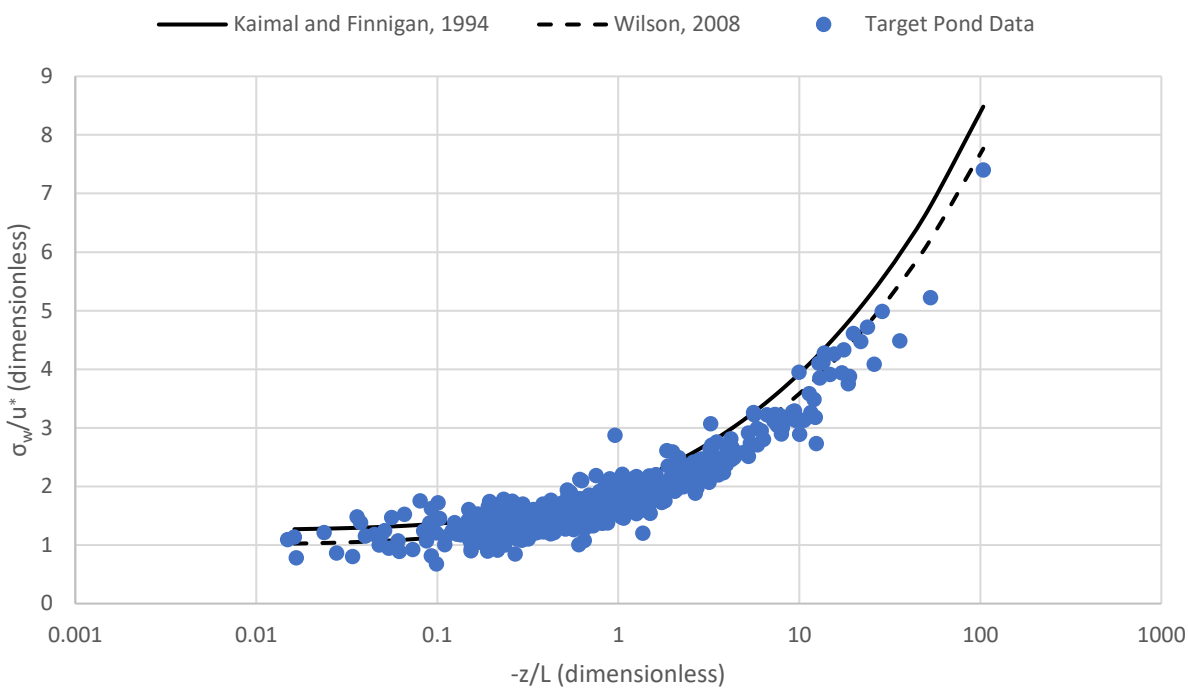

Figure 5.4. Model comparison in undisturbed surface layer.

5.2 Overview of Data Quality

Table 5.1 and Table 5.2 show the data filtration procedures for CO_2 and CH_4 flux data after EddyPro output, to account for invalid averaging time, inappropriate diagnostic numbers, wind direction, then Mauder and Foken (2004, as explained in Mauder and Foken, 2013) flagging system. Table 5.1 and Table 5.2 also present the number of data before and after each data filtration process, and percentage (%) of remained CO_2/CH_4 flux data after each data filtration processes. The "Percentage Remained" column of Table 5.1 and Table 5.2 are calculated using the "number of data after filtration" divided by the total "number of data before filtration" (which is 2699).

Table 5.1. Quantity and percentage of CO_2 data points before and after each data filtration process.

Filtration Process	Number of Data Before Filtration	Number of Data After Filtration	Percentage Remained (%)*
Invalid averaging time	2699	1975	73.18
Diagnostic filtration	1975	1973	73.10
Wind direction filtration	1973	496	18.38
Footprint filtration	496	367	13.60
Mauder and Foken (2004, explained in Mauder and Foken, 2013) flux flags	367	292	10.82

*Calculated using the "number of data after filtration" divided by the total "number of data before filtration" (which is 2699).

Table 5.2. Quantity and percentage of CH_4 data points before and after each data filtration process.

Filtration Process	Number of Data Before Filtration	Number of Data After Filtration	Percentage Remained (%)*
Invalid averaging time	2699	1974	73.14
Diagnostic filtration	1974	1972	73.06
Wind direction filtration	1972	495	18.34
Footprint filtration	495	366	13.56
Mauder and Foken (2004, explained in Mauder and Foken, 2013) flux flags	366	351	13.00

*Calculated using the "number of data after filtration" divided by the total "number of data before filtration" (which is 2699).

Table 5.1 and Table 5.2 show that the Mauder and Foken (2004, explained in Mauder and Foken, 2013) process filters CO_2 flux and CH_4 flux differently. In addition, measured CO_2 concentrations has one more valid 30 minutes averaging period than measured CH_4 concentrations.

EddyPro flag invalid data points (e.g. invalid time averaging; flux footprint estimation beyond reasonable range) with "-9999" for error label. Therefore, in Table 5.1 and Table 5.2, the invalid time averaging filtration filters out these flagged values. From August 4th to August 10th (2017), CO_2 diagnostic numbers were often above zero, indicating a chopper house temperature error (LI-COR, 2009). Therefore, diagnostic filtration filters out these CO_2 fluxes with alerting diagnostic numbers. Since WPL correction during data processing utilizes water vapour pressure and heat measurements from LI-7500A (Webb et al., 1980), therefore both CO_2 and CH_4 fluxes/concentrations (in molar ratio) need to consider the impact of LI-7500A diagnostic number. Mauder and Foken (2004, explained in Mauder et al., 2013) introduced a flagging system, and all data with level "2" flag are not suitable for further analyses. For LI-7500A data, both CO_2 and H_2O flags needs to be considered. The wind direction filtration discards all data with wind direction from 90 degrees to 270 degrees. The percentage remained column shows that wind direction filtration is the most important step for choosing meaningful values for further analyses. Footprint based data filtration discards all fluxes with 90 percentage footprint output larger than the distance from the pond boundary to EC tower. Appendix B shows the MatLab code for wind direction and footprint based data filtration.

From August 25 to August 29 (2017), the SD card available for data storage exceeded the storage limit, and therefore all data from August 10 to August 15 were lost due to data overwriting.

After the field campaign, both LI-7500A and LI-7700 went through instrument quality check during June 2018, by LI-COR instrument distributor at Lincoln, Nebraska. Based on analyses

results from LI-COR, LI-7700 methane gas analyser works properly, and meets quality specifics. However, the LI-7500A CO_2/H_2O gas analyser has condensation problem at the source lens.

5.2.1 Data Quality of CO_2 Measurements

The condensation at the source lens of LI-7500A may affect the concentration measurements and following flux calculations of CO_2/H_2O gases. According to LI-COR applications scientist James Kathilankal (personal communication, July 19, 2018), the condensation formed when a faulty sensor head cable caused water leakage in the chopper house of the LI-7500A instrument. The water leakage may have lead to short circuit, and overheating of the chopper house, which resulted in vaporizing the oil paint inside the chopper house. The vaporized oil paint may have condensate at the inner side of the source lens and reduced the signal strength of the infrared. The impact of the condensation and overheating of the chopper house may be unpredictable, and the data obtained may not represent the true concentrations of the site, and therefore may not produce reliable CO_2 flux calculations. After the condensation problem, even the diagnostic values of LI-7500A seemed trustworthy, the actual measurements may have already been affected by the condensation and may be less reliable than the measurements before the condensation problem occurred. According to James Kathilankal (2018), measurements obtained before the LI-7500A diagnostic problem may still represent valid measurements of CO_2 flux, since the condensation problem had not occurred. Therefore, comparison of the CO_2 measurements before the diagnostic problem on August 3rd of year 2017, and the CO_2 measurements after the diagnostic problem could help understand how the condensation issue affected the data collected after August 3, 2017. In Section 5.3 and Section 5.4, concentration

measurements and flux measurements of CO_2 before the end of August 3rd are compared to measurements of the entire field campaign.

5.2.2 Data Quality of CH_4 Measurements

CH_4 concentration measurements come from LI-7700 methane gas analyser. Therefore, measured concentration of CH_4 are reliable. However, H_2O concentrations measured by LI-7500A instrument may introduce errors caused by condensation on the source lens. Therefore, large changes of H_2O concentrations (in terms of mole fraction) may introduce considerable impact on the mixing ratio of CH_4. H_2O concentrations before August 3rd (2017) are also compared with H_2O concentrations for the entire field campaign to assess if the H_2O measurements can impact the calculation of CH_4 flux.

5.3 Concentration Measurements

LI-7500A gas analyser measured both CO_2 concentrations, and H_2O concentrations during the field campaign. LI-7700 measured the concentrations of CH_4. All concentration measurements from LI-7500A and LI-7700 are in units of molar density, therefore, conversion from molar density to molar mixing ratio is necessary to make CO_2 concentration output independent of H_2O concentrations. EddyPro calculates CO_2 concentrations as molar mixing ratio in units of micromole (µmol) of CO_2 per mole (mol) of dry air. Conversion from µmol/mol to parts per million by volume (ppmv) (dry) does not change the magnitude of number, and therefore EddyPro also gives ppmv values through molar mixing ratio. Table 5.3 summarizes the minimum (Min), maximum (Max), median, and average concentrations of both CO_2, CH_4 and H_2O gases during the entire field campaign. As discussed in Section 5.2, measured CO_2

concentrations may not be reliable. Table 5.4 shows the minimum, maximum, median and average concentrations of CO_2, CH_4 and H_2O before August 3rd, 2017.

Table 5.3. Minimum, maximum, median, and average concentrations of CO_2, CH_4 and H_2O for the entire field campaign.

Statistics	CO_2 Concentrations (ppmv)	CH_4 Concentrations (ppmv)	H_2O Concentrations (mmol/mol)
Minimum	364.807	1.975	7.488
Maximum	449.276	13.668	22.441
Median	385.313	3.020	12.734
Average	388.840	3.577	13.215

Note: values shown obtained from 30 min time averaging output from EddyPro after data filtration.

Table 5.4. Minimum, maximum, median, and average concentrations of CO_2, CH_4 and H_2O before August 3rd, 2017.

Statistics	CO_2 Concentrations (ppmv)	CH_4 Concentrations (ppmv)	H_2O Concentrations (mmol/mol)
Minimum	387.483	2.078	8.188
Maximum	434.052	3.696	16.556
Median	392.732	2.652	13.722
Average	395.209	2.678	12.483

Note: values shown obtained from 30 min time averaging output from EddyPro after data filtration.

The median and average concentrations of CO_2 before the diagnostic problem (Table 5.4) are generally higher than the corresponding values after the diagnostic problem (Table 5.3). However, the range between minimum and maximum values of CO_2 concentrations before the diagnostic problem is smaller than the corresponding range after the diagnostic problem. On the other hand, the median and average concentrations of CH_4 before the diagnostic problem are generally lower than the corresponding values after the diagnostic problem, while the range between minimum and maximum values of CH_4 concentrations before the diagnostic problem is smaller than the corresponding range after the diagnostic problem. The range of concentrations

are expected statistically to be higher for a longer duration of measurements, which is consistent with the data shown in Table 5.3 and Table 5.4. However, average/median CO_2 concentrations are higher before the diagnostic problem while CH_4 concentrations are lower. This may be caused by consumption of CO_2 during CH_4 production from microbial metabolism (Stasik and Wendt-Potthoff, 2016), or caused by unreliable CO_2 concentration measurements after the failure of the CO_2 gas analyser. For comparison purpose, concentrations of H_2O are also presented in Table 5.3, and Table 5.4. Even though condensation problem of LI-7500A greatly affects the CO_2 concentration measurements and CO_2 flux output, H_2O concentrations remain relatively consistent after the diagnostic problem. Therefore, CH_4 flux output is still reliable after WPL correction, even after the condensation problem of LI-7500A.

5.3.1 CO_2 Concentrations

Figure 5.5 presents all valid measurements of CO_2 concentrations during the entire field campaign. The filtered concentration measurements are not continuous since wind direction filtration filters out majority of data. Figure 5.5-A shows the whole view of CO_2 concentrations, while Figure 5.5-B reveals the zoomed in CO_2 concentrations from day 245 (September 2) to day 254 (September 11) of 2017. Though concentration data is not continuous, Figure 5.5-B shows that peak CO_2 concentration measurements often occur during morning time (day 247, 249, 251, and 252 Figure 5.5-B). Pattern of peak CO_2 concentrations are consistent with previous EC measurements on water surface by Brown (2013). Red triangle in Figure 5.5-A encloses data points measured after the LI-7500A diagnostic problem.

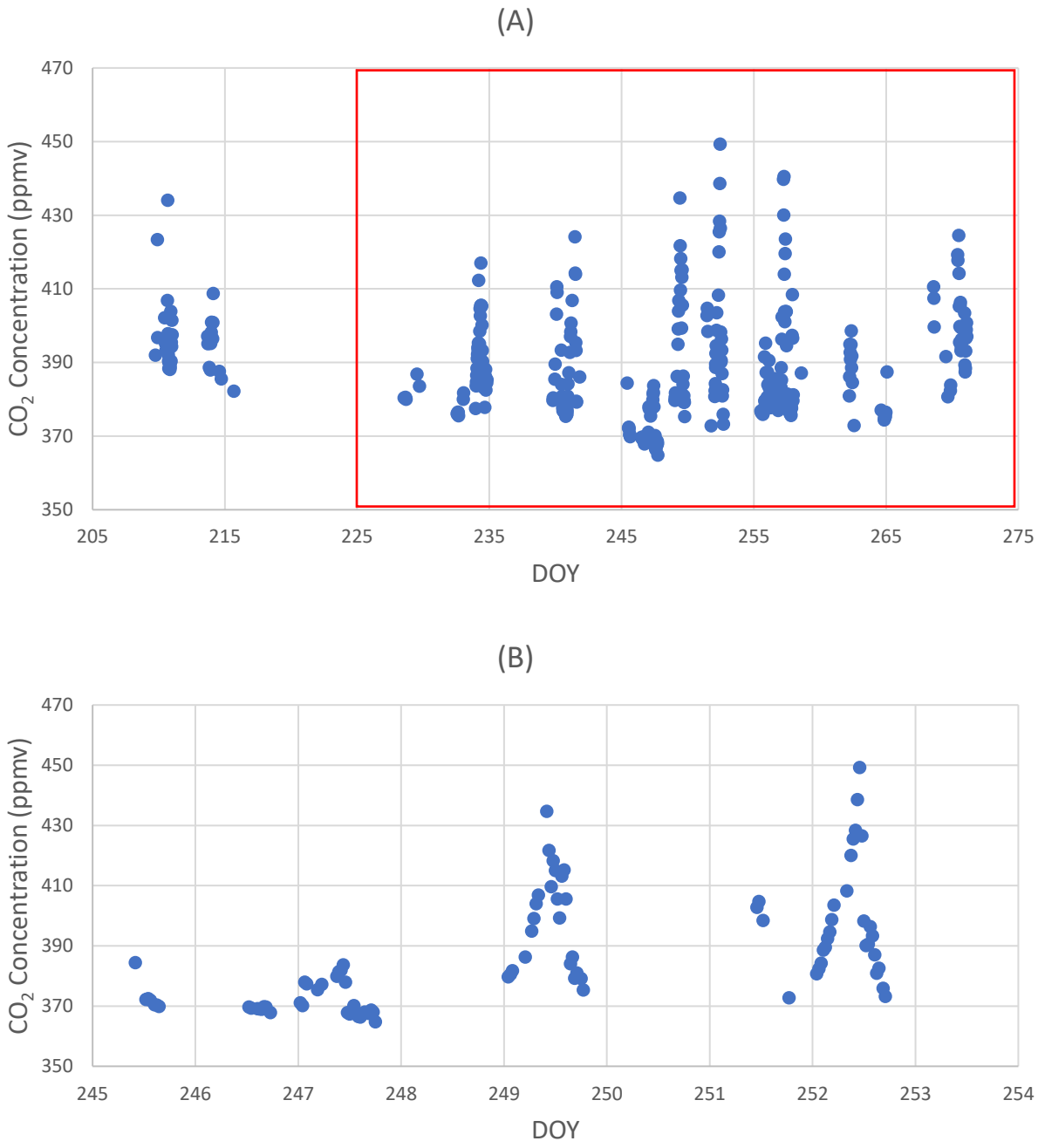

Figure 5.5. Filtered CO_2 concentrations plotted against DOY; (A): full scale; (B): zoom in.

5.3.2 CH_4 Concentrations

Figure 5.6 presents all valid measurements of CH_4 concentrations during the whole field campaign. Figure 5.6-A presents the whole view of CH_4 concentrations, while Figure 5.6-B

shows the zoomed in CH_4 concentrations from day 245 (September 2) to day 254 (September 11) of 2017. Though CH_4 concentrations are not continuous, Figure 5.6-B shows that peak CH_4 concentration measurements often occur shortly after midnight (beginning of day 247, 249, and 252 in Figure 5.6-B). Concentrations of CH_4 are higher during night due to reduced atmospheric mixing at nighttime, which is consistent with Mahzabin (2012) experiments.

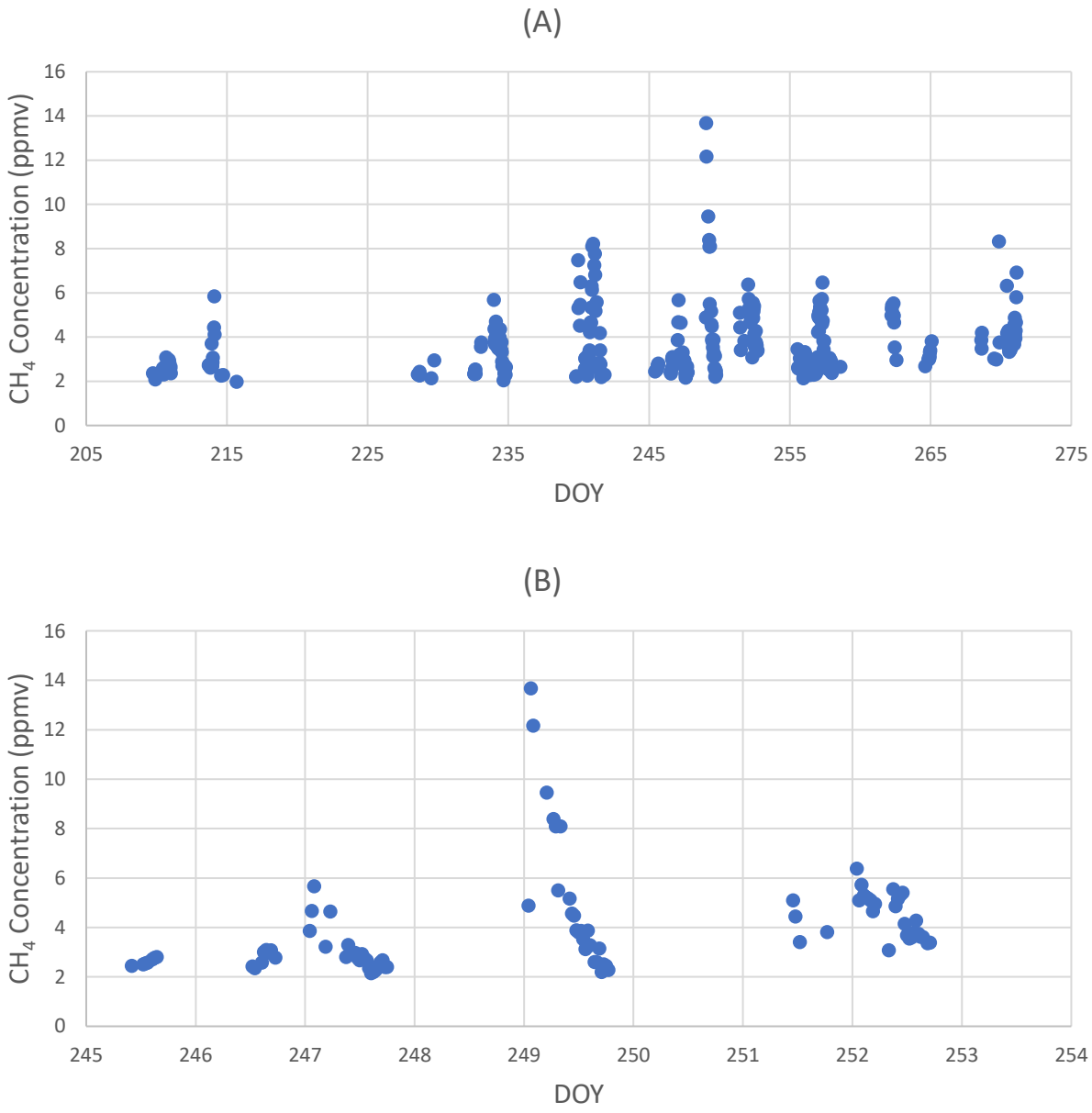

Figure 5.6. Filtered CH_4 concentrations plotted against DOY; (A): full scale; (B): zoom in.

5.3.3 Concentration Roses

Figure 5.7 shows the concentration roses of CO_2. The wind mainly blows from north and northwest of the pond toward the EC tower. In Figure 5.7, high concentrations of CO_2 come from both west and east of the target tailings pond.

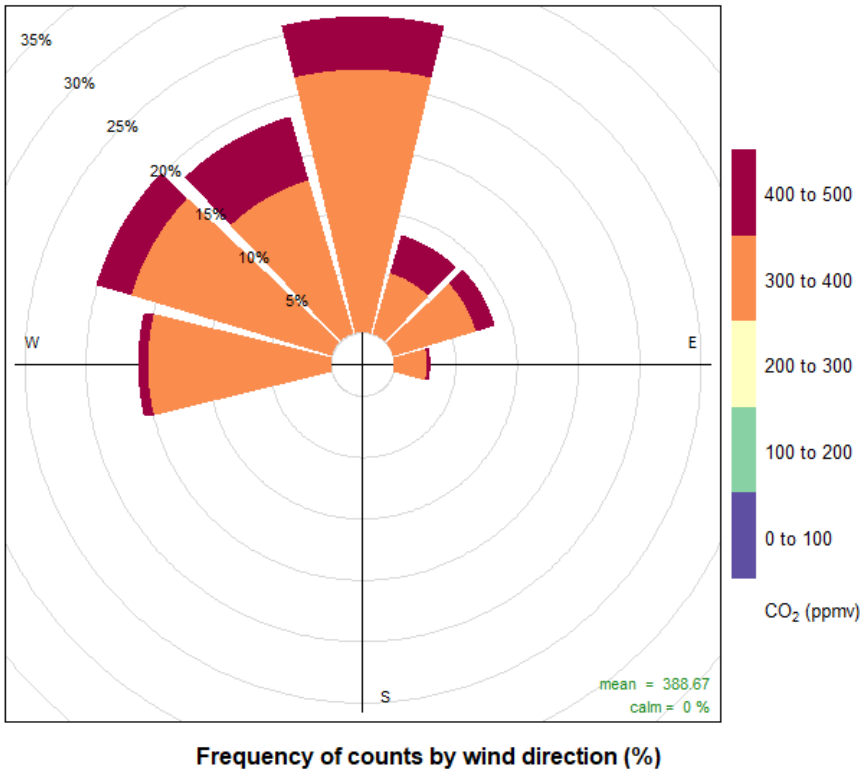

Figure 5.7. CO_2 Concentration Rose (filtered data); Colour of the wedges indicates concentrations of CO_2 in ppmv.

Similarly, Figure 5.8 shows the concentration roses of CH_4. In Figure 5.8, the wind direction frequency of CH_4 is the same as in Figure 5.7. More CH_4 concentrations come from west of the target pond than east of the pond.

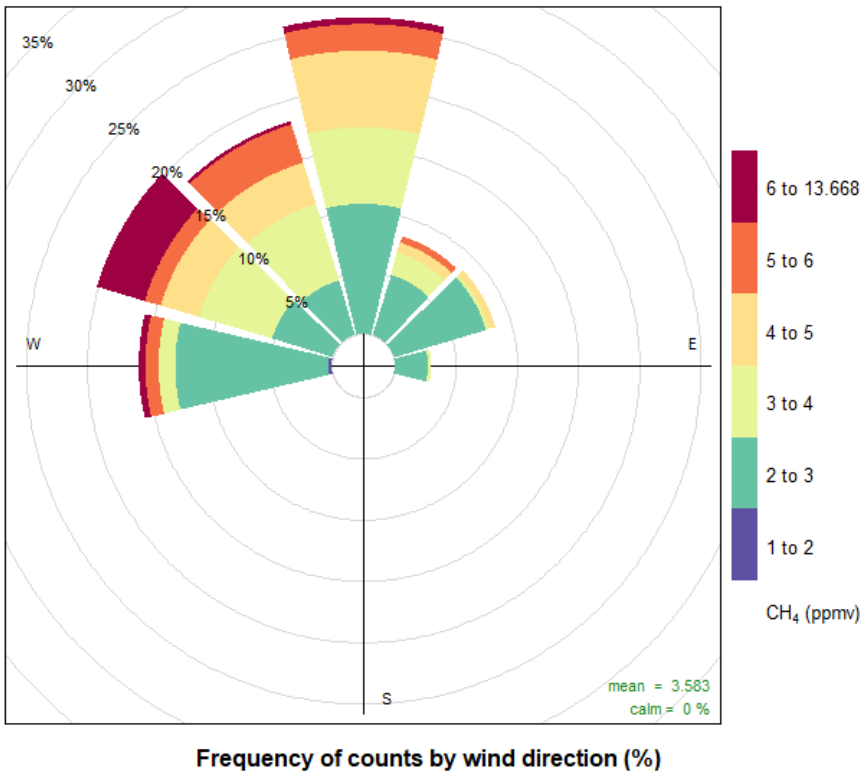

Figure 5.8. CH_4 Concentration Rose (filtered data); Colour of the wedges indicates concentrations of CH_4 in ppmv.

5.4 Flux Outputs

EddyPro advanced setting calculated and corrected filtered fluxes of both CO_2 and CH_4. Table 5.5 shows the minimum, maximum, median, and average values of both CO_2 and CH_4 fluxes in units of gram (g) per square metre (m^2) per day (d), and µmol per second per metre square (m^2). The minus sign means the flux is negative (pond is a sink instead of a source). Please note the calculated CO_2 fluxes may not be accurate as discussed in Section 5.1. Table 5.6 shows the measurements of CO_2 and CH_4 flux before August 3rd, 2017 (when the LI-7500A diagnostic problem occurred). The flux values of CO_2 fluxes before August 3rd are obviously higher than

the CO_2 flux values of the entire field campaign, therefore, the CO_2 flux measurements after the diagnostic problem has markedly drifted and may be less reliable than the measurements obtained before August 3rd, 2017.

Table 5.5. Minimum, maximum, median and average fluxes of CH_4 and CO_2 for entire field campaign.

Statistics	CO_2 Flux ($\mu mol/s/m^2$)	CO_2 Flux ($g/m^2/d$)	CH_4 Flux ($\mu mol/s/m^2$)	CH_4 Flux ($g/m^2/d$)
Minimum	-31.346	-119.165	-1.562	-2.159
Maximum	26.490	100.704	15.791	21.829
Median	1.798	6.835	4.680	6.470
Average	0.869	3.304	4.743	6.557

Table 5.6. Minimum, maximum, median and average fluxes of CH_4 and CO_2 before August 3rd, 2017.

Statistics	CO_2 Flux ($\mu mol/s/m^2$)	CO_2 Flux ($g/m^2/d$)	CH_4 Flux ($\mu mol/s/m^2$)	CH_4 Flux ($g/m^2/d$)
Minimum	-27.633	-105.050	0.222	0.307
Maximum	26.489	100.701	7.817	10.806
Median	2.92	11.101	4.692	6.486
Average	3.036	11.542	4.28	5.917

5.4.1 CO_2 Flux

Figure 5.9 shows all valid CO_2 flux measurements throughout the field campaign, after all post measurement data procedures, including the instrument sensible heat (ISH) correction. Since fluxes calculation requires concentration data, wind direction filtration does introduce large gaps in data (Figure 5.9 A closer look at the flux data (Figure 5.9-B) reveals no clear pattern of CO_2 flux variation. The maximum CO_2 flux measurement occurred during the first few days of field campaign, while majority of CO_2 flux measurements occurred later during the field campaign. The CO_2 fluxes are lower than previously reported values for the target tailings pond, obtained with flux chamber (Small et al., 2015). As presented in Table 5.5, the median CO_2 fluxes

measured during the field campaign is around 6.835 g/m2/d, which is lower than 16.35 CO_2 emission measured in 2012 (Small et al., 2015). The average CO_2 flux in Table 5.5 at 3.304 is even lower. The main contributor to this large difference is considerable numbers of negative CO_2 fluxes output obtained in this field campaign. As shown in Table 5.6, flux measurements (median and average values) of CO_2 before August 3rd, 2017 are much closer to previous CO_2 flux measurements (Small et al., 2015). Further discussion in Section 6.3 will address possible reasons causing negative CO_2 flux outputs. Red rectangle in Figure 5.9-A encloses data points measured after the LI-7500A condensation problem.

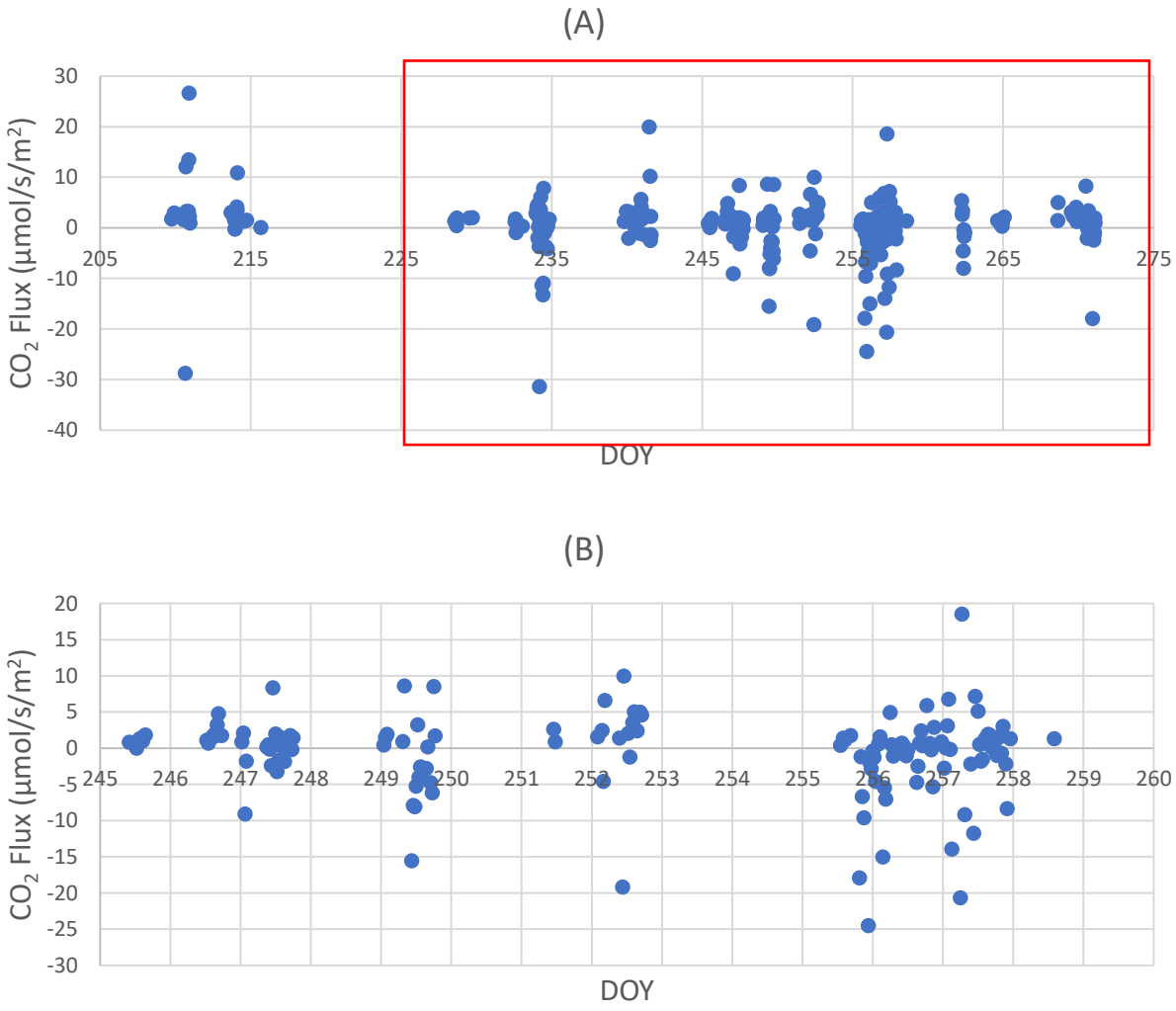

Figure 5.9. Filtered CO_2 fluxes plotted against DOY; (A): full scale; (B): zoom in.

5.4.2 CH_4 Flux

Figure 5.10 shows the filtered CH_4 fluxes during the field campaign. As shown in Table 5.5 and Table 5.6, CH_4 flux values did not markedly change after the LI-7500A diagnostic issues, therefore, all CH_4 flux outputs after data quality filtration are reliable. Wind direction filtration also introduces data gaps in Figure 5.10. Almost all CH_4 fluxes are above zero, indicating the target tailings pond as fugitive CH_4 source. Figure 5.10-B indicates no clear pattern of CH_4 flux variation. As presented in Table 5.5, the median CH_4 fluxes during the field campaign is around 6.470 , which is higher than previous value of 2.59 obtained with a flux chamber (Small et al., 2015). Median CH_4 flux is also higher than CO_2 flux during this EC field campaign. In past studies, CH_4 fluxes are notably smaller than CO_2 emission (Small et al., 2015). Section 6.3 of this thesis discusses possible reasons for the difference between the EC measurements and previous measurements.

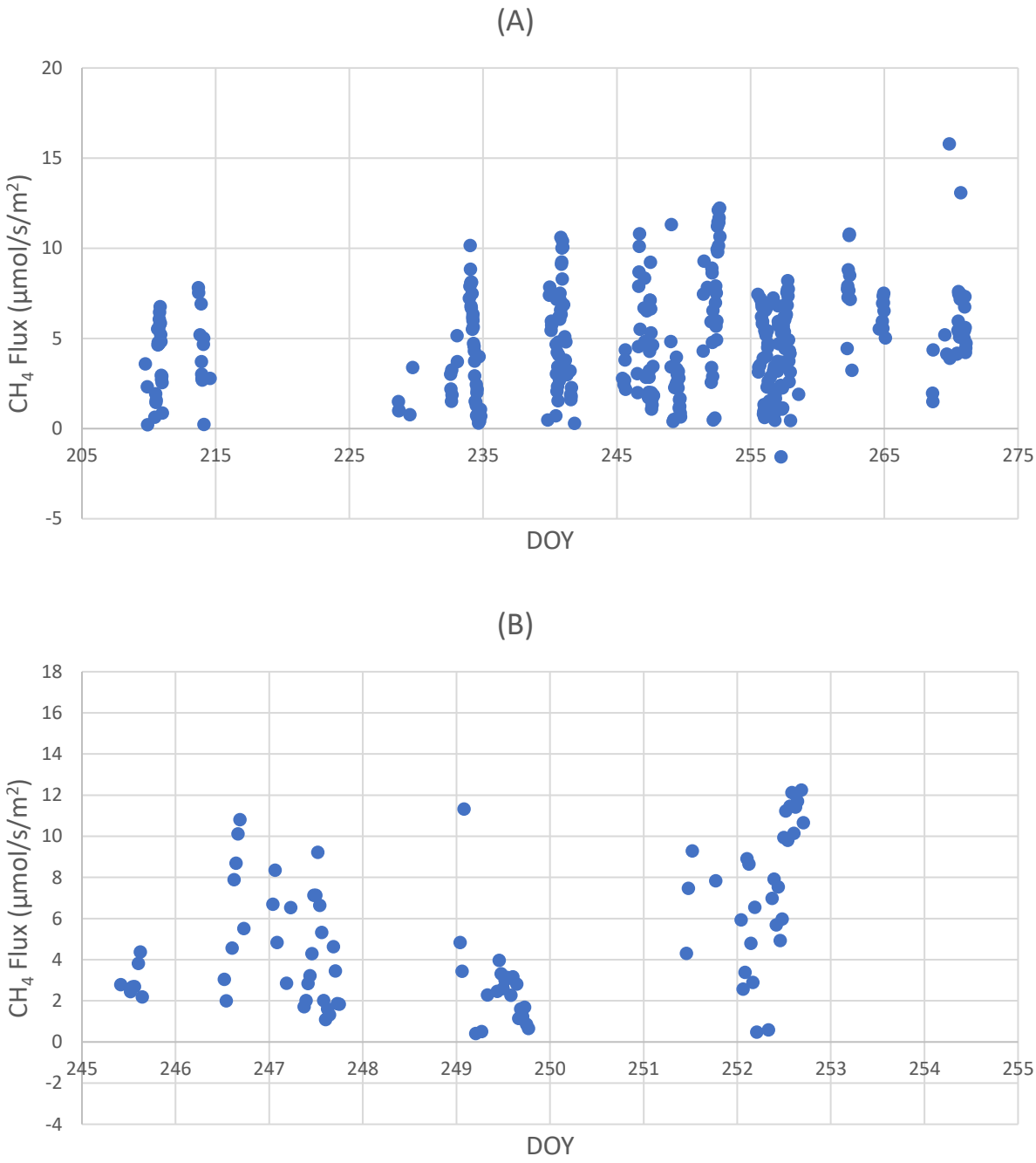

Figure 5.10. Filtered CO_2 fluxes plotted against DOY; (A): full scale; (B): zoom in.

5.5 CO_2 Flux Outputs without ISH Correction

The ISH correction is not typically applicable for measurements under relatively warm weather (around 15 °C), since, for measurements under warm temperature, it may only cause small noise without much effect on the output flux (Burba et al., 2008). However, for general small fluxes over water surfaces, the instrument sensible heat flux may not be negligible and may markedly impact the flux output. The ISH correction is based on a linear regression between the air temperature and the instrument surface temperature, and therefore may be field specific. Therefore, presenting flux outputs without the ISH correction is necessary for more comprehensive understanding of the flux output. Table 5.7 shows the minimum, maximum, median, and average CO_2 flux value without the "add ISH components" correction.

Table 5.7. Minimum, maximum, median and average fluxes of CO_2 without ISH correction.

Statistics	CO_2 Flux ($\mu mol/s/m^2$)	CO_2 Flux ($g/m^2/d$)
Minimum	-31.401	-119.374
Maximum	26.606	101.145
Median	1.13	4.296
Average	0.25	0.950

Comparing CO_2 flux outputs in Table 5.7 (without ISH correction) to the CO_2 flux outputs in Table 5.5 or Table 5.6 (with ISH correction), the median and average CO_2 flux outputs in Table 5.7 are relatively smaller. This means the ISH correction in EddyPro does affect the values of CO_2 flux output during this field campaign. However, the linear correction done in EddyPro was based on empirical specific field condition (Burba et al., 2008), and was not optimized for this specific case. Therefore, the calculated CO_2 flux either before or after the correction may not be able to represent the exact true CO_2 flux of this field campaign.

Figure 5.11 presents all the flux outputs from EddyPro without the ISH correction. CO_2 flux outputs in Figure 5.11 show similar trends as in Figure 5.9. However, each flux outputs did not go through the ISH correction, and majority of flux outputs are slightly smaller than flux outputs with ISH correction.

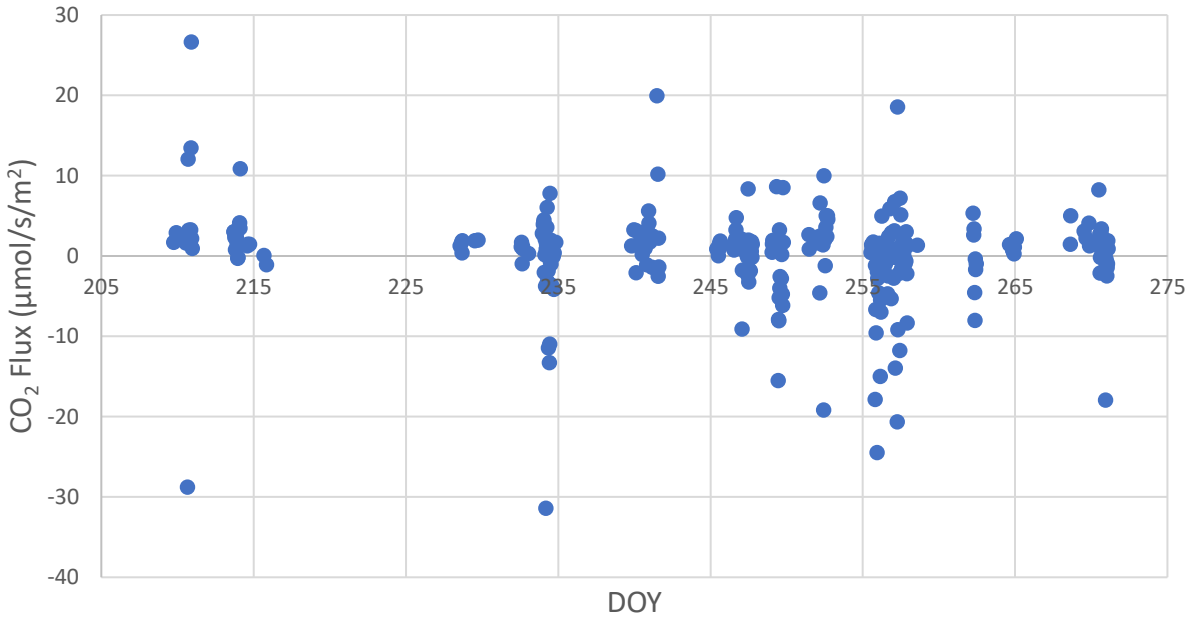

Figure 5.11. Filtered CO_2 fluxes without ISH correction plotted against DOY.

6.0 DISCUSSIONS

6.1 Data Interpretation

6.1.1 Concentrations and Temperature

Figure 6.1 depicts all filtered CO_2 concentrations data against the air temperature measured by CSAT3 sonic anemometer. The relationship between CO_2 concentrations and temperature is not obvious. Peak CO_2 concentration measurements occurred around 288 K.

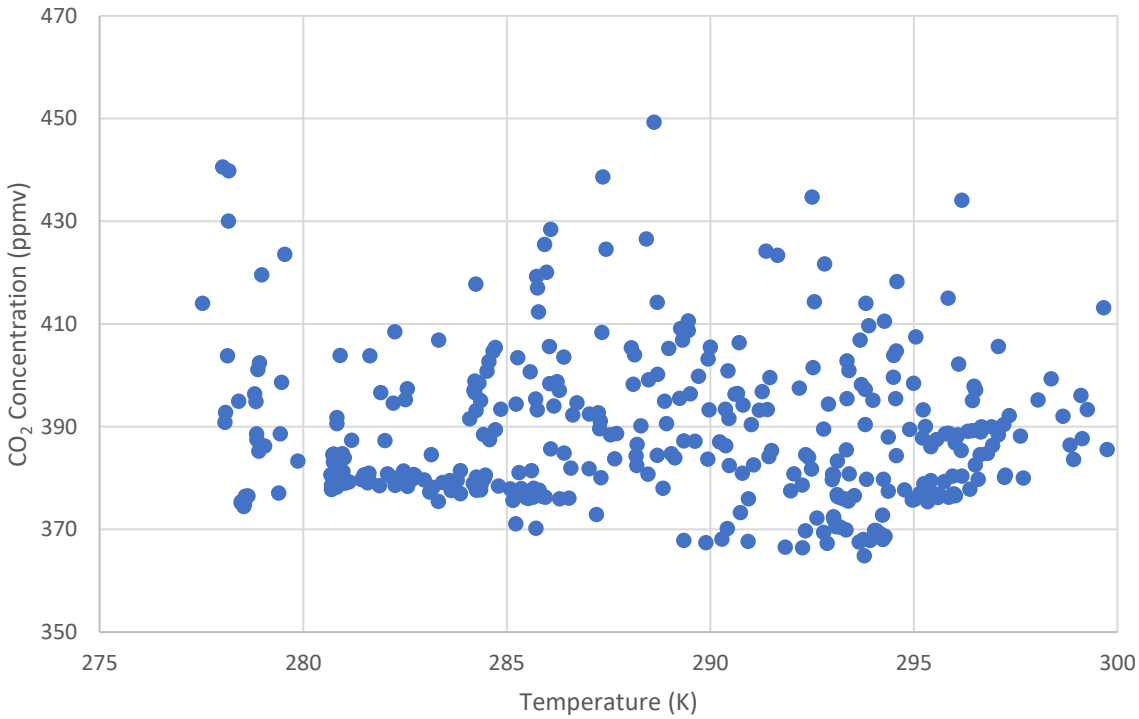

Figure 6.1. CO_2 concentrations in relation to temperature.

Figure 6.2 shows the relationship between CH_4 concentrations and temperature. No clear pattern of CH_4 concentrations variation related to temperature can be observed. CH_4 concentrations are notably lower than average (shown in Table 5.3) at temperatures above 294 K, and peak CH_4 concentrations appear at around 288 K to 293 K.

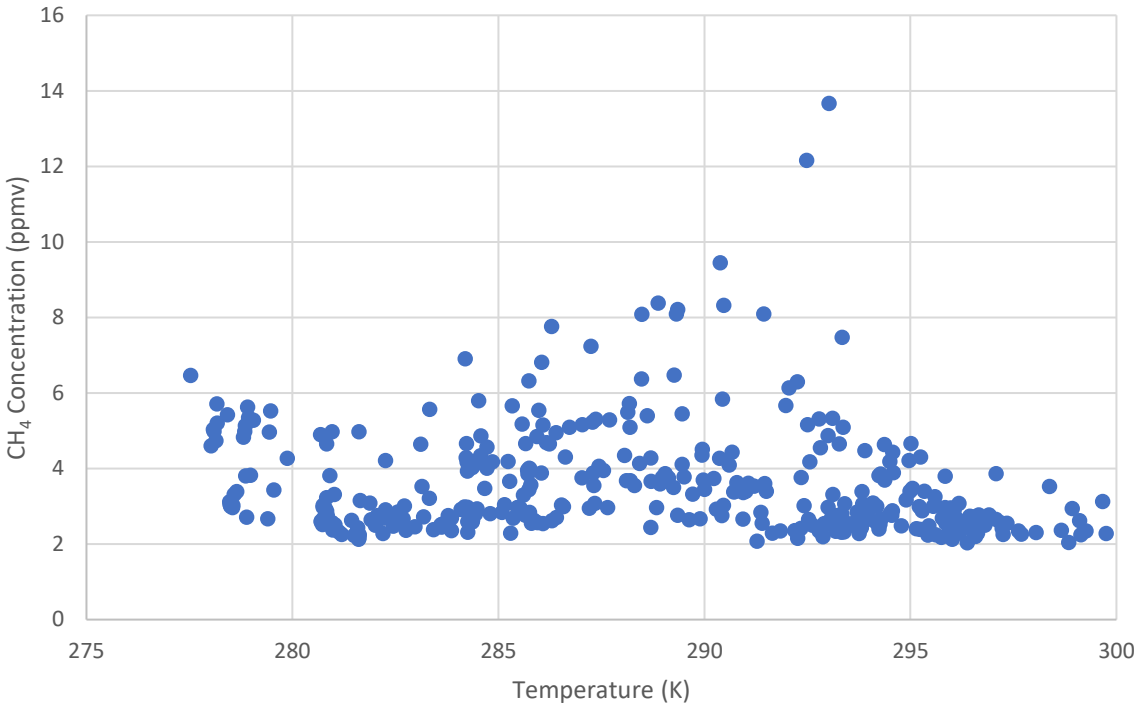

Figure 6.2. CH_4 concentrations in relation to temperature.

6.1.2 Concentrations and Wind Speed

Figure 6.3 presents the relationship between CO_2 concentrations and mean horizontal wind speed (ū) while Figure 6.4 shows the variation of CH_4 concentrations against wind speed. The highest concentrations of CO_2 and CH_4 were observed at low wind speed (0.0 m/s to 2.0 m/s). At high wind speed (6.0 m/s to 8.5 m/s), concentrations of CO_2 and CH_4 were generally low, but this observation was also based on a small number of data points. Concentrations of atmospheric GHGs are lower in strong wind condition due to more concentration dilution caused by the wind. Gas concentrations in the atmosphere usually decreases as wind speed increases (Jones et al., 2010).

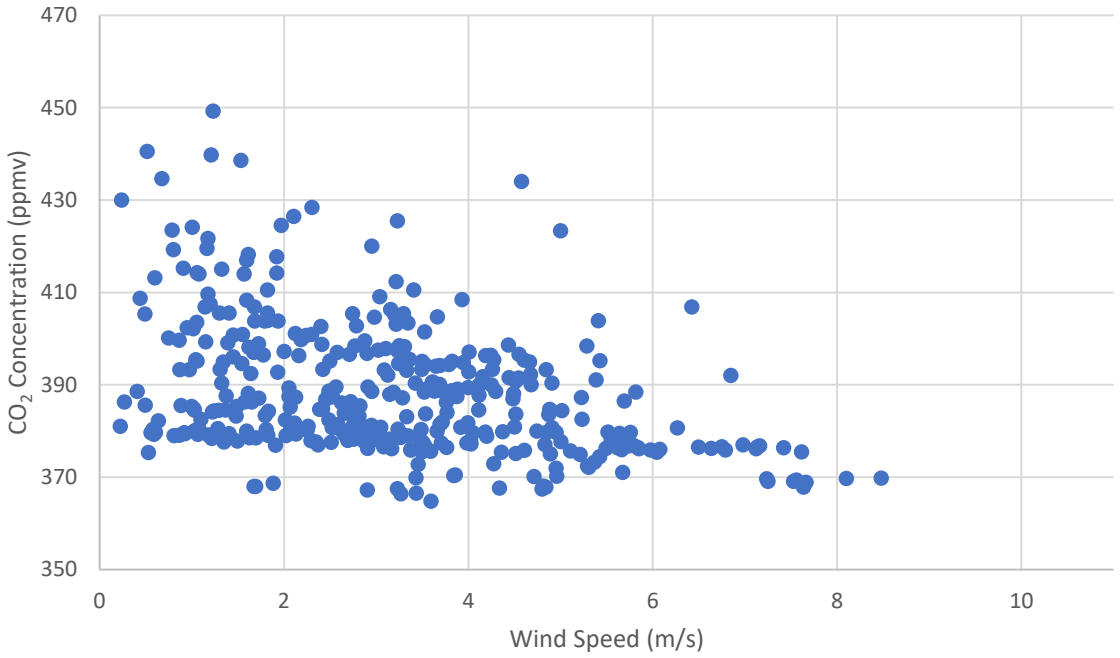

Figure 6.3. CO_2 Concentrations in relation to mean horizontal wind speed (ū).

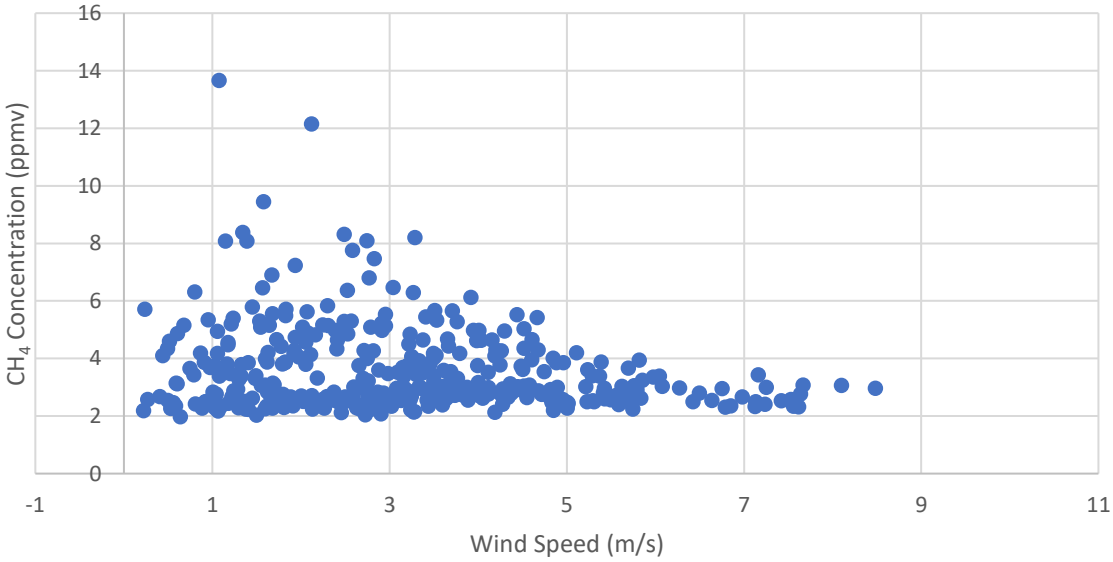

Figure 6.4. CH_4 Concentrations in relation to mean horizontal wind speed (ū).

6.1.3 Fluxes and Temperature

Figure 6.5 shows CO_2 fluxes variation with temperature. The mean CO_2 remained relatively stable as temperature varies. Section 6.1.8 will still discuss the relationship between diurnal averaged variation of CO_2 fluxes and diurnal temperature more closely. Unfortunately, the CO_2 flux values after the LI-7500A diagnostic problem are generally less reliable. Air temperature variation should not have a main impact on flux measurements as temperature does not impact the instantaneous change of vertical wind speed and the instantaneous change of the trace gas concentration.

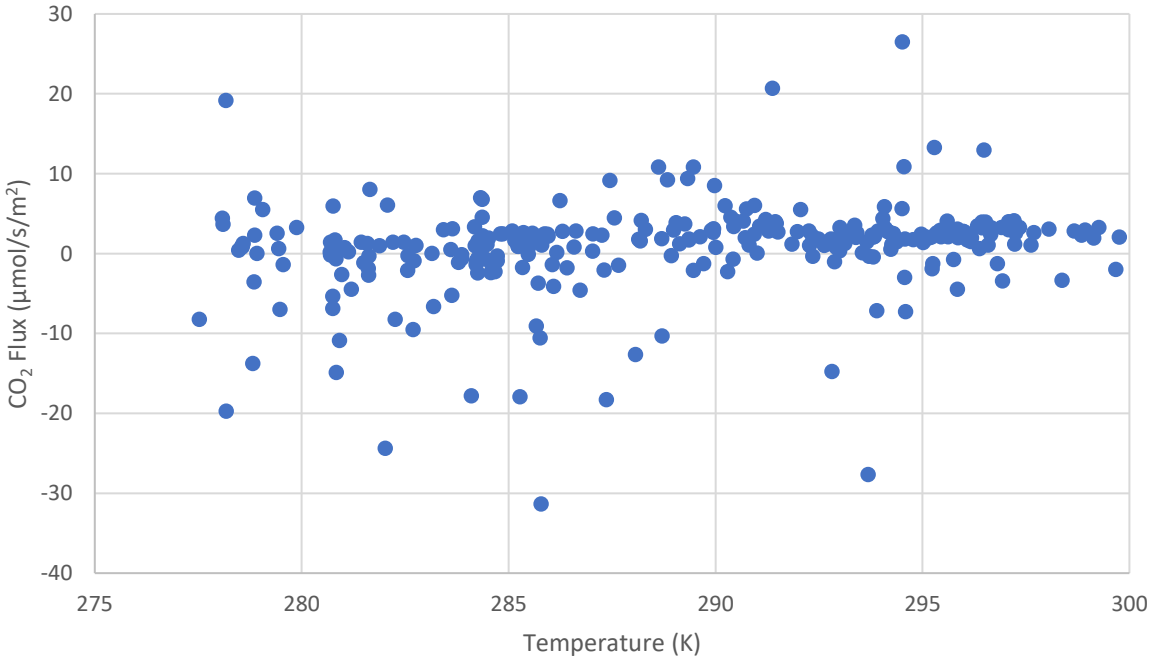

Figure 6.5. CO_2 fluxes in relation to temperature.

Figure 6.6 presents the variation of CH_4 fluxes with temperature. No obvious relationship between CH_4 and temperature is observed. The highest CH_4 flux appears at around 291 K (around 17.85 °C), which is close to the temperature of highest CH_4 concentrations. Air

temperature does not impact generation of GHGs from the tailings pond as microbial activities occur underneath the tailings pond water surface.

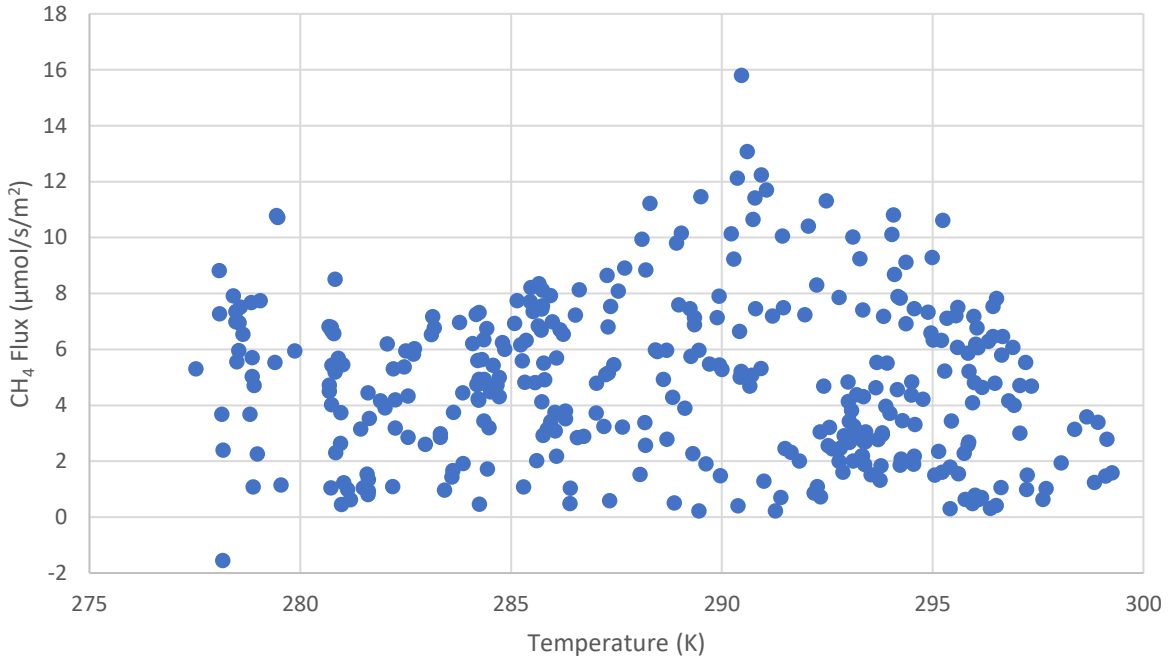

Figure 6.6. CH_4 fluxes in relation to temperature.

6.1.4 Fluxes and Wind Speed

Wind (eddies) can carry the emissions from the tailings pond surface to the EC tower. A high enough wind speed which can produce enough turbulence is key for observing correct flux emissions from the target water surface (Burba, 2013). Figure 6.7 presents variation of CO_2 fluxes against mean horizontal wind speed. There is no clear relationship between CO_2 fluxes and horizontal wind speed (Figure 6.7). As wind speed increases above 6 m/s, the range of CO_2 fluxes narrows down, and the number of negative CO_2 fluxes decreases due to possible contribution of CO_2 sources outside of the pond at high wind speed.

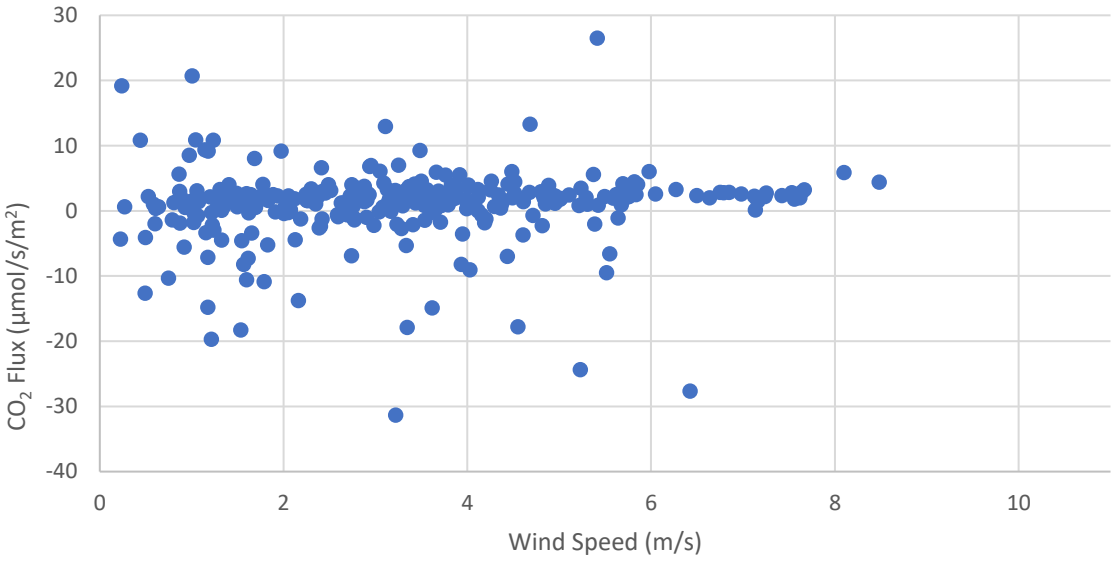

Figure 6.7. CO_2 fluxes in relation to mean horizontal wind speed (ū).

Figure 6.8 depicts the variation of CH_4 fluxes with respect to mean horizontal wind speed. There is no clear correlation between CH_4 fluxes and the wind speed (Figure 6.8). In contrast with the relationship between CO_2 fluxes and wind speed, range and maximum value of CH_4 fluxes increase as wind speed increases. Higher wind speed (> 1 m/s) fully develops the turbulence of water surface, therefore, it drives up the measurements of CH_4 fluxes (Burba, 2013). Once the turbulence is fully developed at moderate or high wind speed, the CH_4 fluxes start to remain relatively consistent.

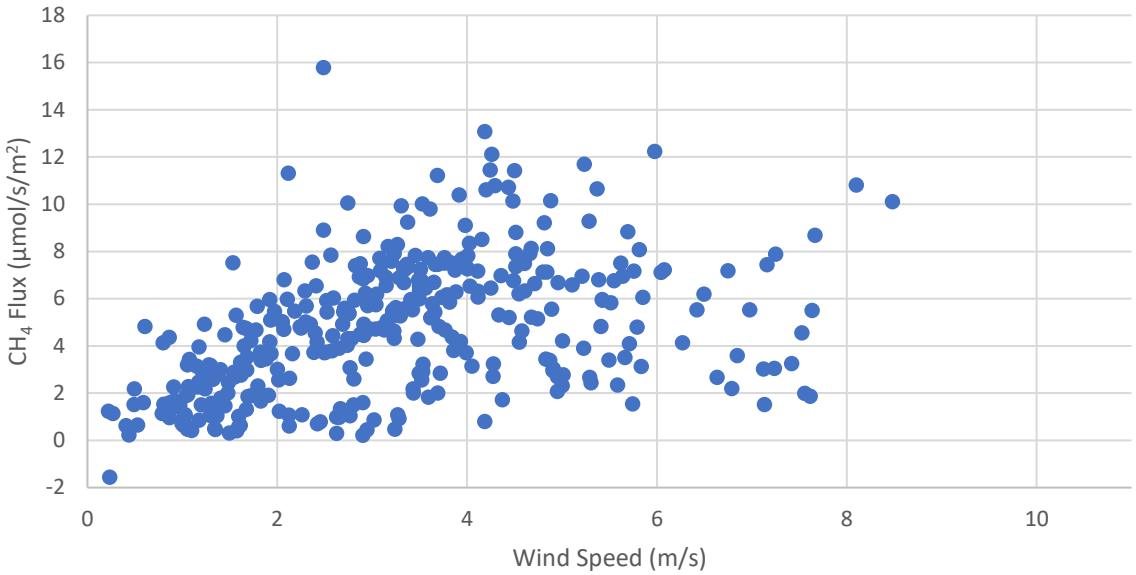

Figure 6.8. CH_4 fluxes in relation to mean horizontal wind speed (ū).

6.1.5 Emission Fluxes and Wind Direction

Figure 6.9 gives the wind direction distribution of CO_2 flux measurements. All CO_2 fluxes presented in Figure 6.9 are filtered only based on EddyPro error flags and Mauder and Foken (2004, explained in Mauder and Foken, 2013) flux flags (discussed in Section 5.1). The red rectangle enclosed discarded CO_2 flux data from wind direction 90 ° to 270° related to the direction of sonic anemometer (refer to Appendix A, North Offset Calculations for reasons behind wind direction filtration). These CO_2 fluxes come from south of the EC tower, and therefore do not represent CO_2 emissions from the target tailings pond.

In Figure 6.9, data points follow different data filtration process as stated in Section 5.1. Figure 6.9 discards CO_2 data with invalid time averaging period, diagnostic number, and Mauder and Foken (2004) flags, and excludes wind direction filtration. South wind was the dominant type of wind direction, and CO_2 fluxes from south are mainly positive. While relatively more negative

CO_2 fluxes came from the pond. This difference may be due to other strong CO_2 sources south to the pond.

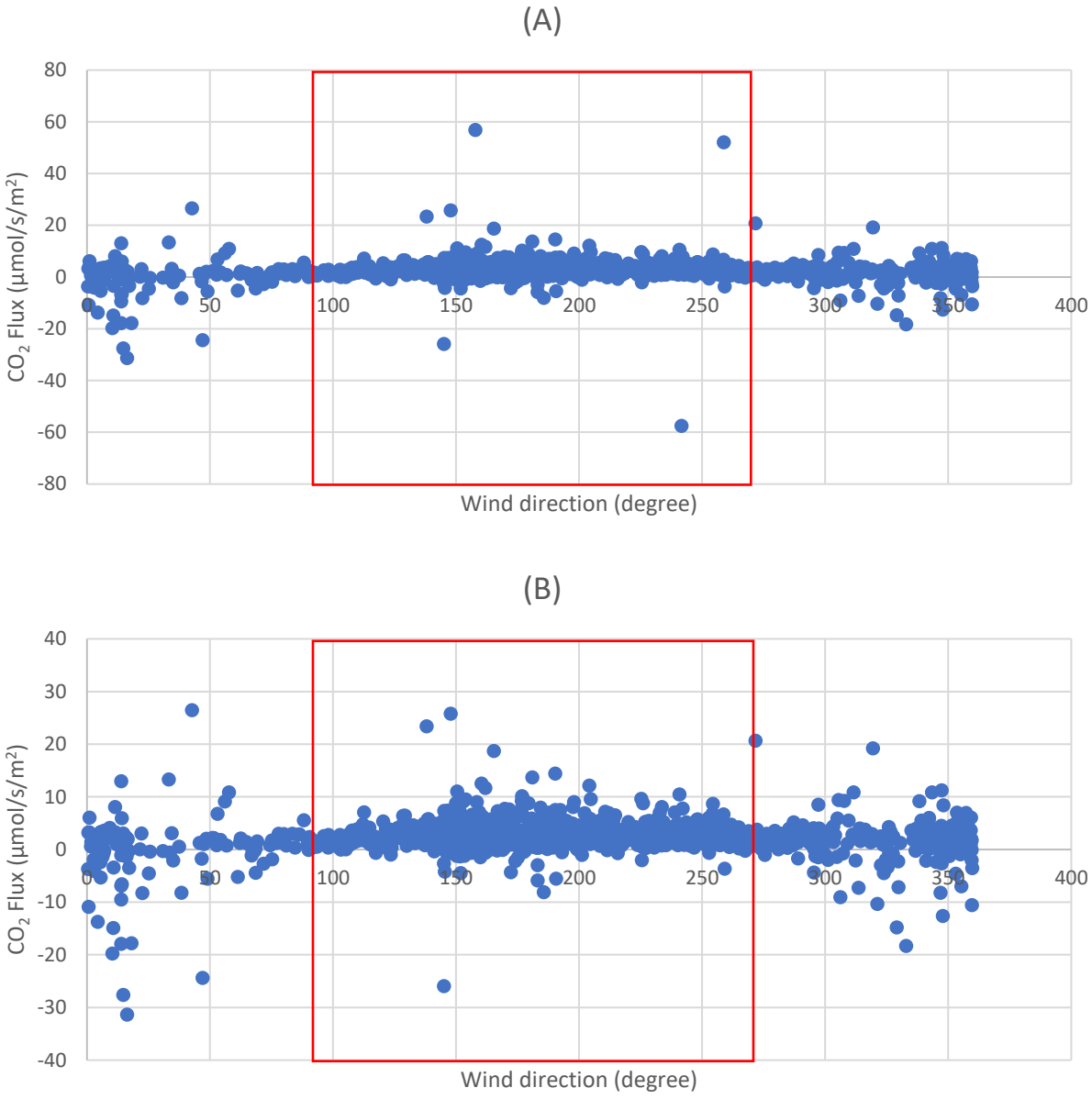

Figure 6.9. CO_2 fluxes in relation to wind direction (not filtered by wind direction); (A): full scale; (B): zoom in; red rectangle: south wind.

Figure 6.10 presents the relationship between CH_4 fluxes and wind direction. CH_4 fluxes from the target tailings pond are much higher than discarded CH_4 fluxes enclosed by the red rectangle.

This large difference indicates that the target tailings pond is a large source of CH_4 compared to the area south of the target tailings pond.

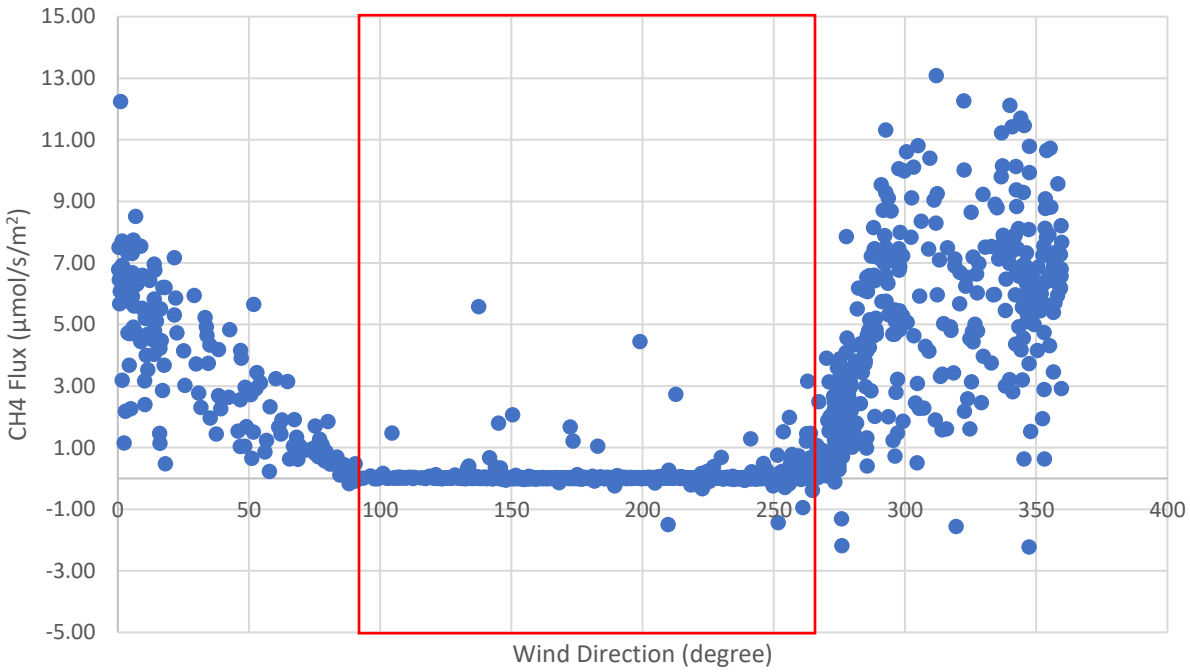

Figure 6.10. CH_4 fluxes in relation to wind direction (not filtered by wind direction); red rectangle: south wind.

6.1.6 Footprint Analyses

EddyPro calculates the 90% flux footprint, L_{90}, as the along-wind distance providing 90 percent contribution to turbulent fluxes. The 90% flux footprint calculation process selected in EddyPro Advanced Setting is a crosswind integrated model referring to Kormann and Meixner (2001). The data filtration of L_{90} value is based on wind direction and discards all error values (flagged by EddyPro as "-9999"). The number of error output of L_{90} is different from both CO_2 and CH_4 error output. The fluxes with L_{90} values larger than 1500 m were not discarded for comparison in Figure 6.11 and Figure 6.12.

Figure 6.11 shows more variability in CO_2 fluxes (in both positive and negative direction) for L_{90} values less than approximately 1300 m. The variability in CO_2 fluxes starts to drop after L_{90} go above 1300 m. As shown in Figure 4.1, the distance between the physical boundary of the water surface of the target tailings pond and the EC tower vary from 969 m to 1410 m. L_{90} at around 1300 m indicates a reasonable value for a relatively sharper change of the range of CO_2 fluxes. As L_{90} goes beyond 1300 m, other more stable sources of CO_2 outside of tailings pond boundary may contribute to the measured CO_2 fluxes.

Similarly, Figure 6.12 shows the variation of CH_4 fluxes with 90% flux footprint. Peak of CH_4 fluxes increases gradually as L_{90} values increase up to 1300 m then levels off. Beyond L_{90} of 2100 m, peaks of CH_4 fluxes drop markedly since the target tailings pond has much higher contribution to CH_4 fluxes than nearby sources.

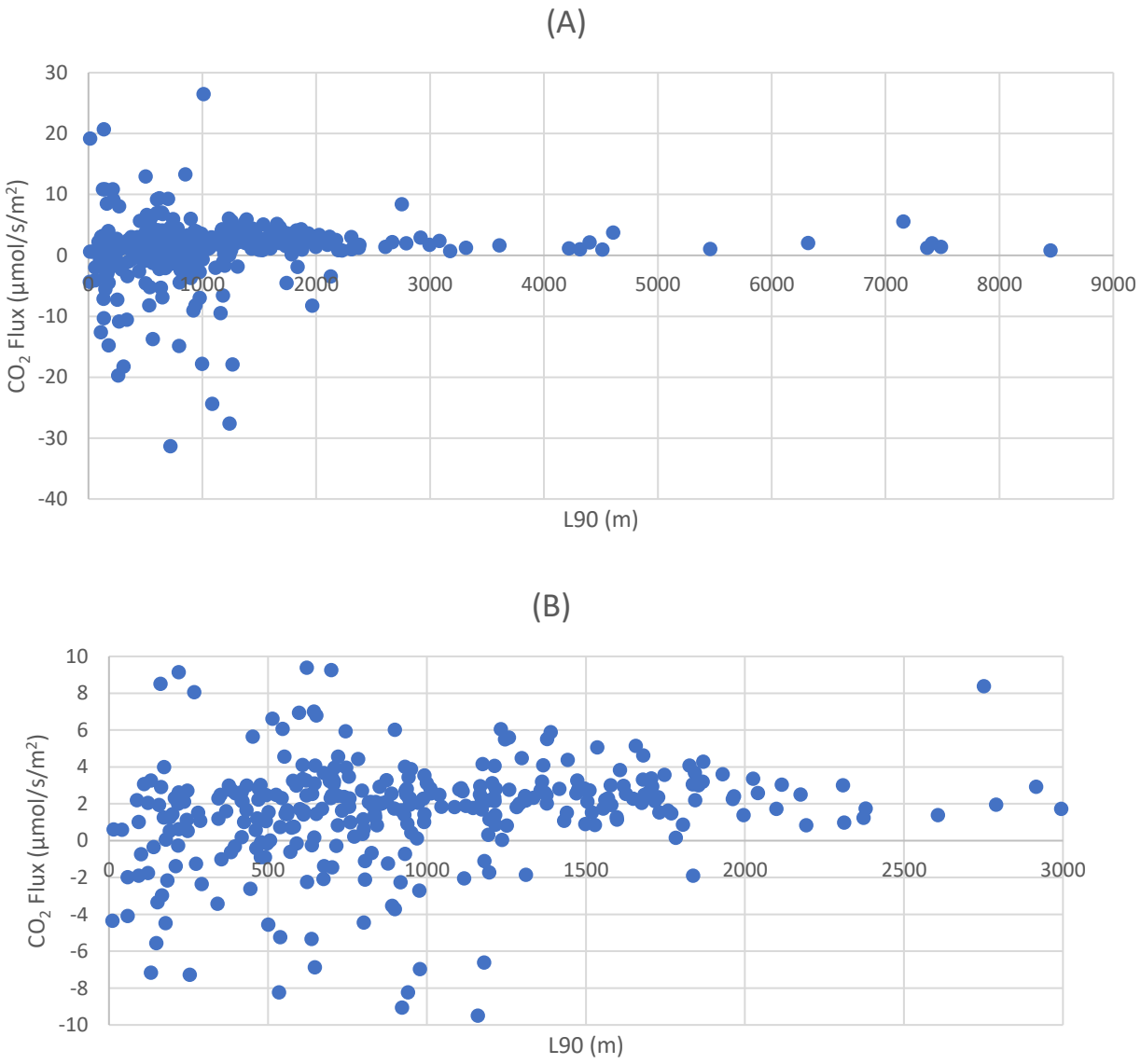

Figure 6.11. CO_2 fluxes in relation to L_{90} footprint; (A): full scale; (B): zoom in.

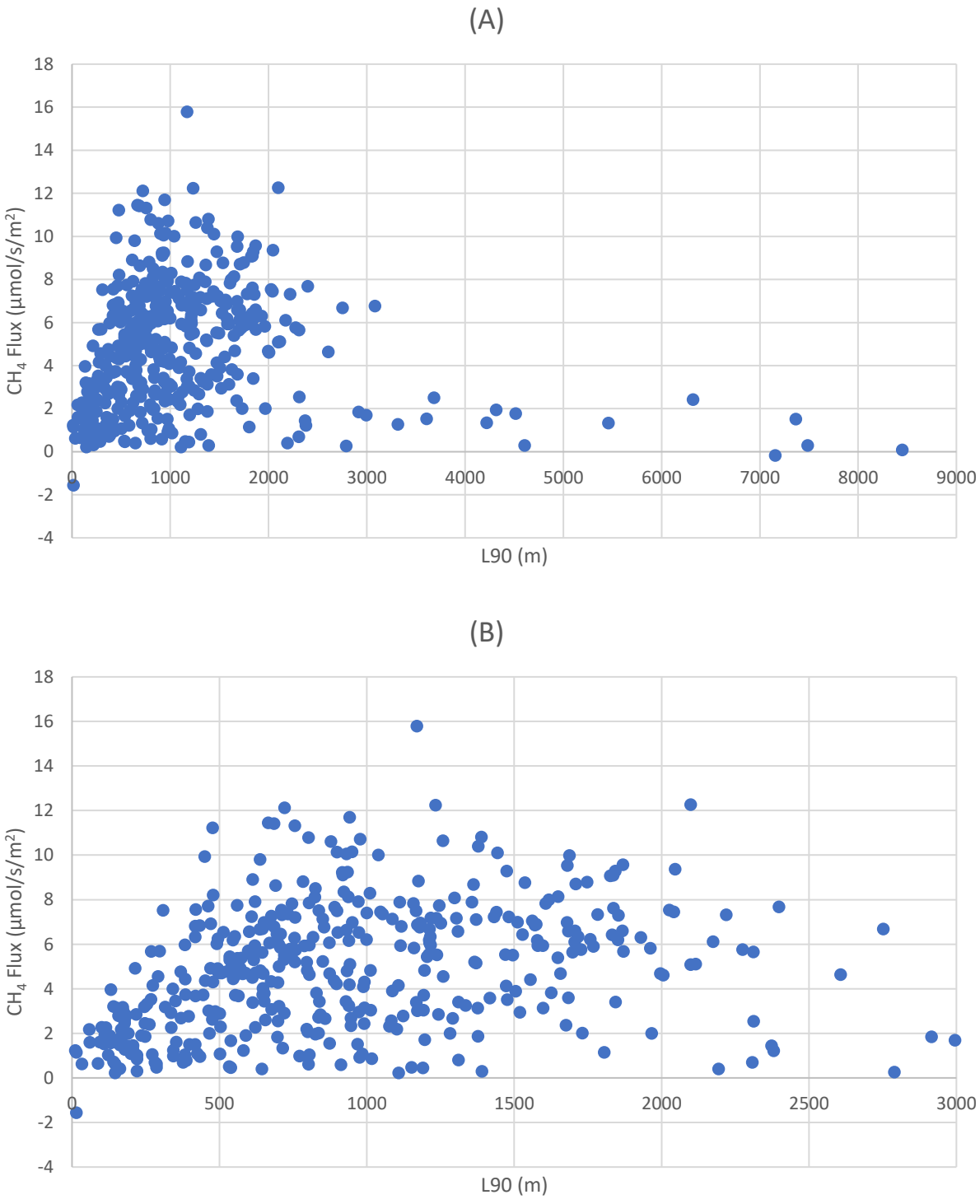

Figure 6.12. CH_4 fluxes in relation to L_{90} footprint; (A): full scale; (B): zoom in.

Figure 6.13 shows the variation of L_{90} value with respect to mean horizontal wind velocity ($\bar{u}$). L_{90} values increase as $\bar{u}$ increases. As wind speed increases, sources contributing to the measured fluxes may come from further distances towards the EC tower. Since Kormann and Meixner (2001) model accounts for advection and diffusion of the target atmospheric constituent, sometimes L_{90} may be large at relatively lower wind speed due to diffusion as dominant fate of constituent, especially during stable atmospheric condition at night (Burba, 2013).

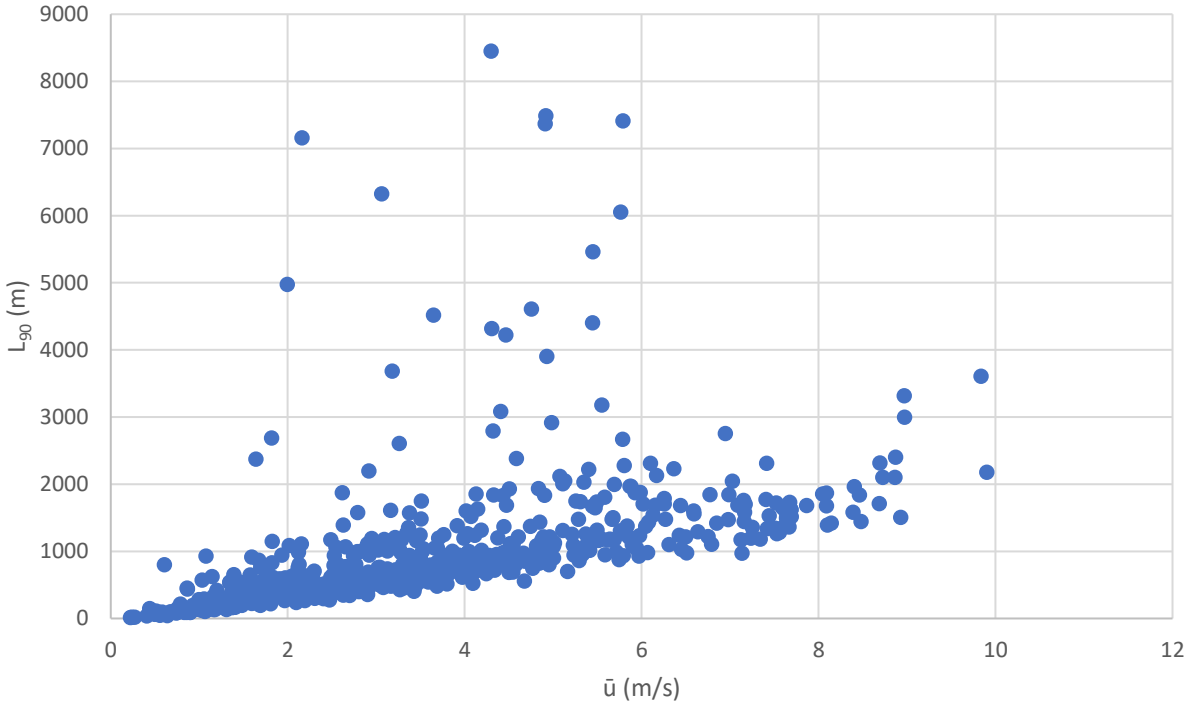

Figure 6.13. L_{90} values in relation to mean horizontal wind speed ($\bar{u}$).

Figure 6.14 reveals the relationship between L_{90} (without quality filtration for representative flux values) and wind direction. Mean L_{90} value is 962.61 m, and median L_{90} value is around 722 m. Both average and median L_{90} values are inside and close to the boundary of the target tailings pond. However, a portion of data (shown as orange and red in Figure 6.14) represents 90% flux

footprint beyond 1500 m, which highlights the importance of proper data filtration, based on footprint, to exclude GHG sources outside of the target pond boundary.

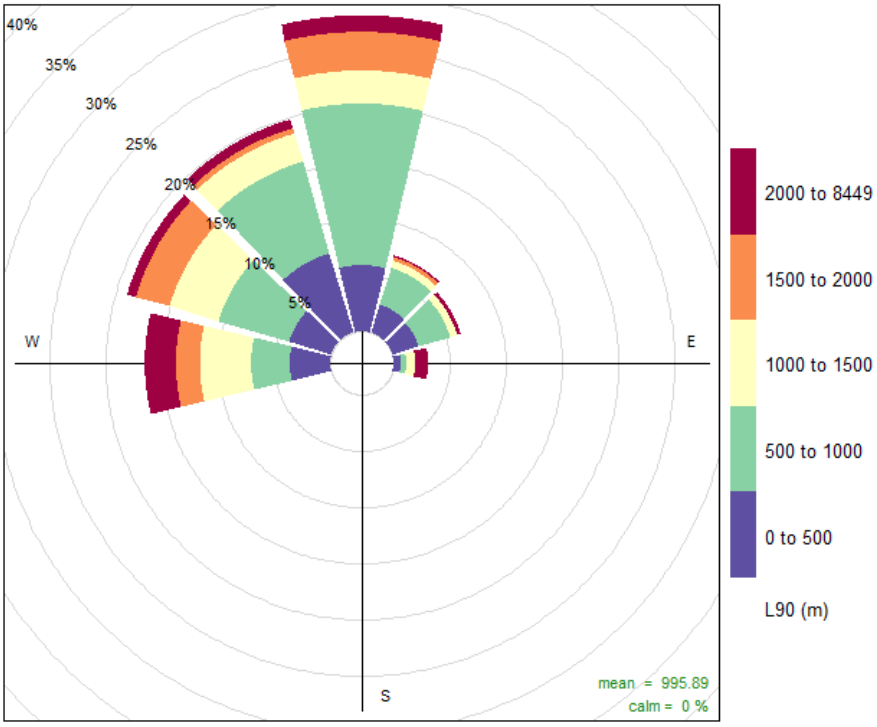

Figure 6.14. L_{90} flux footprint in relation to wind direction; Colour of the wedges indicates L90 in unit of m.

Kljun et al. (2015) described a simple parameterized way to plot flux footprint for prediction purposes if the general wind conditions (including wind direction and wind speed) are known before the measurements, and back tracking purpose with measured wind conditions during field campaign. The main theory behind the two-dimensional parameterization of the footprint functions is based on the ideal concept of a source area contributing to each flux measurements (Schmid, 1994). The concept in a form of three-dimensional illustration is presented in Figure 6.15.

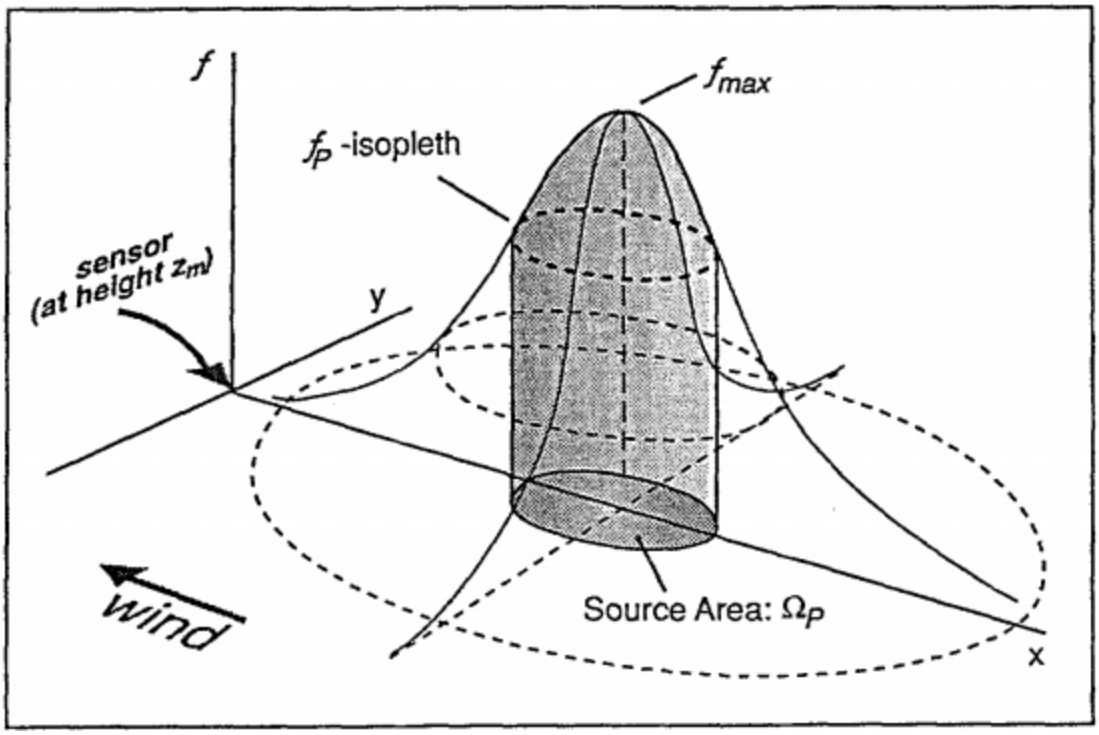

Figure 6.15. Three-dimensional illustration of the source isopleth contributing to sensor measurements (adapted from Schmid, 1994)**.**

As presented in Figure 6.15, the source weight, as represented by f is small for the small separation distance along x-axis. Then the source weight rises to a maximum with increasing distance and then fall off to all directions as the separation increases from the maximum point. The total weight under the integrated source weight function is represented as φ_{tot}. Symbol P represents the fraction of this volume bounded by the isopleth f_P, and the cylinder below, which is hatched in Figure 6.15. The source area of the fraction level, P, is represented as Ω_P, which is the projection of the isopleth f_P on the x-y normal plane. Assumptions include the wind blows towards the negative direction of x-axis, and the turbulence is horizontally homogeneous.

To better understand the two-dimensional source area, Schmid (1994) further illustrated the source area in Figure 6.16. As shown in Figure 6.16, point X_m in the source area represents the maximum source location, which is the upwind point with the maximum contribution to the

concentrations or fluxes measured by the sensor. Symbol a is the near end of the source area and symbol e is the far end of the source area relative to the sensor. And symbol d is the maximum lateral (or crosswind) half-width of the source area.

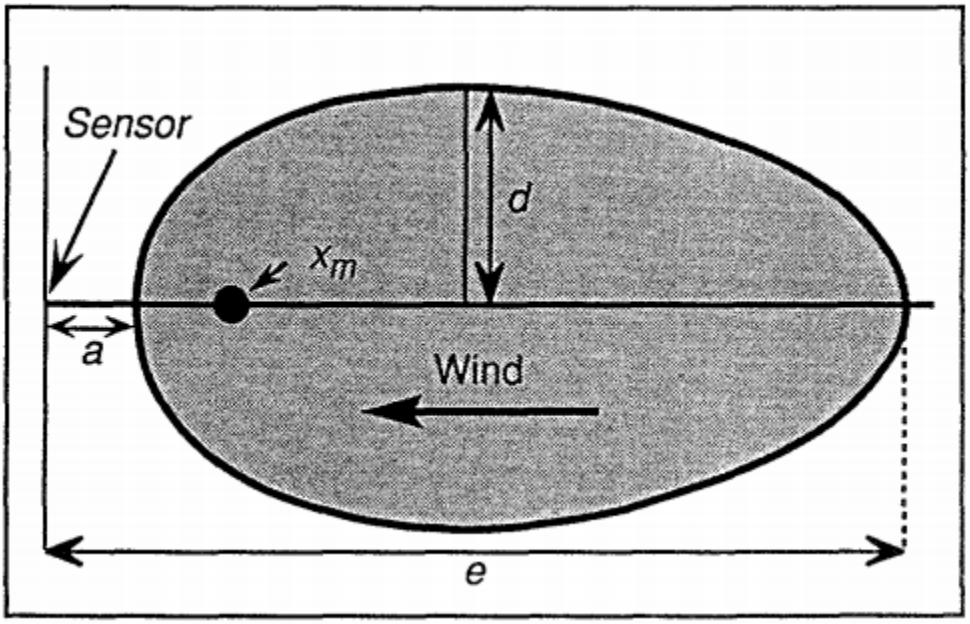

Figure 6.16. Two-dimensional illustration of the source area contributing to sensor measurements (adapted from Schmid, 1994)**.**

Based on the concept of an ideal source area, Kljun et al. (2015) plotted the dispersion simulations of source area calculated from the ideal concept and created a two-dimensional parameterized function of the source area, by adjusting the parameterization function using an unconstrained nonlinear optimisation technique based on the Nelder–Mead simplex direct search algorithm (Lagarias et al., 1998). Based on the parameterization of the calculation for the ideal source area, Kljun et al. (2015) provides a fast and reliable way for calculating the footprint of concentration measurements or flux measurements from EC method. The simple parameterization involves input of timestamps of measurements, measurement height (z_m), displacement height (d), mean wind speed (u_mean), Obukhov length (L), standard deviation of lateral velocity fluctuations (σ_v), friction velocity (u^*), and wind direction. By utilizing the online

footprint generating tool provided by Kljun et al. (2015), Figure 6.17 is generated as a footprint plot for illustrating the source areas of the flux measurements after QA/QC.

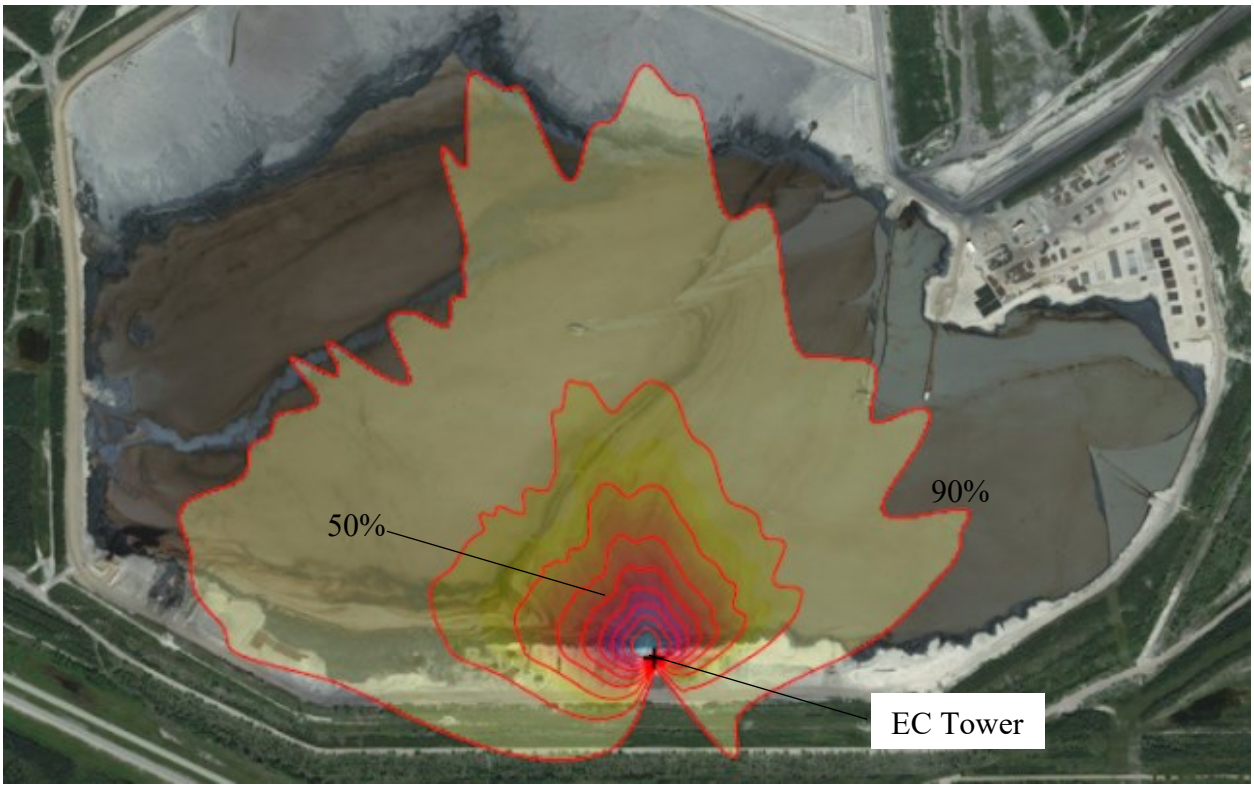

Figure 6.17. Flux footprint (L_{10} to L_{90}) illustration of the filtered flux measurements of CH_4.

As shown in Figure 6.17, the location of EC tower is marked as a small cross at the south edge of the tailings pond. Footprint contour lines are shown in steps of 10% from 10% to 90%. The 50% source contribution contour line and the 90% source contribution contour line are marked in the figure. After QA/QC, the majority of source areas contributing to the flux measurements lie within the boundary of the pond. Only a small portion of the source contribution comes from outside of the tailings pond to the south of the EC Tower as shown in Figure 6.17.

6.1.7 Stability Analyses

Figure 6.18 presents the relationship between measured vertical speed standard deviation (σ_w) and mean horizontal wind speed ($\bar{u}$). Data presented in Figure 6.18 are filtered by wind direction, and error message (-9999 in EddyPro output).In Figure 6.18, vertical wind speed standard deviation changes positively with respect to the mean horizontal wind speed. This is an expected pattern of the ratio between σ_w and $\bar{u}$, as vertical turbulence intensity remains consistent above homogeneous water surface (Brown, 2013).

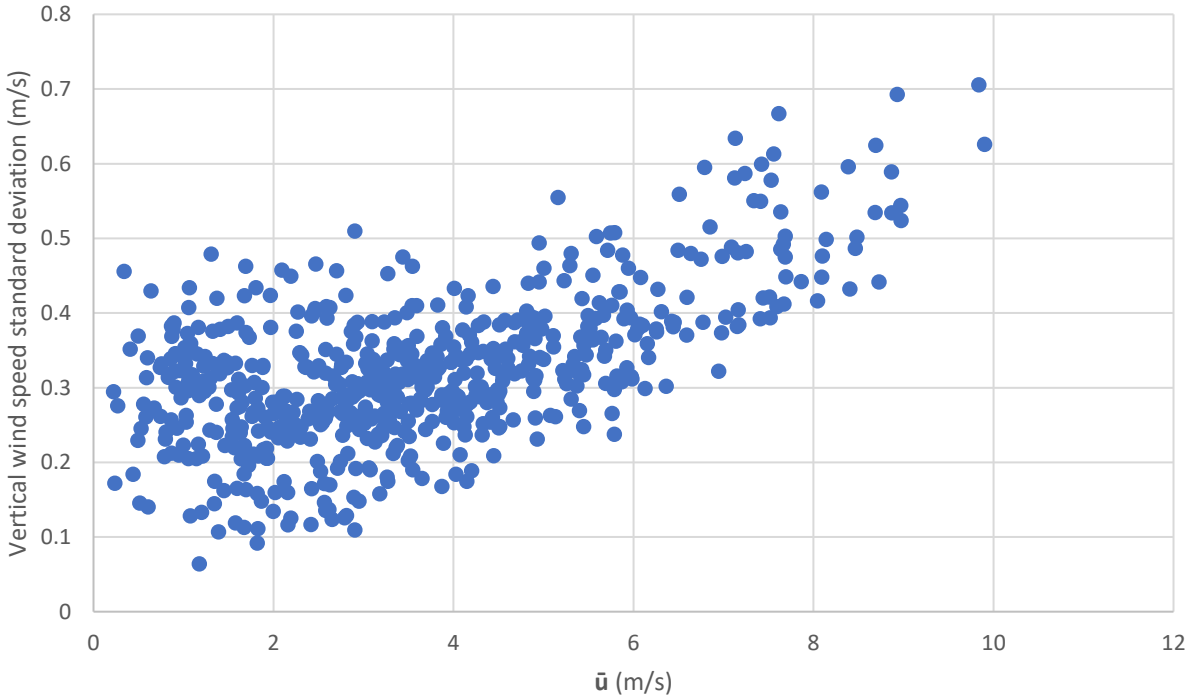

Figure 6.18. Vertical wind speed standard deviation (σ_w) in relation to mean horizontal wind speed ($\bar{u}$).

Figure 6.19 presents the variation of mean horizontal velocity ($\bar{u}$) and stability of the surface atmospheric layer, as indicated by the dimensionless Obukhov stability parameter, z/L. Data in Figure 6.19 are filtered by wind direction and error output (-9999 output of z/L and $\bar{u}$). 92% of the z/L values are negative and close to zero, which means the dominant atmospheric condition

over measured water surface is unstable and neutral (Kaimal and Finnigan, 1995). As ū value increases, z/L value starts to converge closer to 0. Since the Obukhov length is proportional to friction velocity (u^*) (Kaimal and Finnigan, 1995), u^* is proportional to mean horizontal wind speed (ū), and ū increases; therefore, L increases, which lead to z/L closer to 0 (neutral stability condition).

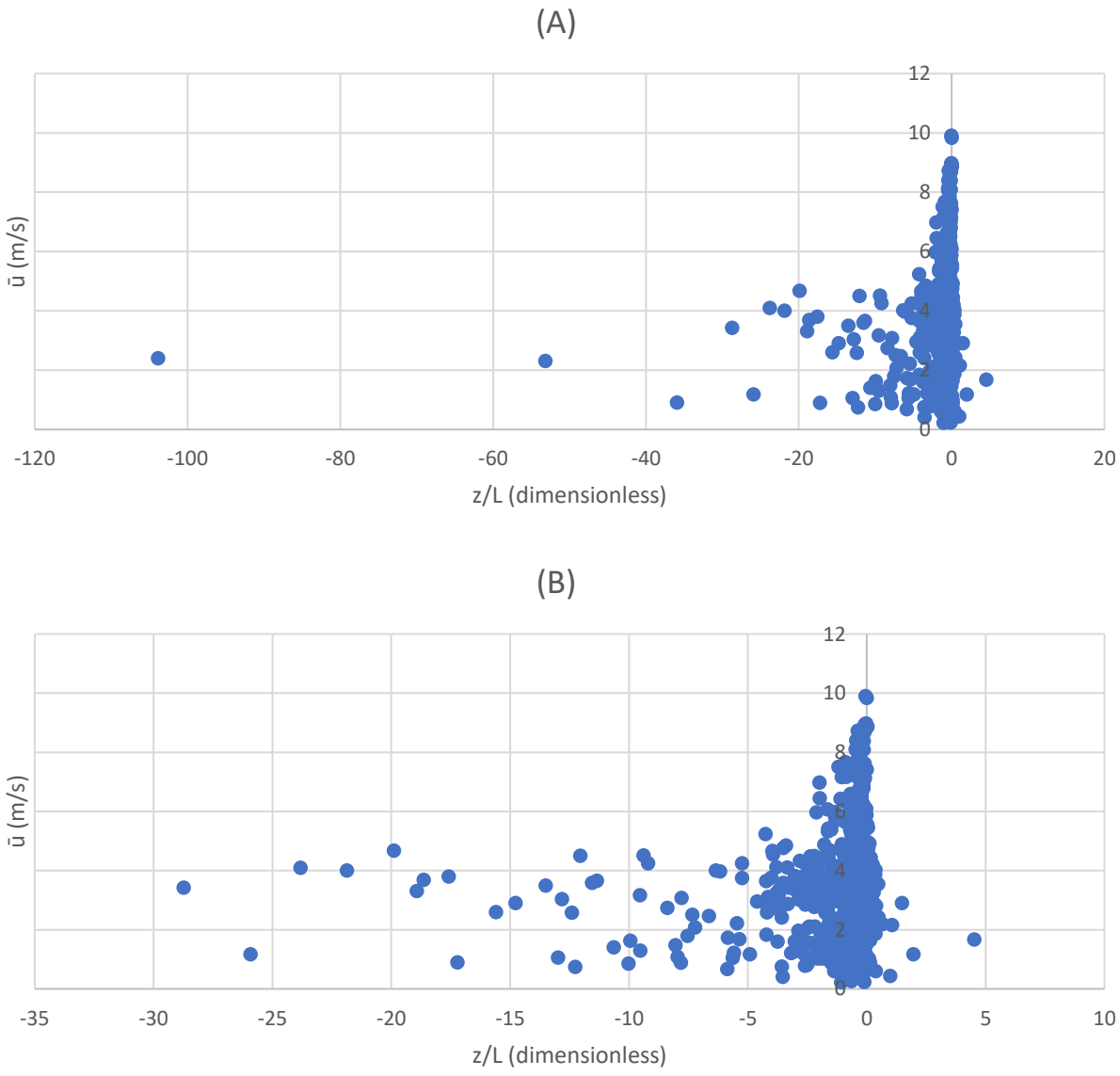

Figure 6.19. Mean horizontal wind speed (ū) in relation with stability (z/L); (A): full scale; (B): zoom in.

Figure 6.20 shows the variation of L_{90} footprint with respect to stability, z/L. L_{90} values increase as z/L values converge closer to 0. The possible reason for the pattern in Figure 6.20 is the positive correlation between mean horizontal velocity and L_{90} values shown in Section 6.1.6.

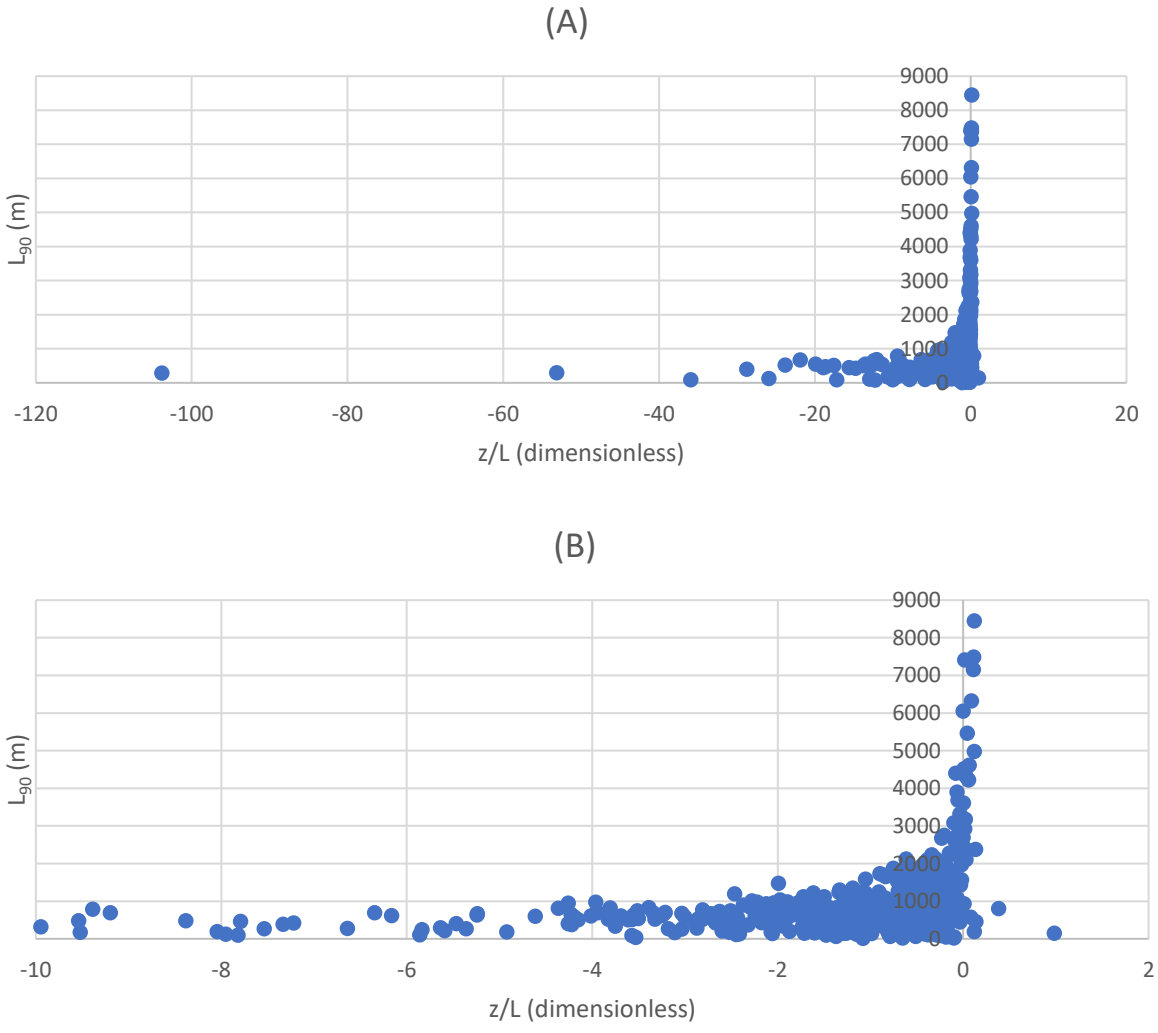

Figure 6.20. L_{90} footprint in relation to stability (z/L); (A): full scale; (B): zoom in.

6.1.8 Daily Composite Variation Comparison

Composite diurnal values are obtained by averaging all valid fluxes and temperatures for each hour period of each day during the field campaign. Figure 6.21 compares the diurnal variation of CO_2 fluxes and air temperatures. Average CO_2 fluxes do not depict a clear pattern between midnight and 8:00, and the variation does not match with the variation of temperature. From 8:00 to 22:00, variation of CO_2 fluxes generally matches the variation of the air temperature. From 18:00 to 8:00 of the next day, average CO_2 fluxes rise and fall and drop below zero for several times, while temperature kept dropping to the lowest point (at 8:00). Hourly median CO_2 fluxes are different from average CO_2 fluxes, since fewer data is available for data analyses during nighttime. Generally, more CO_2 fluxes are positive, however, negative fluxes may affect the hourly average of CO_2 fluxes more than median of CO_2 fluxes when less data is valid for flux analyses. Consistently positive CO_2 fluxes are observed during the day indicating the emissions of CO_2 from the pond at higher atmospheric temperature. Sawyer et al. (2003) stated CO_2 solubility decreases as temperature of water increases, therefore, CO_2 emission from water body may increase as the environment temperature (including both air and water temperature) increases. Negative fluxes means the pond is a sink for CO_2 (e.g. pond absorbing CO_2). Previous studies using eddy covariance for measuring GHG fluxes from oil sands tailings ponds reported occurrence of negative fluxes (Brown 2013; Zhang et al., 2019).

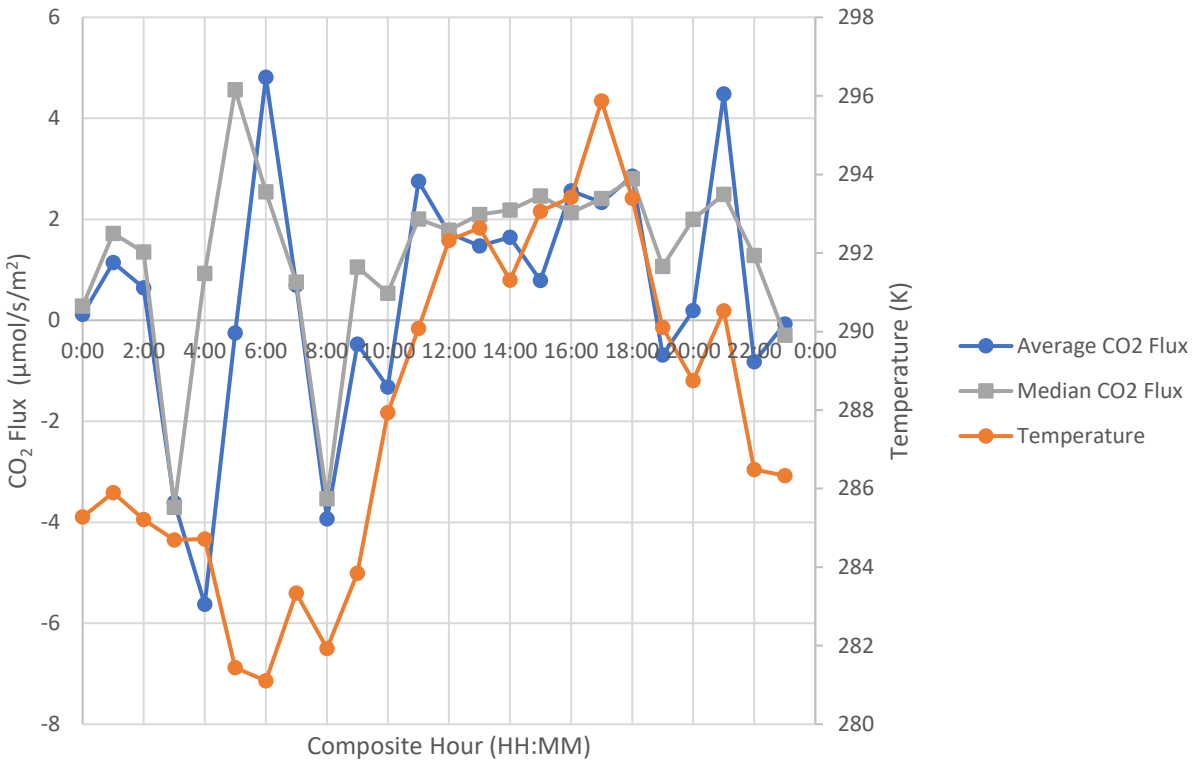

Figure 6.21. Composite diurnal variation of CO_2 flux and temperature.

Figure 6.22 depicts the variation of CH_4 fluxes and temperature as a daily composite plot. All CH_4 fluxes are positive indicating the pond is a source of CH_4 emissions. The CH_4 fluxes does not drop below zero, and the pattern of variation generally matches the variation of air temperature. During nighttime (18:00 to 8:00 of the next day), CH_4 also rise and fall for several times, as air temperature generally drops to the lowest value at 8:00. Unlike CO_2 fluxes, variation of median CH_4 fluxes matches variation of average CH_4 fluxes, since CH_4 fluxes are relatively stable during this field campaign.

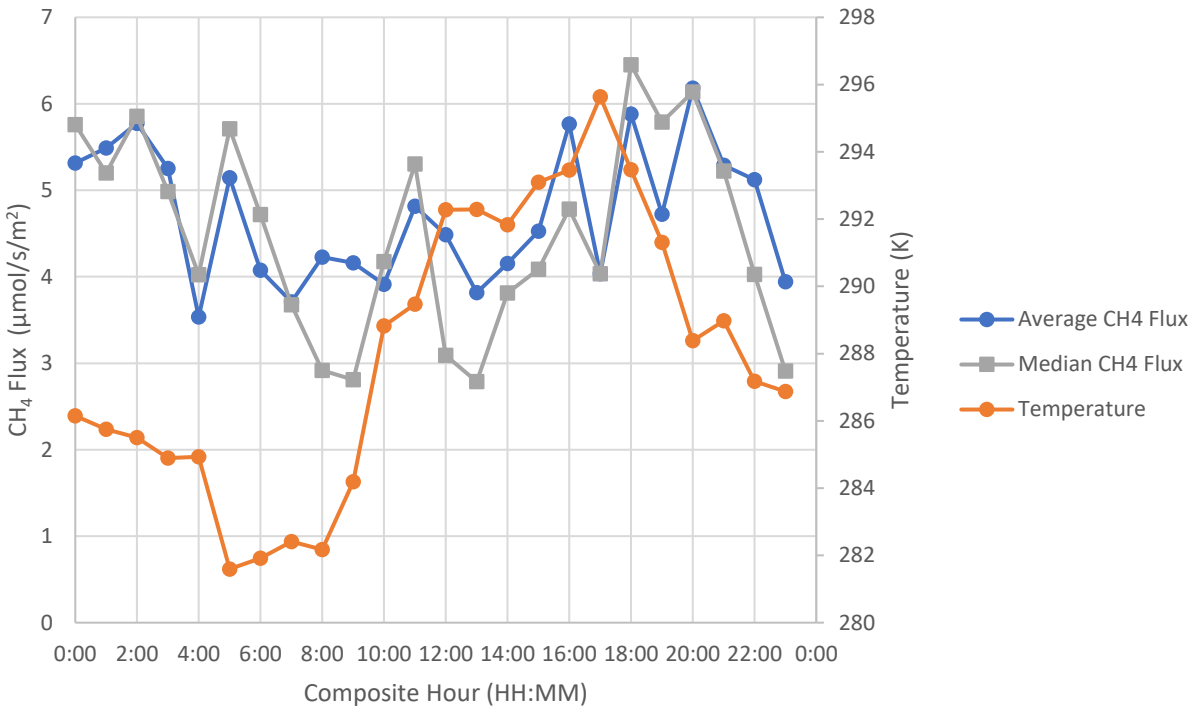

Figure 6.22. Composite diurnal variation of CH_4 flux and temperature.

Figure 6.23 shows the diurnal variation of median CO_2 and CH_4 fluxes. Generally, variation of median CH_4 fluxes follows a similar pattern to the variation of CO_2 fluxes. While CO_2 fluxes go below zero, indicating CO_2 sink into the target tailings pond (which may be an artifact caused by the CO_2 analyser failure), CH_4 fluxes remain above zero at the lower range of the CH_4 flux values.

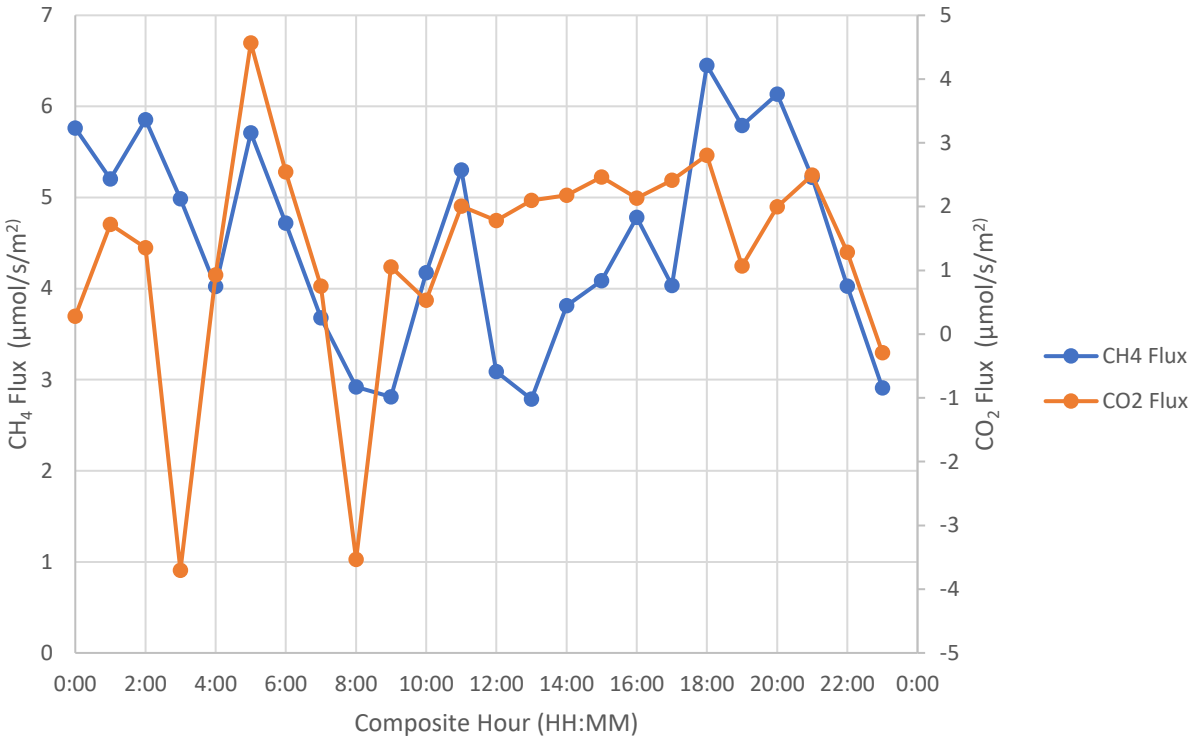

Figure 6.23. Composite diurnal variation of median CH_4 and CO_2 fluxes.

Figure 6.24 and Figure 6.25 show the variation of CO_2 fluxes and CH_4 fluxes with the variation of the count of filtered data available for the averaging process for daily fluxes values. Both Figure 6.24 and Figure 6.25 indicate more available data during daytime, while both CO_2 and CH_4 fluxes are higher than average fluxes. Burba (2013) confirms that more data loss during night is reasonable due to relatively calmer atmospheric condition. During nighttime, some of the averaging hours only contain 5 to 10 counts of data available. Therefore, the quality of the daily composite plot during nighttime may not be reliable due to limited number of valid data points. In Figure 6.24, large differences between average CO_2 fluxes and median CO_2 fluxes appear where the count of available data is relatively low. The median CO_2 fluxes are generally higher

than average CO_2 fluxes, suggesting high magnitude of negative fluxes driving down the average CO_2 fluxes value during diurnal data analyses.

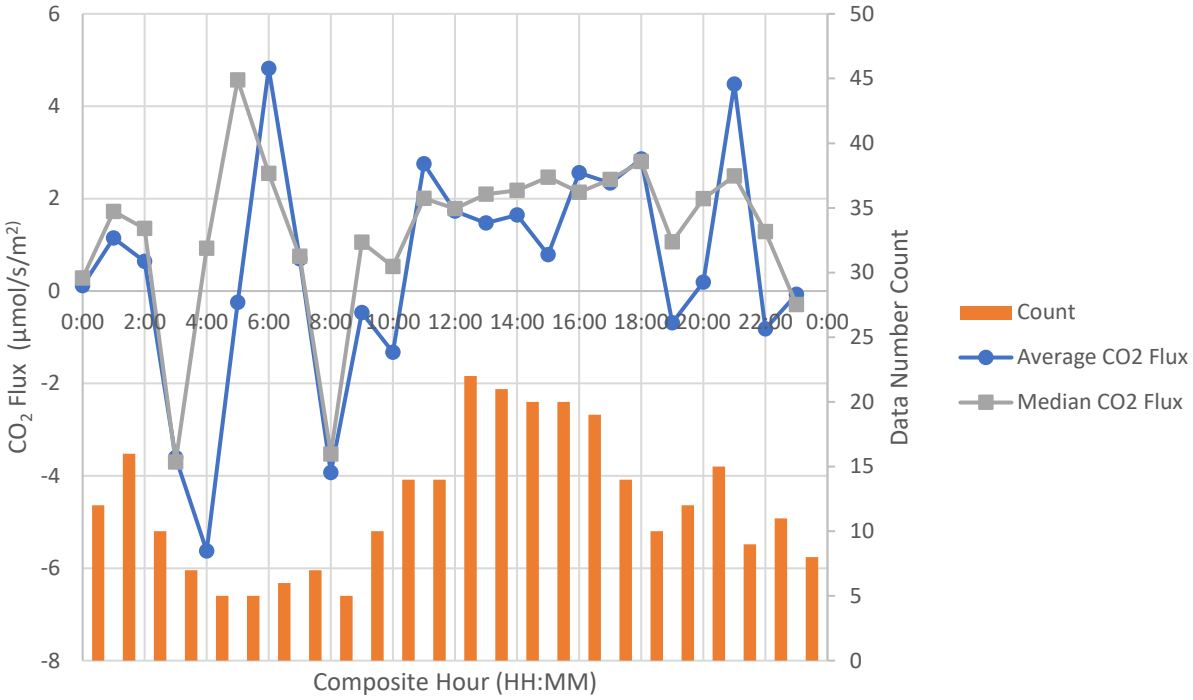

Figure 6.24. Composite diurnal variation of CO_2 fluxes and data count.

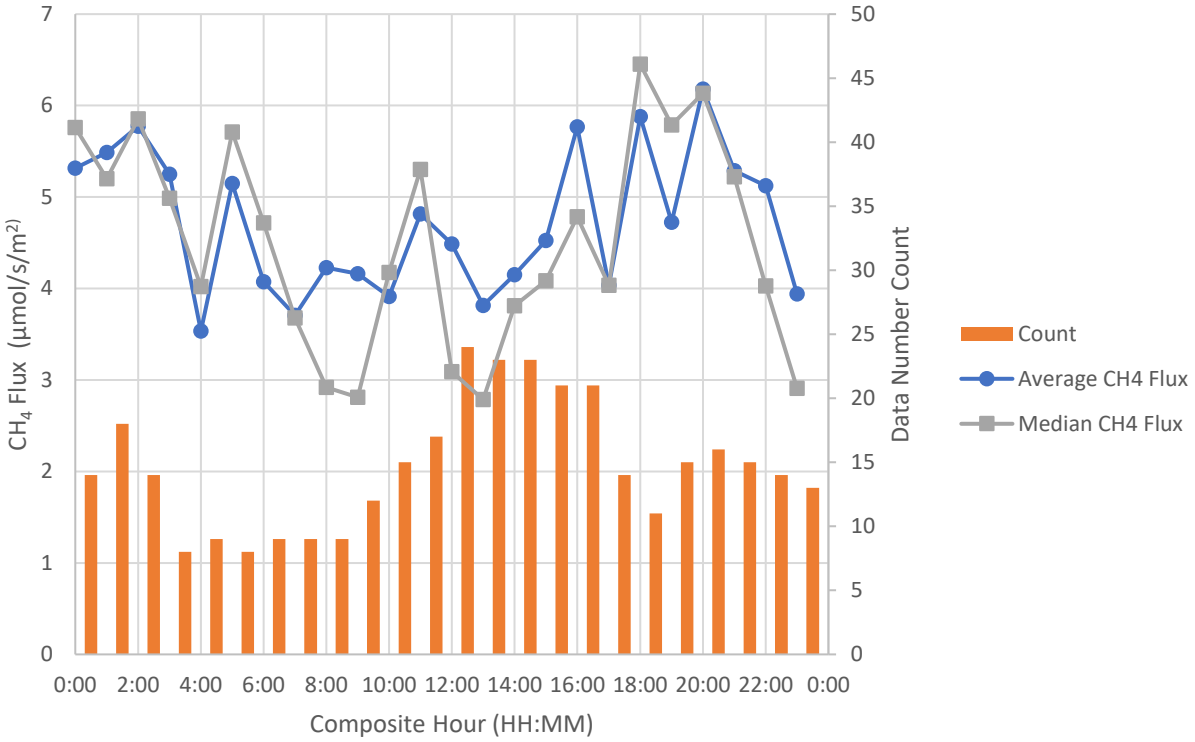

Figure 6.25. Composite diurnal variation of CH_4 fluxes and data count.

Figure 6.26 and Figure 6.27 relate the variation of CO_2 and CH_4 fluxes to variation of standard deviation for the same set of fluxes data for diurnal averaging. Figure 6.26 shows that standard deviation values of CO_2 are higher during nighttime than daytime. As suggested in Figure 6.24, the lower the count of available flux data, the higher the standard deviation of the flux data, and the larger the differences between median CO_2 flux values and average CO_2 flux values. However, the standard deviation of CH_4 fluxes during daytime and nighttime are not too different (Figure 6.27).

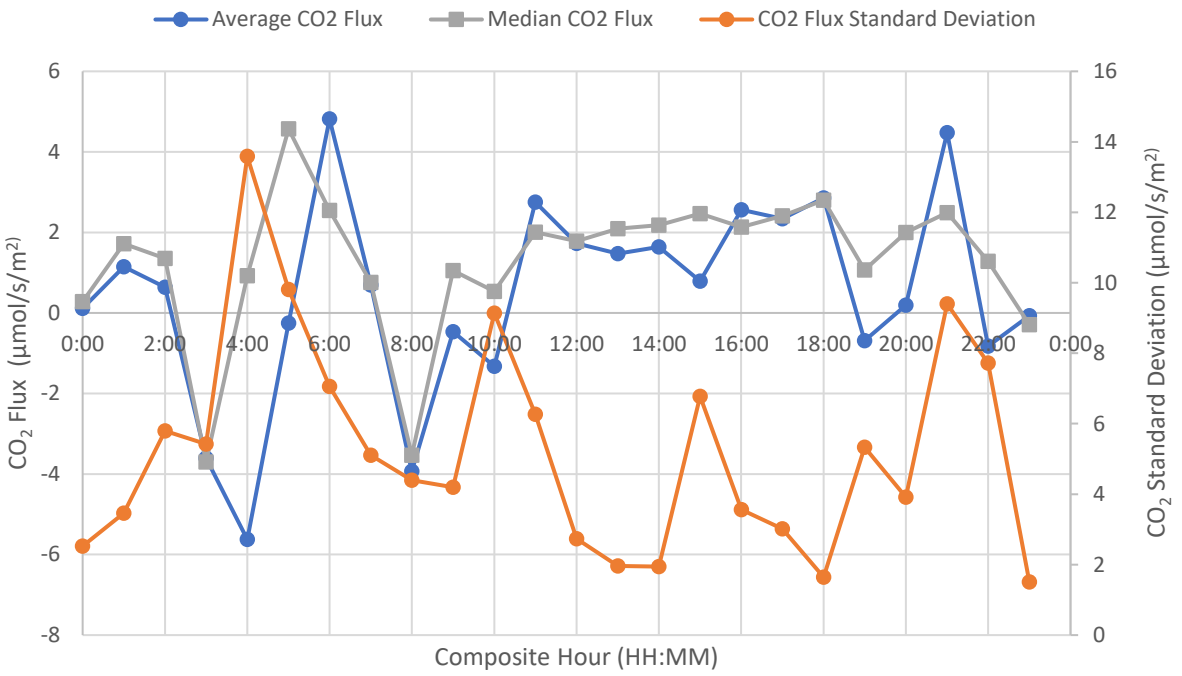

Figure 6.26. Composite diurnal variation of CO_2 fluxes and CO_2 standard deviations.

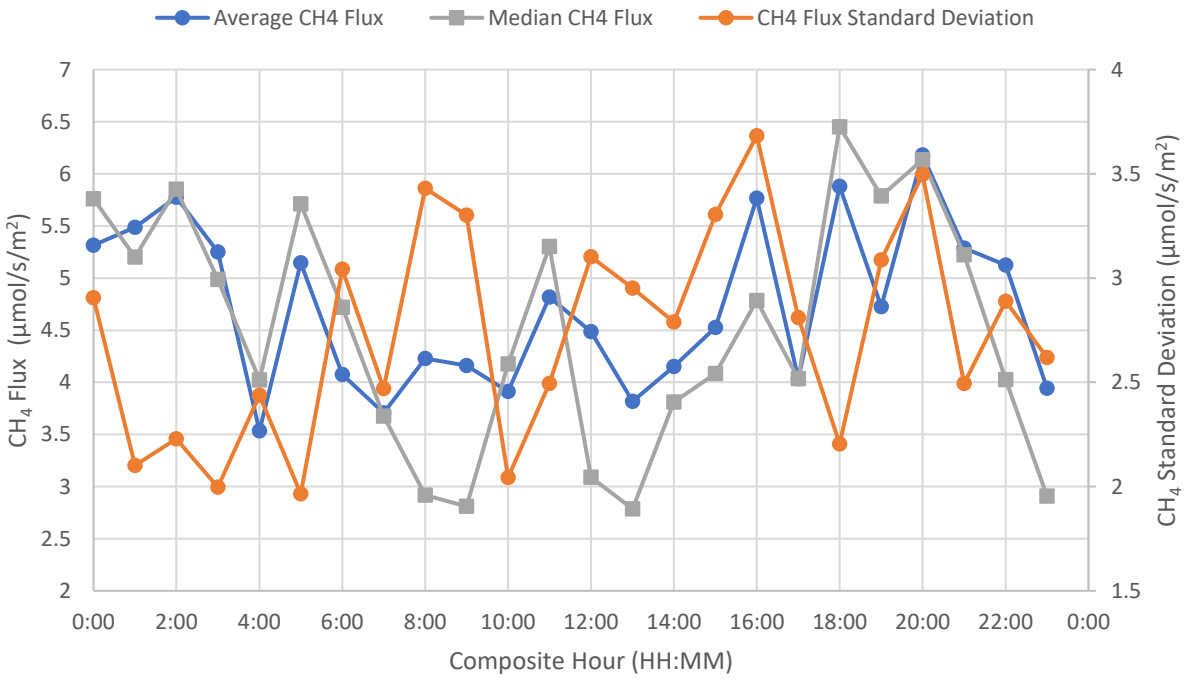

Figure 6.27. Composite diurnal variation of CH_4 fluxes and CH_4 standard deviations.

Although fluxes calculations utilize concentration values, the variation of concentration values do not necessarily match the variation of fluxes. Figure 6.28 presents the variation of CO_2 fluxes with the variation of CO_2 concentrations. In Figure 6.28, higher CO_2 concentrations are observed when low CO_2 fluxes are observed. The difference between variation of CO_2 fluxes and CO_2 concentrations are noticeable, since fluxes reflect the change of concentrations more than the measured concentration values (Burba, 2013). CO_2 concentrations are generally higher during early morning. Similarly, Figure 6.29 presents the variations of CH_4 fluxes and CH_4 concentrations in a daily composite plot. Variation of CH_4 fluxes does not match the variation of CH_4 concentrations as well.

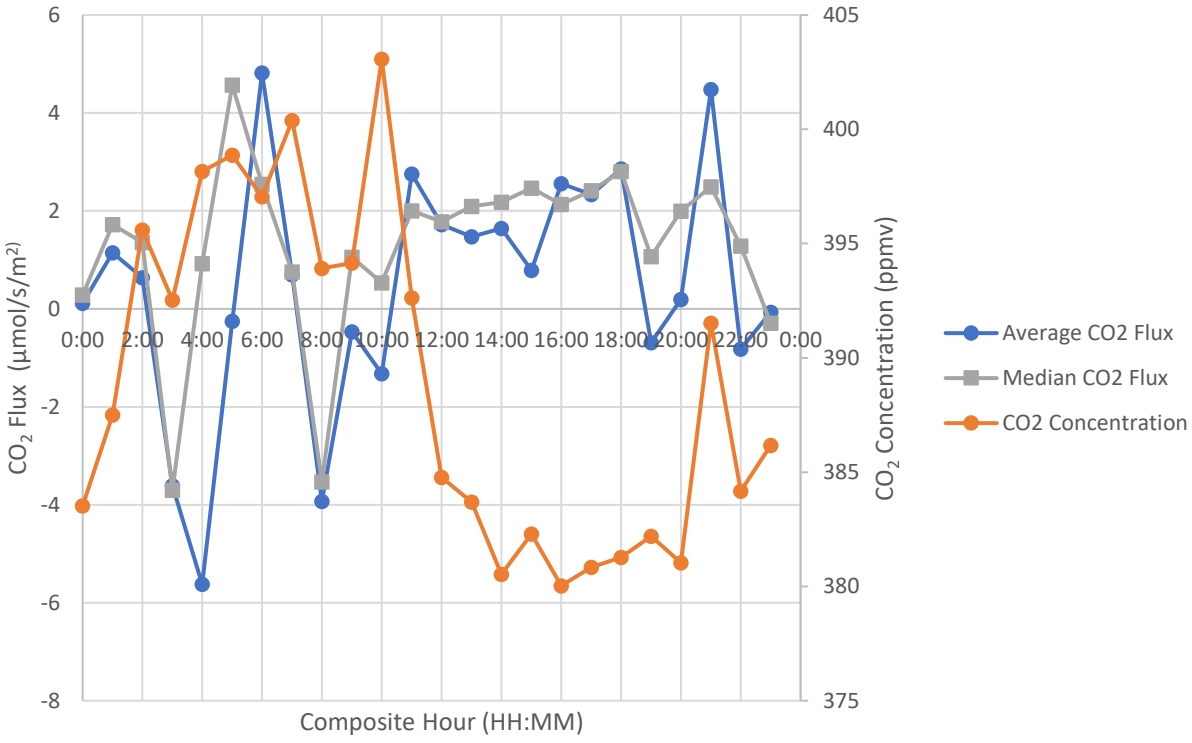

Figure 6.28. Composite diurnal variation of CO_2 fluxes and CO_2 concentrations.

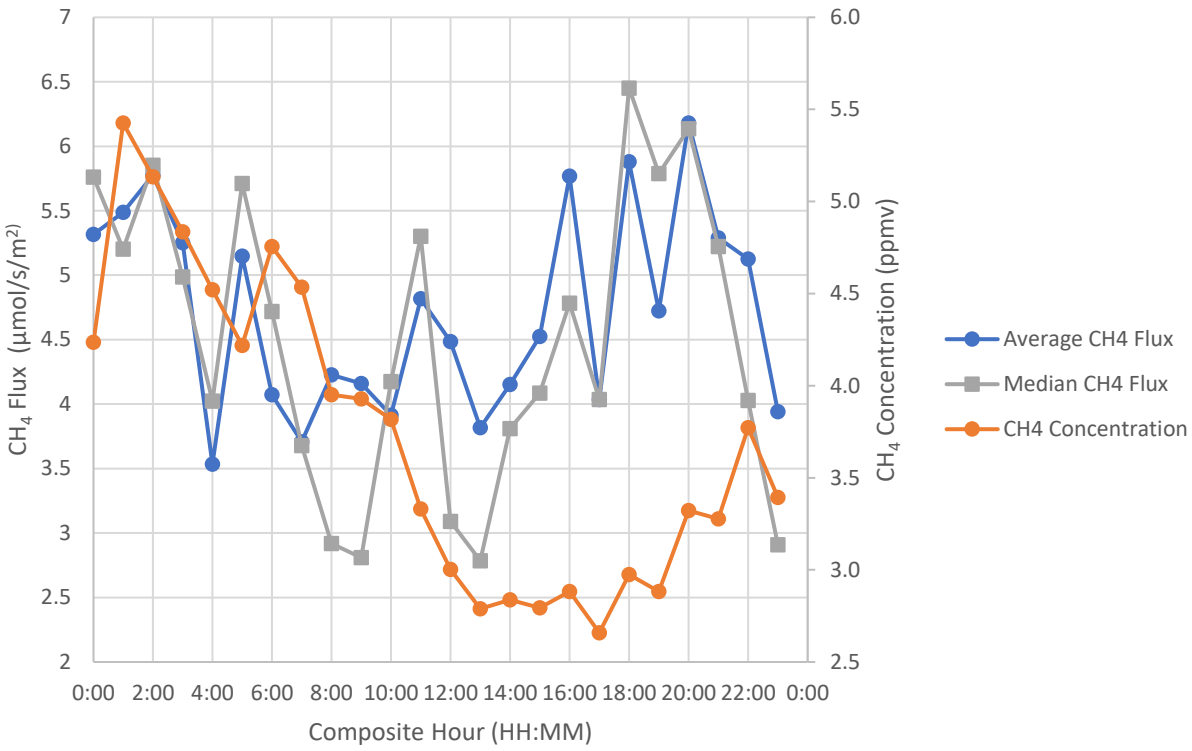

Figure 6.29. Composite diurnal variation of CH_4 fluxes and CH_4 concentrations.

6.1.9 Flux Hotspot

R programming has polarPlot function which plots a bivariant polar plot of variables. In polar plot, the flux of the pollutant of interest is plotted against wind direction and a secondary variable. The secondary variable can be peak footprint of the variable of interest, which represents the distance from the anemometer in the direction from which the largest relative individual contribution to the flux originates (LI-COR, 2016). Such a plot can help qualitatively visualize the emissions hot spots. Figure 6.30 and Figure 6.31 show the CO_2 and CH_4 flux hotspots, respectively, as a function wind direction and peak footprint. The weight ratio of each cluster of drawings is set to 1, which means the cluster would represent the full value of the represented data, even if only one point of data exists inside this cluster. In Figure 6.30, high

CO_2 fluxes mainly come from northwest direction with respect to the flux measurement tower. Figure 6.31 also shows major CH_4 fluxes come from the northwest direction of the flux measurement tower.

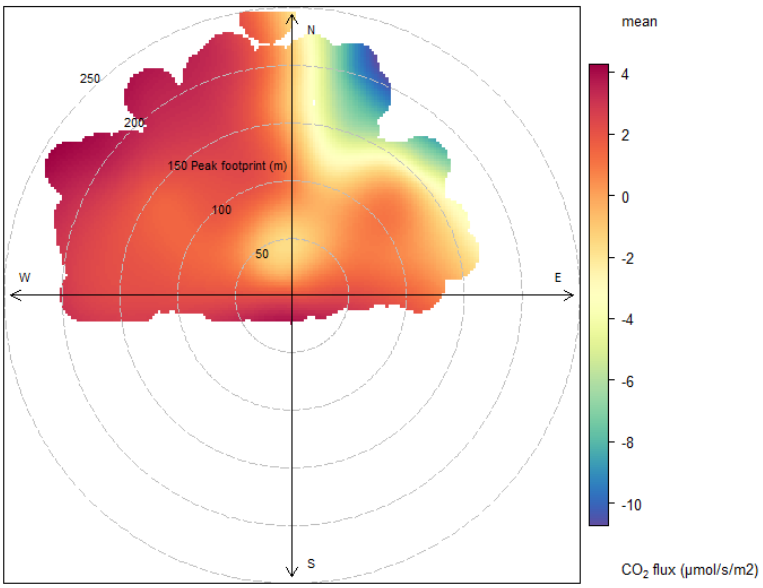

Figure 6.30. Polar plot showing hotspots of CO_2 flux.

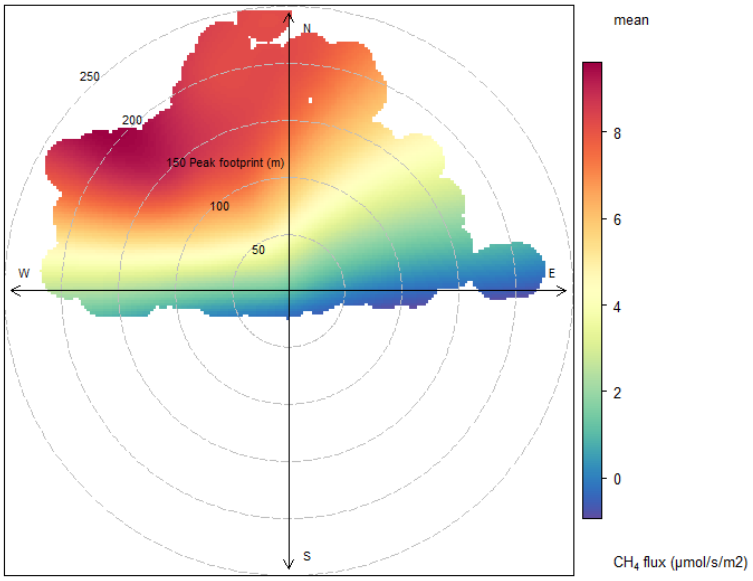

Figure 6.31. Polar plot showing hotspots of CH_4 flux.

6.2 Limitations and Recommendations

6.2.1 Limitations

As stated in Section 2.5.2 of this thesis, real condition should be at least close to major assumptions to allow reliable flux determination by EC method. One aspect of EC tower design is that the 90% flux footprint needs to be representative of the entire water surface (Burba, 2013), while eliminating flux outside the boundary of the target source. The EC tower footprint depends on the tower height and atmospheric stability. If EC tower is set at an elevation to cover the entire target source, for some atmospheric condition, calculated 90 percent flux footprint (L_{90}) exceed the distance between the source boundary and the EC tower (e.g. Figure 6.11 and Figure 6.12). On the other hand, if EC tower elevation is set too low, flux measurements may not represent the entire area of the target source. Therefore, choosing an appropriate EC tower elevation is important to obtain representative fluxes from a target source.

Wind direction often limits the performance of the EC measurements. During this field campaign, south wind was dominant, and wind direction data filtration discarded more than 75 percent of the total measured data. For better EC measurements, an additional EC tower set at the opposite side of the target pond may provide complementary measurements to minimize data loss due to unfavorable wind directions, better understand the emission from the target pond, and double check the measurements.

Burba (2013) also stated that during low wind speed conditions (especially during nighttime), other transportation mechanisms of constituents such as diffusion and advection may take place, and therefore largely impact turbulence measurements. In this thesis, fluxes measured at low

wind speed (lower than 1 m/s) are not discarded since Figure 6.7 and Figure 6.8 do not show any concerning flux values, such as negative fluxes, at low wind speed ranges. In addition, rain may affect both the measured flux and measurement condition of the EC tower. Slight tilt of gas analysers may help drains the rain drops quicker, however, impact of rain could not be completely avoided. Since RSSI of both gas analysers drops to unacceptable values during raining periods, therefore, completed data filtration excludes data measured in rain condition.

EC tower location is often desolate, and therefore frequent access to EC tower sites can be challenging. During this field campaign, utilization of datalogger and modem to remotely monitor the operational condition of EC instruments greatly reduced the pressure of routine EC measurement quality check. Once a problem occurs, an inspection and maintenance trip can be arranged within reasonable time to avoid large data loss. However, regular maintenance is still necessary to replenish the washer reservoir for LI-7700 mirror cleaning, and to ensure enough air supply to the air nozzles system for dust clean up.

EC tower measurement height may be limited by the length of signal cable and pump capacity of the washer reservoir. The installed pump for LI-7700 washer reservoir may only provide pumping capacity up to 5 metres. Therefore, to avoid high level operation with boom lift, an extra pump may be necessary to pump the washer liquid into the washer reservoir for effectively cleaning to maintain an appropriate LI-7700 RSSI automatically.

6.2.2 Recommendations

During this study, one major issue is associated with the gas analyzer malfunction due to improper usage of outdated connection cables. For future success of EC measurements activities,

proper instrument management tools including detailed label of all key instruments and clear documentation of best available instruments will be beneficial.

The predominant wind direction is important for catching the majority of fugitive GHGs emission information from the source surface area. Therefore, a reliable understanding of potential predominant wind direction and speed in form of wind rose within the testing area and testing time would be the key for efficient field data measurements. One major recommendation from this study is to deploy two EC towers at the opposite side of the target tailings pond to complement measurement gaps of one EC tower measurements caused by variation of wind direction.

Because EC technique requires fast response gas analyzers, it is mostly used for GHG emission flux measurements. Since fast response gas analyzers for measuring VOCs concentrations are not readily available, relaxed eddy covariance technique (a variant of eddy covariance technique) is suggested for VOCs emission flux measurements in future field campaigns. However the applicability of such technique in the oil sands environment still needs to be validated.

6.3 Discussion on Flux Measurements

Equation 64 of EddyPro manual (LI-COR, 2016) reveals the core of flux calculation based on molar density measurements by LI-7500A, where both the change of vertical wind velocity and the change of measured molar density averaged during the 30 minutes period determine whether calculated flux is positive or negative. If the target tailings pond keeps emitting CO_2 gas into the atmosphere, both the change of vertical velocity and the change of CO_2 concentrations should be positive in theory, and vise versa. Therefore, negative vertical wind velocity does not mean a

negative flux, and low CO_2 concentration measurements do not contribute to negative fluxes directly as well.

As stated in Section 5.4, average/median CO_2 fluxes measurement during this field campaign are markedly lower than previous measurements of CO_2 fluxes using a flux chamber. During this field campaign, flux calculation provides considerable amount of negative CO_2 fluxes, suggesting carbon sink into the tailings pond may be possible mainly at nighttime. The following discussion suggests several possible reasons behind this difference.

The first reason is that an instrument error occurred during the field campaign. During the field campaign, one extension cable connecting LI-7500A CO_2 gas analyser and the analyser interface unit was exchanged due to unacceptable LI-7500A diagnostic value indicating chopper house temperature issue. After replacing the extension cable, the diagnostic values turned normal, and did not indicate chopper house temperature issue anymore. Normally, condensation on the inner source lens and inappropriate chopper house temperature may cause alarming diagnostic values indicating system problems. However, even diagnostic values turned normal after chopper house issues, instrument overheating and condensation (as discussed in Section 5.1) may cause system offset, and the instrument may require repair and factory calibration. Based on Figure 5.9, CO_2 flux measurements were higher from Day 209 (July 28, 2017) to Day 216 (August 4, 2017), before the extension cable was replaced. After replacing the extension cable, more frequent negative values of CO_2 fluxes start to show up with wider spread of CO_2 concentration measurements (Figure 5.5-A). Wider range of CO_2 concentrations suggest more variations of CO_2 concentrations, and lead to wider range of CO_2 fluxes. Therefore, it is possible that more flux values were negative due to condensation and chopper house overheating, causing unknown

instrument error that does not affect diagnostic and RSSI output from the instrument. However, even after diagnostic problem, CO_2 fluxes from south of the EC tower are more consistently above zero (shown in Figure 6.9), which suggests there may be other reasons for calculated large negative fluxes.

The second reason behind the negative CO_2 fluxes may be the nature of the microbial processes in the tailings pond. Metabolism of naphtha such as alkanes and BTEX (benzene, toluene, ethylbenzene, xylenes) hydrocarbon produces acetate and H_2 (Stasik and Wendt-Potthoff, 2016). Then acetate may go through acetoclastic microbial metabolism into CH_4 and CO_2 directly. Acetate-oxidizing bacteria may also transform acetate into H_2 and CO_2, then hydrogenotrophic methanogens consume both H_2 and CO_2, to produce CH_4 and H_2O. Burkus et al. (2014) predicted the molar ratio between CO_2 emission and CH_4 emission vary based on the diluent type. As paraffinic (P), Naphtha (N8) light, and Naphtha (N10) heavy diluent ideally emit GHGs in CO_2/CH_4 weight ratio, 1/1.38, 1/1.30, and 1/1.25 correspondingly. During this field campaign, the weight ratio between measured CO_2 fluxes and CH_4 fluxes (median values) is 6.835 $g/m^2/d$ CO_2 flux divided by 6.470 $g/m^2/d$ CH_4 flux, which equals to around 1/0.95. This weight ratio value is smaller than the value predicted by Burkus et al. (2014), but not too far from ideal methanogenesis output. Methanogenesis is never an ideal process, therefore the model prediction can be different from the real emission scenario. However, methane oxidation and presence of sulphate may heavily inhibit the production of CH_4 during microbial process in the tailings pond, therefore, in terms of weight, CO_2 emission is usually larger than CH_4 emissions from tailings pond (Small et al., 2015). According to Sawyer et al. (2003), CO_2 has a much higher solubility in water than CH_4, leading to easier CH_4 release from the water surface, and may contribute to more CH_4 emission than CO_2 emission in short term. Therefore, it may be possible for CH_4

fluxes to be higher than historical measurements for this target pond, while CO_2 fluxes less than historical measurements. Since CH_4 production consumes CO_2, as tailings pond ages with FTT input (Burkus et al., 2014), CH_4 fluxes may increase and CO_2 fluxes may decrease. However, further investigation is necessary to understand if microbial process is important enough to cause large amount of short-term CO_2 sink into the tailings pond.

Low turbulence during low wind speed (correlation shown in Figure 6.15), especially at nighttime, suggests flux measurements during low wind speed may be unreliable (Burba, 2013). However, in Figure 6.7, major negative CO_2 fluxes occur at moderate wind speeds, and therefore low turbulence may not be the reason for negative CO_2 flux measurements during this field campaign.

6.4 COMPARISON WITH AVAILABLE DATA

Environment and Climate Change Canada (ECCC) conducted flux measurements at the same tailings pond from August 6th, 2017 to September 9th, 2017 (You et al., 2021). The technologies used by ECCC include EC, flux vertical gradient method, IDM, and flux chamber. Table 6.1 summarizes the CH_4 flux measurements from this study and from ECCC's study. The table shows the 25th percentile (Q_25%), median (Q_50%), 75th percentile (Q_75%) and mean CH_4 flux values (± standard deviation) obtained from data after all QA/QC procedures.

Table 6.1. Minimum, maximum, median and average fluxes of CH_4 for the entire field campaign (unit in g/m^2/d).

Flux method	Q_25%	Median	Q_75%	Mean
EC UofA (this study)	3.4	6.5	9.3	5.9 ± 2.7
EC ECCC*	5.6	7.4	9.8	7.8 ± 1.1
Gradient*	3.8	6.1	11.0	7.2 ± 3.5
IDM*	3.6	5.2	6.6	5.4 ± 0.4
Flux Chamber*	2.0	2.3	3.8	2.8 ± 1.4

* (You et al., 2021).

In Table 6.1, Statistics and average fluxes are area weight-averaged for EC, flux vertical gradient, and IDM methods. For flux chamber measurements, statistics and average are based on 15 measurements using flux chambers (You et al., 2021). The CH_4 measurements obtained in this thesis using EC from July 28, 2017 to September 29, 2017 resulted in an area-weighted CH_4 mean flux value of 5.9 g/m^2/d and a CH_4 median flux value of 6.5 g/m^2/d. Table 6.1 reveals that EC method provided the highest median flux as 7.4 g/m^2/d (ECCC result), while flux chamber method provided the lowest median flux measurement as 2.3 g/m^2/d. Flux chamber measurements can not reflect the temporal and spatial heterogeneity of the tailings pond water surface (Denmead, 2008). Therefore, the flux chamber method introduces high uncertainty into the flux measurements and can not capture the variation of the GHG fluxes from the tailings pond. You et al. (2021) also mentioned that CH_4 flux emission estimates from this tailings pond were 5.3 g/m^2/d in 2016 and 11.1 g/m^2/d in 2018. According to Small et al. (2015), the CH_4 flux estimate at this site is 9.45 t/ha/y in 2012, which equates to 2.60 g/m^2/d. The percentage difference between the median CH_4 flux measurement value from this study (6.5g/m^2/d) and that provided by ECCC (7.4 g/m^2/d) is calculated by the following equation:

$$\frac{7.4\ \mathrm{g/m^2/}d - 6.5\,\mathrm{g/m^2/}d}{7.4\ \mathrm{g/m^2/}d} \times 100\ \% = 12\ \%$$

The percentage difference of 12 % is a reasonable value considering the different instrument height, setup location, operational time, and systematic randomness. The median CH_4 flux measurement value of 6.5 $g/m^2/d$ also falls in the range historical measured flux values from 2.6 $g/m^2/d$ to 11.1 $g/m^2/d$.

Both historical flux chamber measurements (Small et al., 2015) and concurrent flux chamber measurements (You et al., 2021) were generally lower than EC flux measurement results. additional EC flux measurements on the oil sands tailings ponds would provide regulatory agencies and oil sands companies better understanding of the fugitive emissions from the tailings ponds and allow further assessment of the economy, efficiency and reliability gain from implementing the EC technique.

Figure 6.32 depicts the dependence of CH_4 flux values (quality data) obtained in this study on wind direction and reveals the relationship as a box and whisker chart. The EC flux data rearranged based on the wind direction divided in every 22.5 degrees. The upper bar represents maximum, lower bar represents minimum, middle bar represents the median, and the dot/cross represents the average of the CH_4 values categorized in each bin. Each box is also bound on the top by the third quartile of the binned flux values and on the bottom by the first quartile of the binned flux values.

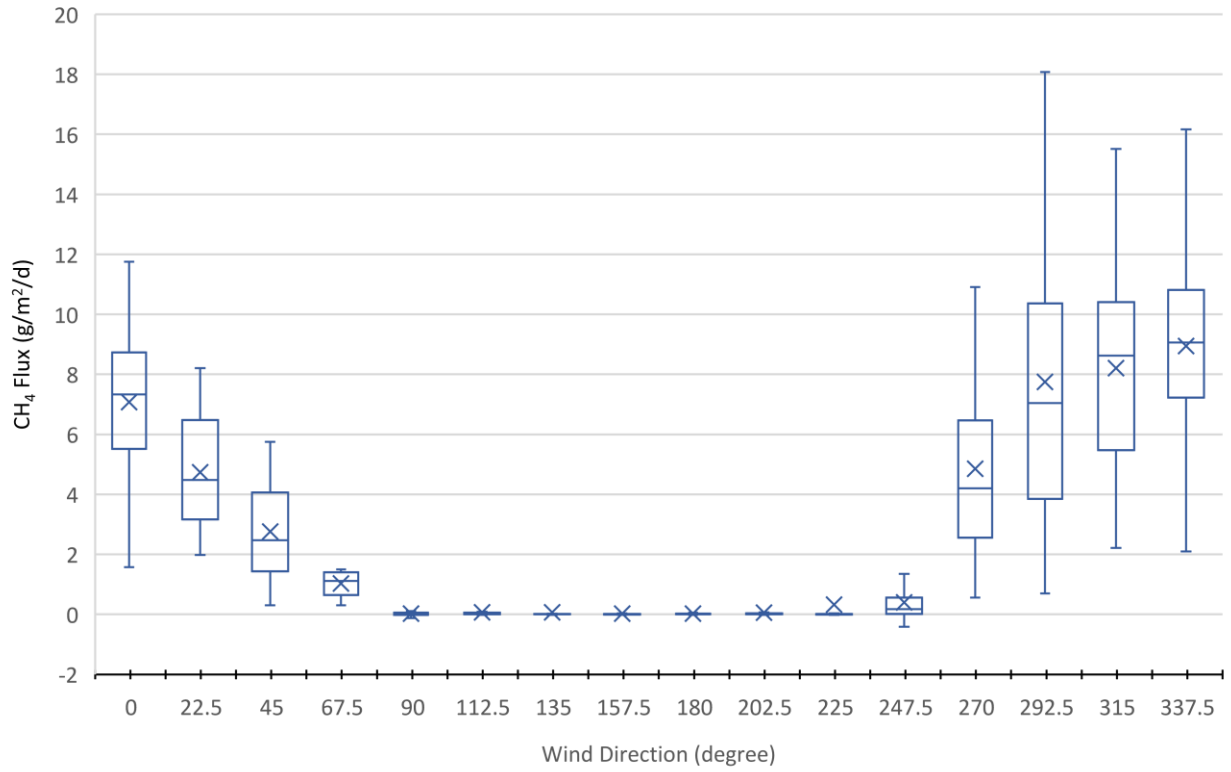

Figure 6.32. Dependence of EC flux of CH_4 from this study on wind direction binned by every 22.5 degrees.

You et al. also summarized the CH_4 flux data in a form of box and whisker chart based on the wind direction in Figure 6.33 (You et al., 2021). In both Figure 6.32 and Figure 6.32, the flux measurements are generally zero from wind direction coming from 90 degrees to 270 degrees, where wind blows from south towards the EC instruments. However, the flux measurements are positive from 270 degree to 360 degree and from 0 degree to 90 degrees, where wind blows from the pond towards the EC instruments. Clearly the pond contributes to higher CH_4 fluxes than the background.

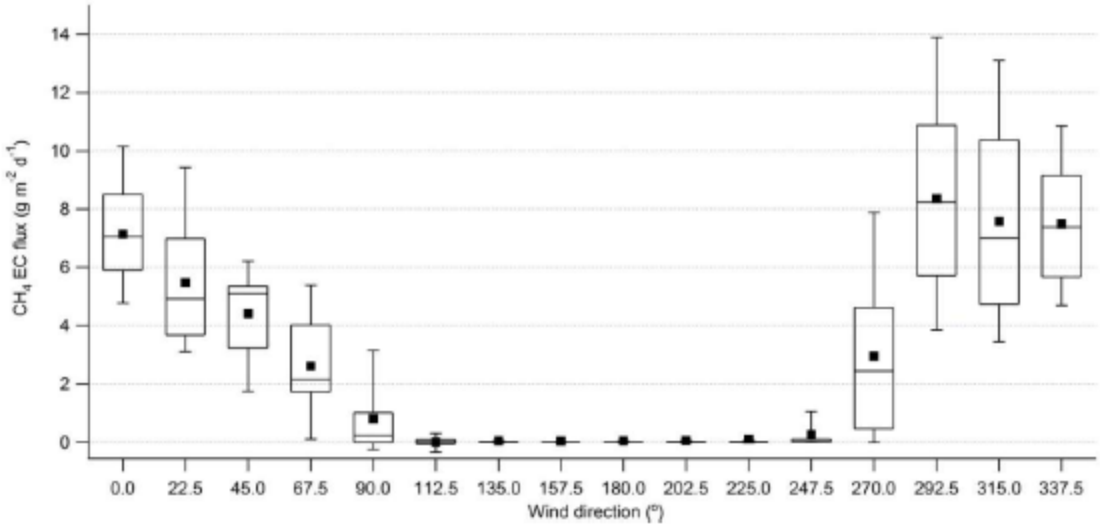

Figure 6.33. Dependence of EC flux of CH_4 on wind direction binned by every 22.5 degrees (adapted from You et al., 2021)**.**

The diurnal variation of the CH_4 flux, filtered by wind direction, was also analyzed in this study. Figure 6.34 shows the diurnal variation of flux measurements from wind direction $\geqslant 286°$, or wind direction $\leqslant 76°$, which represents flux contributions from the tailings pond. The CH_4 flux values vary less with the time of day than with the wind direction. Therefore, the general diurnal variations of CH_4 fugitive emissions from tailings pond do not follow a clear pattern.

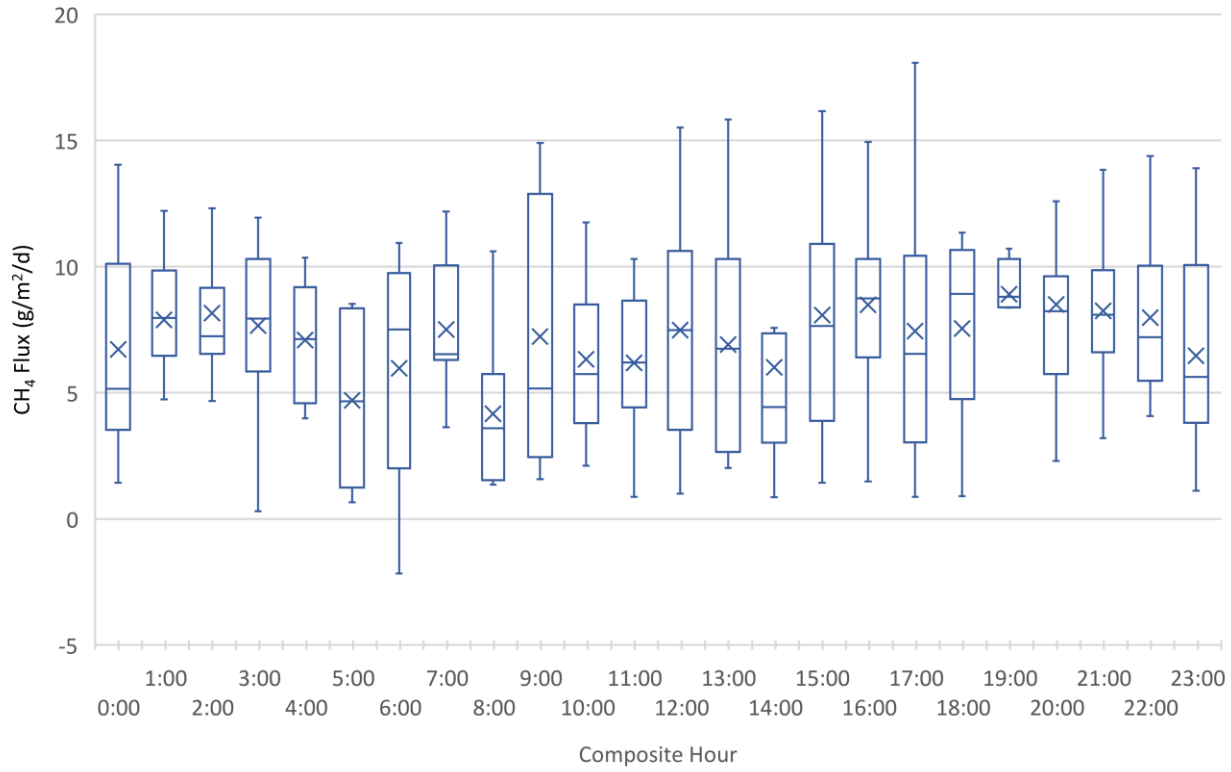

Figure 6.34. Diurnal variation of CH_4 EC flux for wind direction ≥ 286°, or wind direction ≤ 76°

Figure 6.35 provides the diurnal variation of CH_4 flux from the ECCC study. The flux measurements from wind direction ≥ 286°, or wind direction ≤ 76° do not follow a clear diurnal pattern. This is consistent with the findings of this study shown in Figure 6.34, which confirms that the fugitive CH_4 emissions from the pond do not vary extensively with time of the day.

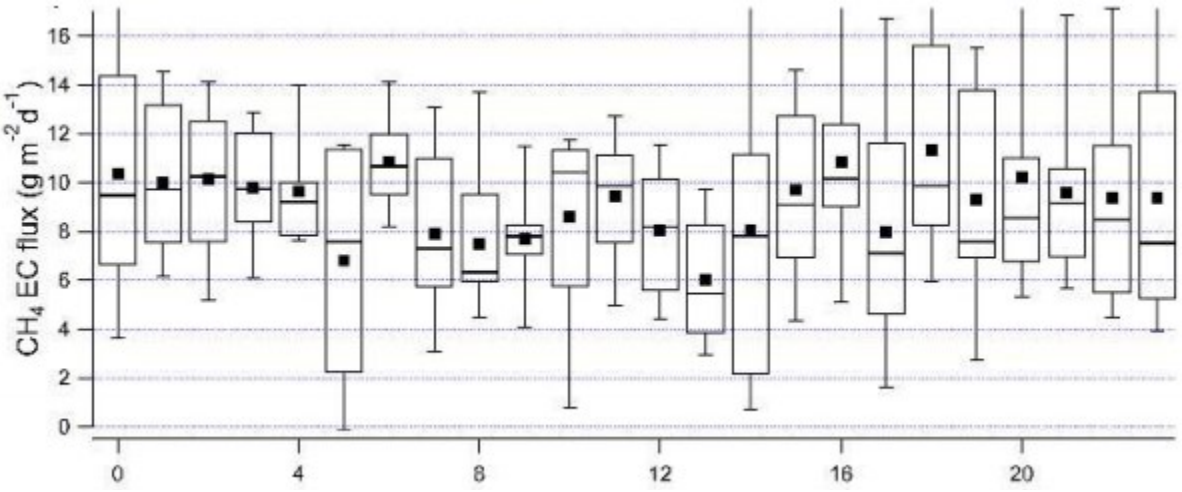

Figure 6.35. Diurnal variation of CH_4 EC flux for wind direction ≥ 286°, or wind direction ≤ 76° based on ECCC data (adapted from You et al., 2021)**.**

7.0 CONCLUSION

An EC tower was placed at Suncor's Tar Island tailings pond 2/3 from July 28 2017 to September 29 2017 to measure high-frequency meteorological parameters (air temperature, pressure, and wind condition) and high-frequency concentration data of GHGs (CO_2 and CH_4). Due to unfavourable wind direction, concerns about LI-7500A performance, and EddyPro flagging choices, data QA/QC discarded a large portion of measured data. The relationship between the normalized standard deviation of vertical velocity (σ_w/u^*) and stability ($-z/L$) matched existing models (Kaimal and Finnigan, 1995; Wilson, 2008) for undisturbed atmospheric surface layer.

During this field campaign, CO_2 concentration measurements did not depict obvious correlation with air temperature. However, CO_2 concentrations decreased as wind speed increases. CH_4 concentrations reached a maximum at around 291 K (around 18°C) and decreased with wind speed as well. Peak CO_2 concentrations often occurred during early morning, and peak CH_4 concentrations often occurred during midnight. In terms of fluxes, CO_2 fluxes generally increased with temperature, but did not show a clear correlation with wind speed. However, CH_4 fluxes reached a maximum at around 291 K (18°C), and maximum CH_4 fluxes increased with wind speed.

The wind direction comparison showed that the range of CO_2 fluxes values measured from the pond direction is higher than the range of CO_2 fluxes values measured from the areas off the pond (south of the EC tower). Comparing CO_2 fluxes from the pond and from south of the EC tower, higher magnitude of negative CO_2 fluxes usually came from the pond, suggesting that the

pond acts as a sink. For CH_4, the wind filtration indicates that CH_4 fluxes from the pond is much higher than the off pond CH_4 fluxes.

As 90 percent footprint of CO_2 fluxes increased, the spread of CO_2 flux values increased. For CH_4, the peak CH_4 fluxes increased as footprint increased. When 90 percent footprint went beyond the boundaries of the tailings pond, both CO_2 and CH_4 flux values became more stable with less spread of values as other sources outside of the pond contributes to the flux measurements. Stability analyses suggests the measured atmosphere above the tailings water surface was meteorically homogeneous. The dominant atmospheric conditions during the field campaign were unstable and neutral.

In daily composite data analyses, variation of CO_2 fluxes and CH_4 fluxes generally matched the variation of temperature during daytime since more data is available for averaging during daytime, as quality control discarded more nighttime data. The variation of CO_2 fluxes generally matched the variation of CH_4 fluxes during daytime as well.

Limitations of EC measurements include the validation of assumptions, challenge of configuring the tower height, instrument troubleshoot and maintenance, and unfavorable meteorological conditions.

Peak CO_2 concentrations often occur during early morning, and peak CH_4 concentrations often occur during midnight. These diurnal concentration patterns are consistent with previous measurements on water surfaces. Average CO_2 flux measurements of this EC tower are lower than previous CO_2 flux measurements on the same tailings pond. Possible reasons behind the difference are instrumental deviation, and nature of microbial processes in tailings pond.

CH_4 measurement results from this study were compared to ECCC measurements obtained at the same tailings pond during the same period. CH_4 measurements from this study showed a median CH_4 flux value of 6.5 $g/m^2/d$, which is 12% different from the median CH_4 flux value of 7.4 $g/m^2/d$ from the ECCC study. Both 6.5 $g/m^2/d$ and 7.4 $g/m^2/d$ median CH_4 flux values obtained from EC flux measurement method are higher than median values obtained from other flux measurement methods performed by ECCC, such as flux vertical gradient method, IDM, and flux chamber method. Compared to historical flux chamber measurements obtained at the same tailings pond, both flux measurements performed by this study and ECCC's study are higher than the historical flux measurements before 2017. Both studies captured similar patterns of CH_4 flux variations with wind direction and diurnal change during the 2017 field campaign.

The major scientific contribution of this thesis is to validate the efficiency and reliability of the EC system for GHGs flux measurements from oil sands tailings ponds. The CH_4 EC measurements of this study cover the majority of the tailings pond over an extended duration, while the flux chamber measurements are snapshot of emissions from a small portion of the tailings pond surface. The EC measurements of CH_4 flux from this study were consistent with measurements obtained using other techniques such as flux vertical gradient method, and IDM and are more reliable than flux chamber measurements. However, the EC measurements of CH_4 flux from this study were higher than concurrent and historical measurements obtained using flux chamber technique. The discrepancy between the EC median CH_4 flux (6.5 $g/m^2/d$) and the flux chamber median CH_4 flux may be due to the heterogeneity of the pond and the inherent uncertainty in the flux chamber measurement technique.

Based on the findings of this study, it is recommended to perform more EC flux measurements on oil sands tailings ponds to better understand the fugitive emissions from the ponds and to further investigate the economy, efficiency and reliability gain from implementing the EC technique. In addition, it is recommended to setup two EC towers at the opposite side of a target pond for better coverage of flux measurements considering the variation of wind direction throughout the measurement period.

REFERENCES

Aubinet, M., Vesala, T., Papale, D. (eds.) (2012). Eddy covariance: a practical guide to measurement and data analyses. Dordrecht, New York.

Baker, J., Norman, J., and Bland, W. (1992). Field-scale application of flux measurement by conditional sampling. Agricultural and Forest Meteorology, **62**(1):31-52.

Baray, S., Darlington, A., Gordon, M., Hayden, K. L. (2017). Quantification of methane sources in the Athabasca Oil Sands Region of Alberta by aircraft mass-balance. Accessed May 1, 2018 at [https://nparc.nrc-cnrc.gc.ca/eng/view/fulltext/?id=b116fe04-247b-4590-bca7-df08b9cd978b].

Barnack, A., and Jones, R. (2004). Practical assessment of the open path Fourier transform infrared (OP-FTIR) for ambient air quality monitoring in Portland and Albany Oregon – August to September 2003. Portland, Oregon. DEQ05-LAB-0031-TR, September 2004.

Brown, C. (2013). Quantifying methane emissions from an oil sands tailings pond using micrometeorological flux measurement techniques. Master's Thesis, Department of Earth and Atmospheric Sciences, University of Alberta, Edmonton, Alberta.

Burba, G. G., Mc Dermitt, D., Grelle, A., Anderson, D. J., Xu, L. (2008). Addressing the influence of instrument surface heat exchange on the measurements of CO_2 flux from open-path gas analysers. Global Change Biology, **14**:1854–1876.

Burba, G. (2013). Eddy Covariance Method for Scientific, Industrial, Agricultural, and Regulatory Applications. LI-COR, Inc. Lincoln, Nebraska.

Burba, G. (2018, July 11). Personal email.

Burkus, Z., Wheler, J., and Pletcher, S. (2014). GHG Emissions from oil sands tailings ponds: overview and modelling based on fermentable substrates. Land Policy (oil sands), Alberta Environment and Sustainable Resource Development (AESRD). Edmonton, Alberta.

Covey, K.R., and Megonigal, J.P. (2019). Methane production and emissions in trees and forests. New Phytologist, **222**(1): 35-51.

Denmead, O.T. (2008). Approaches to measuring fluxes of methane and nitrous oxide between landscapes and the atmosphere. Plant and Soil **309**(1-2): 5-24.

Dyer A.J. (1974). A review of flux-profile relationships. Boundary-Layer Meteorology, **7**: 363-372.

Dyer A.J., and Bradley, E.F. (1982). An alternative analysis of flux-gradient relationships at the 1976 ITCE. Boundary-Layer Meteorology, **22**: 3-19.

Emran, B.J., Tannant, D. D., Najjaran, H. (2017). Low-altitude aerial methane concentration mapping. Remote Sens, **9**(8): 1-13.

Famakinwa, T. E., Su, Y., Wang, J., Gates, I. D. (2018). An in-situ process to consolidate oil sands mine tailings. Journal of Environmental Chemical Engineering, **6**(2): 3295-3305.

Foken, T. (2008). *Micrometeorology*. Springer, Berlin/Heidelberg, 308 pp.

Goldenfum, J.A. (2010). GHG Measurement Guidelines for Freshwater Reservoirs. The International Hydropower Association (IHA). Sutton, London, United Kingdom.

Google Map. (2018). Map of Tar Island, Alberta. Website. Accessed May 1, 2018 at [https://www.google.ca/maps/place/Tar+Island,+AB/@56.9906699,-111.5212062,13.25z/data=!4m5!3m4!1s0x53b0718974f2f7c7:0xf31665703d4cb502!8m2!3d56.975847!4d-111.4811221].

Government of Alberta (GOA). (2014). Quantification of area fugitive emissions at oil sands mines. Climate Change Policy, Edmonton, Alberta, Canada. Accessed May 1, 2018 at [https://open.alberta.ca/dataset/8a419d10-68aa-4af9-8673-8a4cdf14175a/resource/0224eb1d-e817-4525-b833-22f9c49cc3a5/download/2014-areafugitiveemissionsoilsandsmines.pdf].

Government of Alberta (GOA). (2016). Total Area of the Oil Sands Tailings Ponds over Time. Website. Accessed February 24, 2022 at [http://osip.alberta.ca/library/Dataset/Details/542].

Government of Alberta (GOA). (2017). Climate leadership plan progress report. Alberta, Canada. Accessed May 1, 2018 at [https://open.alberta.ca/publications/climate-leadership-plan-progress-report-2016-17].

Government of Alberta (GOA). (2018). Climate leadership plan. Website. Accessed May 1, 2018 at [https://www.alberta.ca/climate-leadership-discussion.aspx].

Högström, U. (1988). Non-dimensional wind and temperature profiles in the atmospheric surface layer: a re-evaluation. Boundary-Layer Meteorology, **42**: 55-78.

Hsieh, Cheng-I, G. Katul, and T. Chi. (2000). An approximate analytical model for footprint estimation of scalar fluxes in thermally stratified atmospheric flows. Advances in Water Resources, **23**: 765-772.

IPCC. (2007). Climate change (2007): Working group i: The physical science basis. Cambridge University Press, Cambridge, UK.

Ivey Business School. (2016). By the numbers: Canadian ghg emissions. Western University. Ontario, Canada. Accessed May 1, 2018 at [https://www.ivey.uwo.ca/cmsmedia/2112500/4462-ghg-emissions-report-v03f.pdf].

Jones, A.M., Harrison, R.M., Baker, J. (2010). The wind speed dependence of the concentrations of airborne particulate matter and NO_x. Atmospheric Environment, **44**: 1682-1690.

Kaimal, J.C., and Finnigan, J.J. (1995). Atmospheric boundary layer flows: Their structure and measurement. Oxford University Press, New York.

Kathilankal, J. (2018, July 19). Personal email.

Kiemle, C., Ehret, G., Amediek, A., Fix, A., Quatrevalet, M., Wirth, M. (2017). Potential of Spaceborne Lidar Measurements of Carbon Dioxide and Methane Emissions from Strong Point Sources. Remote Sensing, **9**(11), 1-16.

Kljun, N., Calanca, P., Rotach, M. W., and Schmid, H. P. (2004). A simple parameterisation for flux footprint predictions. Boundary-Layer Meteorology, **112**: 503-523.

Kljun, N., Calanca, P., Rotach, M. W., and Schmid, H. P. (2015). A simple two-dimensional parameterisation for Flux Footprint Prediction (FFP), Geosci. Model Dev., **8**: 3695-3713.

Kormann, R. and F. X. Meixner. (2001). An analytical footprint model for nonneutral stratification. Boundary-Layer Meteorology, **99**:207–224.

Kumar, A., Bhatia, A., Fagodiya, R.K., Malyan, S.K., Meena, and B.L. (2017). Eddy covariance flux tower: a promising technique for greenhouse gases measurement. Advances in Plants & Agriculture Research., **7**(4): 337-340.

Lagarias, J.C., Reeds, J.A., Wright, G.H., and Wright, P.E. (1998). Convergence properties of the nelder-mead simplex method in low dimensions. SIAM Journal on Optimization, **9**(1): 112-147.

LI-COR. (2009). LI-7500A open path CO_2/H_2O gas analyzer instruction manual. Lincoln, Nebraska. Accessed May 1, 2018 at [http://www.ecotek.com.cn/download/Manual-LI-7500A-EN.pdf].

LI-COR. (2016). EddyPro User's Guide. Lincoln, Nebraska. Accessed May 1, 2018 at [https://www.licor.com/documents/1ium2zmwm6hl36yz9bu4].

LI-COR. (2018). Installation of EC system. Website. Accessed May 1, 2018 at [https://www.licor.com/env/products/eddy_covariance/installation.html].

LI-COR. (2018, July 19). Personal email.

LI-COR. (2020). LI-7700 open path CH_4 gas analyzer instruction manual. Lincoln, Nebraska. Accessed March 20, 2022 at [https://www.licor.com/documents/18warrx05laaa1zo9s0pepmjk0cgiqm3].

Laubach, J., Kelliher, F.M. (2004). Measuring methane emission rates of a dairy cow herd by two micrometeorological techniques. Agricultural and Forest Meteorology, **125**(3-4): 279-303.

Lin, C., Liou, N., and Sun, E. (2012). Applications of Open-Path Fourier Transform Infrared for identification of volatile organic compound pollution sources and characterization of source emission behaviors. Journal of the Air & Waste Management Association, **58**(6): 821-828.

Mahzabin, T. (2012). Quantifying methane emission from surface sources using the backward Lagrangian stochastic method. Master's thesis, University of Alberta.

Mauder, M., Cuntz, M., Drüe, C., Graf, A., et al. (2013). A strategy for quality and uncertainty assessment of long-term eddy-covariance measurements. Agricultural and Forest Meteorology, **169**: 122-135.

Mauder, M., Foken, T., 2004. Documentation and Instruction Manual of the Eddy Covariance Software Package TK2. Universität Bayreuth, Abteilung Mikrometeorologie: Arbeitsergebnisse 26, ISSN 1614-8924, 44 pp.

Moncrieff, J. B., Massheder, J. M., de Bruin, H., Elbers, J., et al. (1997). A system to measure surface fluxes of momentum, sensible heat, water vapour and carbon dioxide. Journal of Hydrology, **188-189**: 589-611.

Moncrieff, J. B., R. Clement, J. Finnigan, T. Meyers. (2004). Averaging, detrending and filtering of eddy covariance time series, in Handbook of micrometeorology: a guide for surface flux measurements, eds. Lee, X., Massman, W. J., and Law, B. E. Dordrecht: Kluwer Academic, page 7-31.

Ott, L. E., Pawson, S., Collatz, G. J., Gregg, W. W., et al. (2015). Assessing the magnitude of CO_2 flux uncertainty in atmospheric CO_2 records using products from NASA's Carbon Monitoring Flux Pilot Project. J. Geophys. Res. Atmos, **120**: 734–765.

Pavelka, M., Acosta, M., Kiese, R., Altimir, N., et al. (2018). Standardisation of chamber technique for CO_2, N_2O and CH_4 fluxes measurements from terrestrial ecosystems. International Agrophysics, **32**: 569-587.

Sawyer, C. N., McCarty, P. L., Parkin, G. F. (2003). *Chemistry for environmental engineering and science*. 5th ed. Boston: McGraw-Hill.

Schmid, H.P. (1994). Source areas for scalars and scalar fluxes. Boundary-Layer Meteorology, **67**: 293-318.

Schuepp, P., Leclerc, M., MacPherson, J., Desjardins, R. L. (1990). Footprint prediction of scalar fluxes from analytical solutions of the diffusion equation. Boundary-Layer Meteorology, **50**: 355-373.

Siddique, T., Fedorak, P.M., Mackinnon M.D., Foght, J.M. (2007). Metabolism of BTEX and Naphtha Compounds to Methane in Oil Sands Tailings. Environmental Science and Technology, **41**(7): 2350-2356.

Siddique, T., Gupta, R., Fedorak, P.M., MacKinnon M.D., Foght, J.M. (2008). A first approximation kinetic model to predict methane generation from an oil sands tailings settling basin. Chemosphere, **72**(10): 1573-1580.

Siddique, T., Penner, T., Semple, K., Foght, J.M. (2011). Anaerobic biodegradation of longer-chain n-Alkanes coupled to methane production in oil sands tailings. Environmental Science and Technology, **45**(13): 5892-5899.

Siebicke, L. and Emad, A. (2019). True eddy accumulation trace gas flux measurements: proof of concept. Atmospheric Measurement Techniques, **12**: 4393–4420.

Small, C. C., Cho, S., Hashisho, Z., Ulrich, A. C. (2015). Emissions from oil sands tailings ponds: Review of tailings pond parameters and emission estimates. Journal of Petroleum Science and Engineering, **127**: 490-501.

Snedecor, G.W. and Cochran, W.G. (1980). *Statistical Methods, 7th ed*. Ames, IA: Iowa State Press, p. 180.

Solomon, S., Daniel, J. S., Sanford, T. J., Murphy, D. M., Plattner, G.-K., Knutti, R., & Friedlingstein, P. (2010). Persistence of climate changes due to a range of greenhouse gases. Proceedings of the National Academy of Sciences of the United States of America, **107**(43): 18354–18359.

Stasik, S., Wendt-Potthoff, K. (2016). Vertical gradients in carbon flow and methane production in a sulfate-rich oil sands tailings pond. Water Research, **106**: 223-231.

Stull, R.B. (1988). An introduction to boundary layer meteorology. Kluwer Academic Publishers, AH Dordrecht, The Netherlands.

Todd, L.A., Ramanathan, M., Mottus, K., Katz, R., Dodson, A. and Mihlan, G. (2001). Measuring chemical emissions using open-path Fourier transform infrared (OP-FTIR) spectroscopy and computer-assisted tomography. Atmospheric Environment **35**: 1937-1947.

Wang, M., Guan, D., Han, S., Wu, J. (2009). Comparison of eddy covariance and chamber-based methods for measuring CO_2 flux in a temperate mixed forest. Tree Physiology, **30**: 169-163.

Webb, E. K., G. I. Pearman, and R. Leuning. (1980). Correction of flux measurements for density effects due to heat and water vapor transfer. Quarterly Journal of the Royal Meteorological Society, **106**: 85–100.

Wilson, J. (2008). Monin-obukhov functions for standard deviations of velocity. Boundary-Layer Meteorology, **129**(3): 353-369.

You, Y., Staebler, R.M., Moussa, S.G., Beck, J., Mittermeier, R.L. (2021). Methane emissions from an oil sands tailings pond: a quantitative comparison of fluxes derived by different methods. Atmospheric Measurement Techniques, **14**(3): 1879-1892.

Zhang, L., Cho, S., Hashisho, Z., Brown, C. (2019). Quantification of fugitive emissions from an oil sands tailings pond by eddy covariance. Fuel, **237**: 457-464.

APPENDIX A

Metadata Calculations

North separations and east separations for LI-7500A and LI-7700 gas analysers

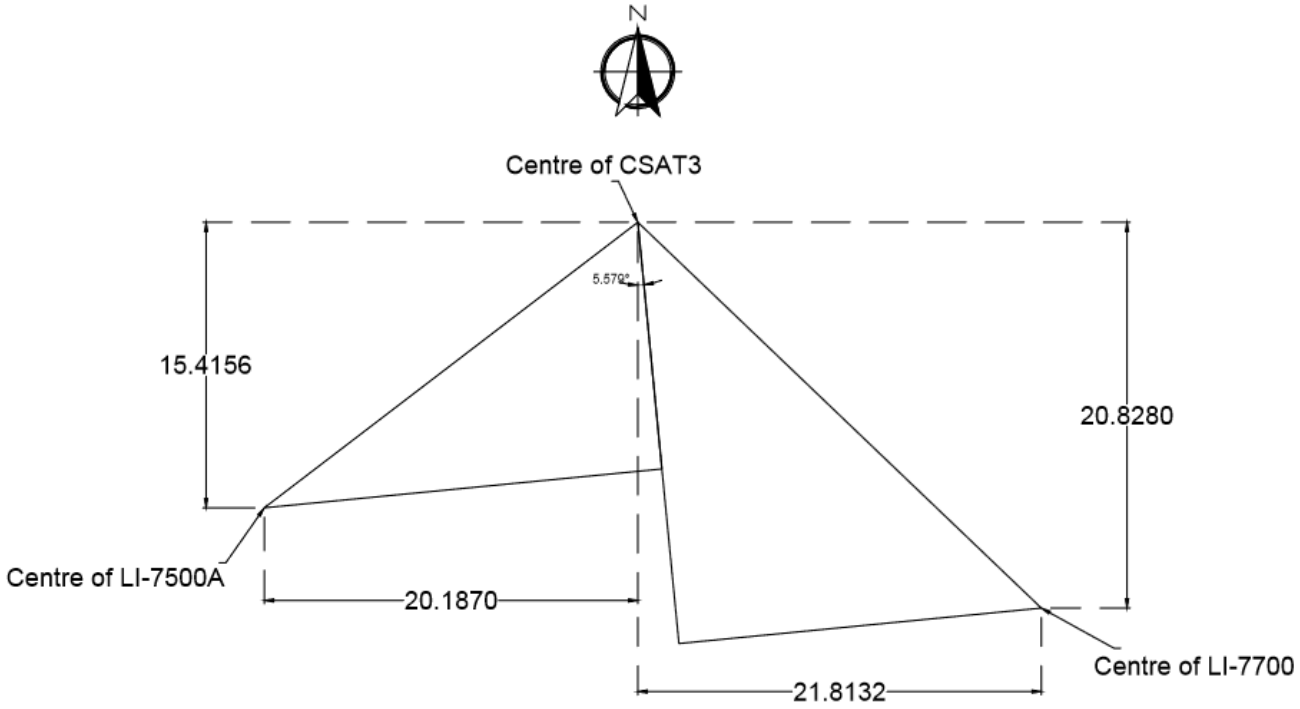

Note: north direction arrow represents the true north.
From the above figure:
North separation is -15.4 cm for LI-7500A, and -20.8 cm for LI-7700
East separation is -20.2 cm for LI-7500A, and +21.8 for LI-7700

Magnetic declination calculation

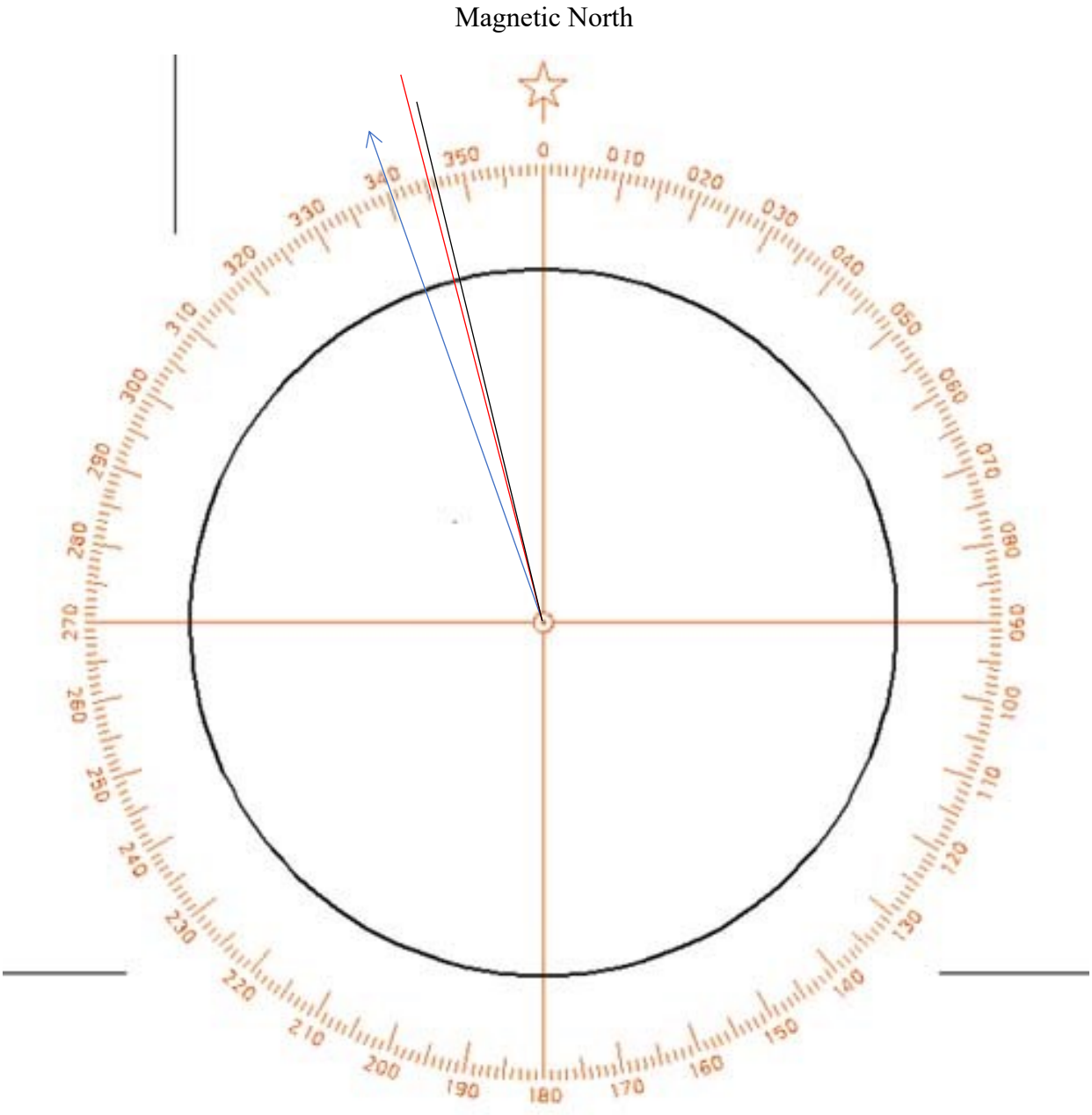

Black line: True North (TN) with Magnetic Declination of **13° 55.26' East** (MN east to TN)
Red line: Grid North (GN) with Grid Declination of **14° 20.82' East** (MN east to GN)
Blue arrow: Measured CSAT3 magnetic bearing at **19.5° West** to magnetic north
Convergence Angle is 0° 25.56' West
Calculated North Offset for use in EddyPro: **19.5° - 13° 55.26' = 5.579°**
To implement on topographic map: **19.5° - 14° 20.82' = 5.153°** (CSAT3 points 5.153° west to GN)

Metadata Calculation Data Source

Compass Figure: [http://www.riti.com/images/pilotage/Compassrose.jpg]

Magnetic declination calculation: [http://geomag.nrcan.gc.ca/calc/mdcal-r-en.php?date=2017-09-24&latitude=56.983699&latitude_direction=1&longitude=111.508283&longitude_direction=-1&grid=on]

Magnetic declination calculator - Results

IGRF-12 (2015) Model Results

Latitude: 56.9836° North
Longitude: 111.5083° West
Date: 2017-09-24

Magnetic declination: 13° 55.26' East

Annual Change (minutes/year): 12.3 '/y West

Grid Declination: 14° 20.82' East

Convergence Angle: 0° 25.56' West

Magnetic declination and grid declination description: [http://geomag.nrcan.gc.ca/mag_fld/magdec-en.php]. Note: UofA 2017 EC case fit to case 3 of the declination combinations.

Use of Compass in the field for magnetic declination: [http://geomag.nrcan.gc.ca/mag_fld/compass-en.php]

APPENDIX B

Footprint Data Filtration

MATLAB manuscript

```
%% Data Input

% Name the EC raw data spreadsheet as "ECRawDataSummary"
% Import it into MatLab workspace with "Matrix" option and need to include column A(the first
column)
% Run following manuscript based on data filtration requirements

% Extract wind direction (WD) data as integer, make sure column 71 of "ECRawDataSummary"
represents the wind direction data
WD=ECRawDataSummary(:,71);

% Initial setup of the output file
Output1=ECRawDataSummary;
% Obtain row size of the spreadsheet
b=length(ECRawDataSummary(:,71));
% Set up error storage as e for discarding data
e=[];

%% Data Filtration
% Data filtration based on wind direction
e1=e;
for i=1:b
   if WD(i)>90&&WD(i)<270
      e1=[e1 i];
   end
end

Output2=Output1;
Output2(e1,:)=[];

% Data filtration based on LI-7500A diagnostic number and invalid footprint(90 percent)
% Extract CO2 Diagnostic number
CO2_Diag=Output2(:,148);
Footprint=Output2(:,88);
e2=e;
b=length(Output2(:,71));
for i=1:b
   if (CO2_Diag(i)~=0)||Footprint(i)==-9999
      e2=[e2 i];
   end
end

Output3=Output2;
Output3(e2,:)=[];
```

```
% Data filtration based on footprint values (90 percent) fall out of the pond boundary
% Use 30 degree wind direction as bin of footprint data
% Extract footprint (90 percent) data and WD data
WD=Output3(:,71);
Footprint=Output3(:,88);
e3=e;
b=length(Output3(:,71));
for i=1:b
   if (WD(i)>=270&&WD(i)<300)&&(Footprint(i)>1380)
      e3=[e3 i];

   elseif (WD(i)>=300&&WD(i)<330)&&(Footprint(i)>1540)
      e3=[e3 i];

   elseif (WD(i)>=330&&WD(i)<=360)&&(Footprint(i)>1480)
      e3=[e3 i];

   elseif (WD(i)>=0&&WD(i)<30)&&(Footprint(i)>1240)
      e3=[e3 i];

   elseif (WD(i)>=30&&WD(i)<60)&&(Footprint(i)>1370)
      e3=[e3 i];

   elseif (WD(i)>=60&&WD(i)<=90)&&(Footprint(i)>1380)
      e3=[e3 i];
   end
end

Output4=Output3;
Output4(e3,:)=[];
%% Data filtration based on data quality flags

% Discard all invalid CO2 concentration data
CO2_Conc=Output4(:,36);
% Setup a separate output for CO2 Concentration
Output5=Output4;
e4=e;
b=length(Output4(:,36));
for i=1:b
   if CO2_Conc(i)==-9999
      e4=[e4 i];
   end
end

Output5(e4,:)=[];
```

```
% Flags for CO2 Flux
CO2_Flag=Output5(:,18);
% Setup a separate output for CO2 flux
Output6=Output5;
e5=e;
b=length(Output5(:,18));
for i=1:b
   if CO2_Flag(i)==2
       e5=[e5 i];
   end
end

Output6(e5,:)=[];

% Discard all invalid CH4 concentration data
CH4_Conc=Output4(:,46);
% Setup a separate output for CH4 concentration
Output7=Output4;
e6=e;
b=length(Output4(:,46));
for i=1:b
   if CH4_Conc(i)==-9999
      e6=[e6 i];
   end
end

Output7(e6,:)=[];

% Flags for CH4 Flux
CH4_Flag=Output7(:,24);
% Setup a separate output for CO2 flux
Output8=Output7;
e7=e;
b=length(Output7(:,24));
for i=1:b
   if CH4_Flag(i)==2
      e7=[e7 i];
   end
end

Output8(e7,:)=[];

%% Data Output from MatLab Matrix to Excel
filename1 = 'MatLab_Output_General.xlsx';
xlswrite(filename1,Output4,1)
```

```
% If CO2 Concentration and Flux data output are required
filename2 = 'MatLab_Output_CO2_Conc.xlsx';
xlswrite(filename2,Output5,1)

filename3 = 'MatLab_Output_CO2_Flux.xlsx';
xlswrite(filename3,Output6,1)

% If CH4 Concentration and Flux data output are required
filename4 = 'MatLab_Output_CH4_Conc.xlsx';
xlswrite(filename4,Output7,1)

filename5 = 'MatLab_Output_CH4_Flux.xlsx';
xlswrite(filename5,Output8,1)
```